Characterization of Alkaline-doped wide bandgap chalcopyrite Cu(In,Ga)Se$_2$ thin films and solar cells

Dissertation

zur Erlangung des Doktorgrades der Naturwissenschaften

(*Dr. rer. nat.*)

der

Naturwissenschaftlichen Fakultät II

Chemie, Physik und Mathematik

der Martin-Luther-Universität

Halle-Wittenberg

vorgelegt von

Frau SETAREH ZAHEDI-AZAD

geb. am 18.06.1988 in Essen

Erstgutachter: Prof. Dr. Roland Scheer
Zweitgutachter: Prof. Dr. Jöerg Schilling
Drittgutachter: Prof. Dr.-Ing Michael Powalla

Tag der Abgabe: 07.01.2020
Tag der öffentlichen Verteidigung: 09.10.2020
Mitglieder der Promotionskommission: Prof. Dr. Jamal Berakdar (Vorsitz), Prof. Dr. Miguel Marques, Prof. Dr. Horst Beige, Prof. Dr. Detlef Reichert, PD Dr. Karl-Michael Schindler, PD Dr. Jan Kantelhardt

Contents

1. Introduction

In recent years considerable attention has been paid to research and develop wide bandgap solar cells. The wide bandgap cells have a better solar cell temperature coefficient and perform more stable under real working conditions [1, 2]. Further, widening the bandgap reduces the current density which in turn lowers the electric losses in the cell [1, 2]. The theoretical calculations of Shockley–Queisser estimates the highest conversion efficiency for a single junction at a bandgap value of 1.4 eV [3], but also as a multi-junction they are promising for top cell of a tandem staking solar cell.

Among the different compounds, the $Cu(In,Ga)Se_2$ (CIGSe) semiconductor is one candidate to fabricate highly efficient solar cell. The material has a direct band gap and offers a large absorption coefficient. As a result a thin layer (2 - 3 μm) would suffice to absorb the incident photons from the sun [4]. Despite the advantage that wide-gap $Cu(In,Ga)Se_2$ absorbers offer, higher efficiency than 12% is not achieved yet [5].

The $Cu(In,Ga)Se_2$ absorbers with high-gallium content have many order of magnitude smaller minority carrier lifetime compared to low-gallium content samples, which reduces the open-circuit voltage [4, 6]. Further, the increase of the gallium content in the absorber leads to a strong voltage dependency of the carrier collection that deteriorates the fillfactor [7]. The voltage dependency of the carrier collection comes from the poor minority carrier diffusion length, which is also related to the reduced minority carrier lifetime [7].

The fall-off of the fillfactor and reduction of the open-circuit voltage due to the low minority carrier lifetime are one reason that lowers the efficiency of wide-gap $Cu(In,Ga)Se_2$ cells. The main reason of the low performance of wide-gap $Cu(In,Ga)Se_2$ devices is the high recombination rate at the charge collecting interface that prevents the open-circuit voltage to reach the level expected for the bandgap of the absorber [2].

One reason of the high interface recombination is the unfavorable band offset between absorber and buffer layer, that changes from a spike to a cliff for wide-gap $Cu(In,Ga)Se_2$ cells and provides high concentration of holes at the interface [8]. In order to reduce the recombination at the interface one solution is to lower the valence band edge [8]. This can be accomplished for instance with addition of sulfur [9]. Recently, it has been reported that the post-deposition treatment of alkalis on small bandgap CIGSe absorbers reduces the recombination rate at the interface by shifting the valence band edge downward at the hetero-interface between $Cu(In,Ga)Se_2$ and CdS layer [10–12]. However, most studies are on small bandgap CIGSe cells and little is known about the impact of the post-deposition

treatment of alkalis on wide-gap CIGSe devices. Therefore, in the present work, the influence of the post-deposition treatment with alkaline elements on wide-gap $Cu(In,Ga)Se_2$ cells is investigated. From temperature dependent current-voltage analysis, the electronic transport of the charge carriers is simulated and finally the dominant recombination path is examined.

The outline of this thesis is as follows:

- In Chapter 2, the basic equations of hetero-junction solar cells are presented. The charge carrier transport in the bulk and at the interface is explained and the fundamental equations of recombination regions are given.

- In Chapter 3, the steps from preparation of the $Cu(In,Ga)Se_2$ absorber to the finished solar-cell are described, and the methods used to characterize the cells are introduced.

- In Chapter 4, the role of a gallium gradient of wide-gap $Cu(In,Ga)Se_2$ cells on sodium containing substrates is examined. The influence of a gallium gradient on the electronic parameters, collection probability and collection efficiency is investigated.

- In Chapter 5, the influence of post-deposition treatment of heavy alkalis on the electronic parameters of $Cu(In,Ga)Se_2$ cells is investigated. The measurement results of temperature dependent current-voltage analysis are presented and numerical simulations with Synopsis® TCAD are performed to explain two effects "crossover" and "double-diode" occurring for the alkali-treated current-voltage curves.

- In Chapter 6, the dominant recombination path of the wide-gap alkali-treated devices is examined. This is accomplished by measuring the open-circuit voltage transients ($V_{OC}(t)$). By measuring the transients of the doping density, the $V_{OC}(t)$ is recalculated and the different slopes of the $V_{OC}(t)$ are discussed.

- In Chapter 7, the impact of alternative substrates on the electronic parameters of the wide-gap $Cu(In,Ga)Se_2$ cells are examined. In section 7.1, the effect of the post-deposition treatment of sodium and potassium on the solar cell parameters of $Cu(In,Ga)Se_2$ absorber is investigated. In section 7.2, the role of substrate temperature during absorber growth on the electronic properties of the wide-gap $Cu(In,Ga)Se_2$ cells is studied.

- In Chapter 8, the results of the present work are summarized and final conclusions are drawn.

2. Fundamentals of solar cells

In this chapter the basic equations to describe an absorber/buffer/window hetero-structure are introduced. Different kinds of recombination types and regions are discussed in section 2.3. Finally, a review on wide gap Cu(In,Ga)Se$_2$ cells and the latest investigations on the alkali post deposition treatment will be given.

2.1. Physics of an absorber/buffer/window hetero-structure

The structure of the solar cells studied in this thesis consists of an absorber (Cu(In,Ga)Se$_2$), buffer layer (CdS) and a window (ZnO) layer. The window layer is a highly doped material (10^{18} cm^{-3}), and the buffer layer is very low doped (10^{15} cm^{-3}) [4]. Depending on the gallium and sodium concentration the doping density of the absorber varies in the range of 5×10^{14} - 1.5×10^{16} cm^{-3} [13, 14]. The hetero-structure of a wide-gap Cu(In,Ga)Se$_2$ cell is sketched in the figure 2.1(a - d). The built-in potential (V_{bi}) across the space charge region is defined by:

$$qV_{\mathrm{bi}} = E_{\mathrm{g,a}} - E_{\mathrm{p,a}} - E_{\mathrm{n,w}} + \Delta E_{\mathrm{c}}^{a,b} + \Delta E_{\mathrm{c}}^{b,w} \tag{2.1.1}$$

where $E_{\mathrm{g,a}}$ is the bandgap of the absorber, $E_{\mathrm{p,a}}$ is the energy difference between the hole fermi level and the valence band edge of the the neutral bulk region, $E_{\mathrm{n,w}}$ is the energy difference between the electron Fermi level and the conduction band edge of the neutral bulk region in the window layer, and $\Delta E_{\mathrm{c}}^{a,b} + \Delta E_{\mathrm{c}}^{b,w}$ are the conduction band offsets at the absorber/buffer and buffer/window interface. The hole barrier at the interface between CIGSe and CdS is the sum of the potential drop in the absorber layer and $E_{\mathrm{p,a}}$ [15]:

$$\begin{aligned}
E_{\mathrm{p,a}}^{if} = & E_{\mathrm{p,a}} + q(V_{\mathrm{bi}} - V) + \frac{q^2 N_{D,b} d_{\mathrm{b}}^2}{2\epsilon_{\mathrm{b}}} + \frac{q^2 \epsilon_{\mathrm{a}} N_{\mathrm{A,a}} d_{\mathrm{b}}^2}{\epsilon_b^2} \\
& - \frac{2\epsilon_{\mathrm{a}} N_{\mathrm{A,a}} d_{\mathrm{b}}^2}{\epsilon_b^2} \sqrt{d_b^2 + \frac{\epsilon_{\mathrm{b}} N_{D,b} d_{\mathrm{b}}^2}{\epsilon_{\mathrm{a}} N_{\mathrm{A,a}}} + \frac{2\epsilon_{\mathrm{b}}^2}{q^2 \epsilon_{\mathrm{a}} N_{\mathrm{A,a}}} q(V_{\mathrm{bi}} - V)}
\end{aligned} \tag{2.1.2}$$

where d_{b} is the thickness of the buffer layer, and $N_{\mathrm{A,a}}$ and $N_{\mathrm{D,b}}$ are the doping density of the absorber and the buffer layer, respectively. The volume charge can be calculated by equation 2.1.3:

$$\rho = \frac{q}{\epsilon_0} \left(p(z) - n(z) - N_{\mathrm{D}}^+(z) - N_A^-(z) \right) \tag{2.1.3}$$
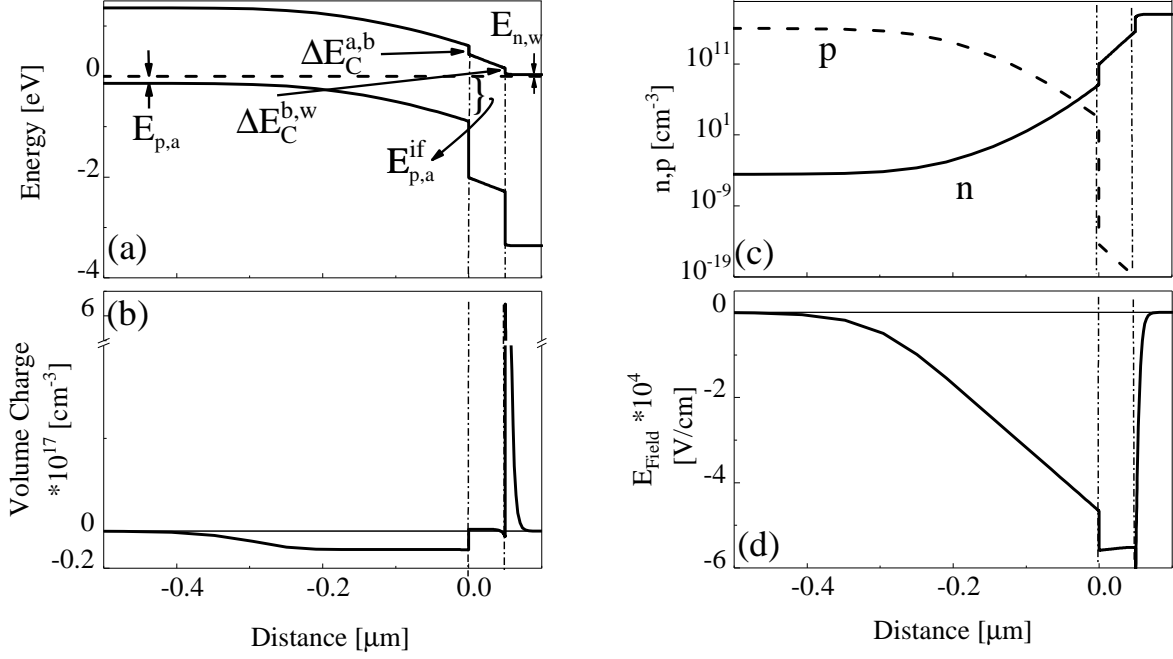
Figure 2.1.: Simulation of an absober/buffer/window hetero-structure with interface states of 2×10^9 cm^{-2} at the absorber/buffer interface charge, (a) band diagram in equilibrium, (b) volume charge on a logarithmic scale, (c) densities of electrons and holes, (d) electric field. The images are adapted from [4].

where $p(z)$ and $n(z)$ are the free charges and $N_D^+(z)$ and $N_A^-(z)$ are the ionized donors and acceptors, respectively [16]. As can be seen in figure 2.1(b), the electrical charge in the buffer layer is very low. Due to the low doping density of the buffer layer, the width of the space charge region extends into the window layer (Fig. 2.1(b - c)). Furthermore, the highly doped window layer results in a large space charge width in the absorber layer (Fig. 2.1(b - c)). The space charge width of the absorber (w_a) can be calculated by equation 2.1.4 [4]:

$$w_a = -\frac{d_b \epsilon_a}{\epsilon_b} + \sqrt{\left(\frac{d_b \epsilon_a}{\epsilon_b}\right)^2 + \frac{2\epsilon_0 \epsilon_a}{q^2 N_{A,a}}\left(q(V_{bi} - V) + \frac{(qd_b)^2 N_{D,b}}{2\epsilon_0 \epsilon_b}\right)} \qquad (2.1.4)$$

In figure 2.1(d), the distribution of electrons and holes are depicted. The figure 2.1(c), indicates that the densities of holes and electrons of the buffer layer are lower than the absorber and window layer. Consequently, the buffer layer is depleted and leads to a constant electric field as can be seen in figure 2.1(d). By the use of equation 2.1.4, the total capacitance can be calculated [4]. With the assumption that the width of the space charge region in the window is negligible ($w_w \longrightarrow 0$) and the buffer layer is completely

depleted ($w_\text{b} = d_\text{b}$), the total capacitance is given by [4]:

$$\frac{1}{C_\text{scr}} = \left(\frac{w_\text{a}}{\epsilon_0 \epsilon_\text{a}} + \frac{w_\text{b}}{\epsilon_0 \epsilon_\text{b}} + \frac{w_\text{w}}{\epsilon_0 \epsilon_\text{w}} \right)^{-1}$$

$$= \sqrt{ \left(\frac{d_\text{b}}{\epsilon_a \epsilon_b} \right)^2 + \frac{2}{q^2 N_{A,a} \epsilon_0 \epsilon_\text{a}} \left(q(V_\text{bi} - V) + \frac{(qd_b)^2 N_{D,b}}{2\epsilon_0 \epsilon_b} \right) } \quad (2.1.5)$$

2.2. Charge carrier transport

2.2.1. Transport equations in the bulk

The transport equations for electrons and holes under bias in one dimension is given by [17]:

$$J_\text{n}(z) = \mu_\text{n}\, n(z) \nabla_\text{z} E_\text{Fn}(z) \quad (2.2.1\text{a})$$

$$J_\text{p}(z) = \mu_\text{p} p(z)\, \nabla_\text{z} E_\text{Fp}(z) \quad (2.2.1\text{b})$$

where $J_\text{p}(z)$ and $J_\text{n}(z)$ are the electric current densities of holes and electrons and μ_p and μ_n are the mobilities of the holes and electrons, respectively. The current densities ($J_\text{n/p}$) consist of two terms; drift and diffusion term and can be expressed as following:

$$J_\text{n}(z) = \mu_n n(z) \left(q\, E(z) - \frac{d}{dz} \chi(z) \right) + q D_\text{n} \frac{d}{dz} n(z) \quad (2.2.2\text{a})$$

$$J_\text{p}(z) = \mu_p p(z) \left(q\, E(z) - \frac{d}{dz} \chi(z) + \frac{d}{dz} E_\text{g} \right) - q D_\text{p} \frac{d}{dz} p(z) \quad (2.2.2\text{b})$$

The first parentheses in equations 2.2.2a and 2.2.2b is called the drift current and is the migration of carriers due to the presence of an electric field. Such a force-field can be induced by a bandgap grading [18–20]. The second term in equations 2.2.2a and 2.2.2b is the diffusion current and is proportional to the gradient of the carrier concentration and arises from non-uniform illumination or local injection of carriers [17]. The substitution of the current densities of holes and electrons from equation 2.2.2 into the continuity equation yields to [17, 21]:

$$\frac{\partial n(z)}{\partial t} = G_\text{n} - U_\text{n} + \frac{1}{q} \frac{d}{dz} \left(\mu_n n(z) \left(q\, E(z) - \frac{d}{dz} \chi(z) \right) + q D_\text{n} \frac{d}{dz} n(z) \right) \quad (2.2.3\text{a})$$

$$\frac{\partial p(z)}{\partial t} = G_\text{p} - U_\text{p} - \frac{1}{q} \frac{d}{dz} \left(\mu_p p(z) \left(q\, E(z) - \frac{d}{dz} \chi(z) + \frac{d}{dz} E_\text{g} \right) - q D_\text{p} \frac{d}{dz} p(z) \right) \quad (2.2.3\text{b})$$

In the steady state condition ($\frac{\partial n(z)}{\partial t} = \frac{\partial p(z)}{\partial t} = 0$) and with the assumption of a low carrier injection (Eq.2.3.3), the equations 2.2.3 at zero field for minority carriers become:

$$0 = -\frac{n}{\tau_{\mathrm{n}}} + q\,D_{\mathrm{n}}\frac{d^2 n(z)}{dz^2} \tag{2.2.4a}$$

$$0 = \frac{p}{\tau_{\mathrm{p}}} - q\,D_{\mathrm{p}}\frac{d^2 p(z)}{dz^2} \tag{2.2.4b}$$

The general solution to the second-order equation 2.2.3 has the form of $e^{\pm\frac{z}{\sqrt{D_{\mathrm{n,p}}\tau_{\mathrm{n,p}}}}}$. In order to solve the equation 2.2.4, appropriate boundary conditions are required, which will be explained in the next section.

The collection function ($\eta_{\mathsf{C}}(z)$)

The collection function (η_{C}) is the probability of an electron generated at the point z to be collected [21]. The collection function at the point z is the ratio of the dark carrier concentration ($n(z)$) to the carrier concentration in its thermal equilibrium value ($n_0(z)$) [4]:

$$\eta_{\mathrm{C}}(z) = \left(\frac{\Delta n(z)}{n_0(z)}\right) \Bigg/ \left(\frac{\Delta n(-w_{\mathrm{a}})}{n_0(-w_{\mathrm{a}})}\right) \tag{2.2.5}$$

where $\Delta n(-w_{\mathrm{a}})$ is the injected carrier concentration at the edge of space charge region. Inserting the equation 2.2.5 into the continuity equation (Eq. 2.2.3) yields [21]:

$$\frac{d}{dz}\left(\frac{d}{dz}\eta_{\mathrm{C}}(z) - \frac{\eta_{\mathrm{C}}(z)}{k_{\mathrm{B}}T}\left(qE(z) - \frac{d}{dz}\chi(z)\right)\right) - \frac{\eta_{\mathrm{C}}^2(z)}{L_{\mathrm{n}}^2} = 0 \tag{2.2.6}$$

where L_{n} is the diffusion length and is the average distance that a minority carrier will diffuse before recombining [17, 22]. In order to determine the collection function of the minority carriers, the following boundary conditions must be satisfied:

1. The electric field in the space charge region collects all the generated carriers within this region. In other words, the collection function within the depletion region is assumed to be unity [4]:

$$\eta_{\mathrm{C}}(z = -w_a) = 1 \tag{2.2.7}$$

2. Far from the junction, the collection function extends to an interface characterised by a surface recombination velocity of S_{n} [18]:

$$\frac{d}{dz}\eta_{\mathrm{C}}(z)\bigg|_{z=-d_{\mathrm{a}}} = \frac{S_{\mathrm{n}}}{D_{\mathrm{n}}}\,\eta_{\mathrm{C}}(z) \tag{2.2.8}$$

where d_{a} is the absorber thickness. The equation 2.2.6 will be used in chapter 4 to study

the influence of different bandgap gradients on the collection function.

2.2.2. Transport equation across the interface

Thermionic emission across a potential barrier

Thermionic emission is a process in which the majority carriers at the interface have to overcome a barrier (ϕ_{b}) [16]. For an electron barrier, the total current across the barrier is the current density of electrons from the buffer to the absorber minus the current density from the absorber to the buffer layer [4, 23]. The transport over an interface is proportional to the carrier densities and can be written as [4, 23]:

$$J_{TE} = v_{\mathrm{th}} \left[n(0^+) - n(0^-) exp(-\frac{\phi_{\mathrm{b}}}{k_{\mathrm{B}}T}) \right] \tag{2.2.9}$$

Here, v_{th} is the thermal velocity, $n(0^+)$ and $n(0^-)$ are the electron densities in the buffer layer and the absorber layer, respectively. The ϕ_{b} is the electron barrier height. The equation 2.2.9 indicates that in order to overcome the barrier height, a high density of electrons has to be present at the interface, or the temperature must be high. The electron density in the buffer layer can be expressed as [23]:

$$n(0^+) = n(0^-)\, exp\!\left(-\frac{\phi_{\mathrm{b}}}{k_{\mathrm{B}}T}\right) exp\left(\frac{\Delta E_{\mathrm{Fn}}}{k_{\mathrm{B}}T}\right) \tag{2.2.10}$$

Here ΔE_{Fn} is the drop of the electron Fermi level at the interface [4]. The substitution of equation 2.2.10 into equation 2.2.9 changes the thermionic current to [23]:

$$J_{\mathrm{TE}} = J_{0,\mathrm{TE}} \left[exp\left(\frac{\Delta E_{\mathrm{Fn}}}{k_{\mathrm{B}}T}\right) - 1 \right] \tag{2.2.11}$$

with the saturation current density [16]:

$$J_{0,\mathrm{TE}} = v_{\mathrm{th}} n(0^-) exp\left(-\frac{\phi_{\mathrm{b}}}{k_{\mathrm{B}}T}\right) = qA^* T^2 exp\left(-\frac{\phi_{\mathrm{b}}}{k_{\mathrm{B}}T}\right). \tag{2.2.12}$$

Here, A^* is the Richardson constant which depends on the materials involved at the interface [19]. The equation 2.2.11 describes the charge transport over a barrier at the interface and is very similar to the equation 2.4.1 which describes the charge transport in the pn junctions. However, the expression of the saturation current density for the thermionic emission ($J_{0,\mathrm{TE}}$) is proportional to T^2 (see Eq.2.2.12).

2.3. Recombination types

Upon illumination or forward-biasing the equilibrium state of the junction is disturbed and the excess carrier density is generated [16]. The system wants to restore the equilibrium state through a process inverse to generation [16]. If a photon is emitted then the recombination process is classified as a radiative recombination. In a non-radiative recombination the excess energy is dissipated by transferring the energy to phonons [16]. The recombination can be divided into band-to-band recombination, Auger recombination and Shockley-Read-Hall recombination [4]. In the following, a description of the band-to-band recombination process and Shockley-Read-Hall recombination process will be given. The Auger recombination will not be discussed here, since it is not an active process in CIGSe absorbers [4].

2.3.1. The radiative band-to-band recombination

In the band-to-band recombination, the electron that occupies a higher energy state than it would under thermal equilibrium makes a transition to a lower state [22]. For a band-to-band transition to take place, the presence of an electron and a hole is required simultaneously. Therefore, the recombination process is the product of the electron and hole densities and the net recombination rate can be written as [4]:

$$R = U_{\mathrm{n}} - G_0 = B(n\,p - n_0\,p_0) \tag{2.3.1}$$

where U_{n} is the recombination rate, G_0 is the generation rate in equlibrium, B is the radiative recombination constant and n_0 and p_0 are the densities of the electrons and holes in thermal equilibrium, respectivly [4]. In the non-equilibrium condition the carrier concentrations can be written as:

$$n = n_0 + \Delta n \tag{2.3.2a}$$

$$p = p_0 + \Delta p \tag{2.3.2b}$$

where Δp and Δn are the excess carrier concentrations of holes and electrons, respectively. The recombination rate then under low-level injection $\Delta n = \Delta p \ll (n_0 + p_0)$ can be written:

$$U_{\mathrm{n}} = B(n_0 + p_0)\Delta n = \frac{\Delta n}{\tau} \tag{2.3.3}$$

where τ is the characteristic lifetime and is defined as $\tau = \frac{1}{B(n_0+p_0)}$ [22].

2.3.2. Shockley-Read-Hall recombination

In the Shockley-Read-Hall recombination, defect states within the bandgap of the semiconductor are responsible for recombination. This is in contrast to the band-to-band transition, where the conduction band and the valence band are involved in the process. The recombination involves four transitions as given in equation 2.3.4. The processes caused by capture and re-emission of electrons and holes [24].

$$C_{\mathrm{n}} = \sigma_{\mathrm{n}}\,v_{\mathrm{n}}(N_{\mathrm{t}} - n_{\mathrm{t}})\,n \tag{2.3.4a}$$

$$C_{\mathrm{p}} = \sigma_{\mathrm{p}}v_{\mathrm{p}}\,n_{\mathrm{t}}\,p \tag{2.3.4b}$$

$$E_{\mathrm{n}} = \beta_{\mathrm{n}}\,n_{\mathrm{t}} \tag{2.3.4c}$$

$$E_{\mathrm{p}} = \beta_{p}(N_{\mathrm{t}} - n_{\mathrm{t}}) \tag{2.3.4d}$$

Here, $(N_{\mathrm{t}}$ - $n_{\mathrm{t}})$ is the density of unoccupied defect states, C_{n} and C_{p} are the capture rates of electrons and holes, $E_{\mathrm{n/p}}$ is the emission rate, and β_{n} and β_{p} the emission coefficients of electrons and holes, respectively. With the aid of the continuity equation and charge neutrality equation, the net recombination through a single trap state is [16]:

$$R = U - G_0 = \frac{n\,p - n_{\mathrm{i}}^2}{\tau_{\mathrm{p}}(n^* + n) - \tau_{\mathrm{n}}(p^* + p)} \tag{2.3.5}$$

where $n^* = N_{\mathrm{C}}\exp\left(\frac{E_T - E_C}{k_{\mathrm{B}}T}\right)$ and $p^* = N_{\mathrm{V}}\exp\left(\frac{E_V - E_T}{k_{\mathrm{B}}T}\right)$ are the auxiliary densities with N_{C} and N_{V} the effective densities of states in the conduction and valence band, respectively [25]. The minority carrier lifetimes τ_{p} and τ_{n} for holes and electrons respectively are defined as [4]:

$$\tau_{\mathrm{p}} = \frac{1}{\sigma_{\mathrm{p}}\nu_{\mathrm{th}}N_{\mathrm{t}}} \text{ and } \tau_{\mathrm{n}} = \frac{1}{\sigma_{\mathrm{n}}\nu_{\mathrm{th}}N_{\mathrm{t}}} \tag{2.3.6}$$

Here, $\sigma_{\mathrm{p,n}}$ is the capture cross section for holes/electrons and ν_{th} is the thermal velocity. The SRH recombination can be further extended for interface recombination [15]. In this case the term $\tau_{\mathrm{p/n}}$ is replaced by $S_{\mathrm{n/p}}^{-1}$. The $S_{\mathrm{n/p}}$ stands for the recombination velocity at the interface [15]. More information is given in section 2.5.3.

2.4. IV characteristics

When a solar cell is illuminated, the photo-gernerated carriers leads to a splitting of the Fermi levels. The electric field at the junction separates the electron-hole pairs by driving the minority carriers across the junction. Illuminating the junction, results in a considerable increase of the minority carriers, while the increase of the majority carriers

is negligible [16]. Therefore, the current density of a non-illuminated diode is modified by the photo-generated minority carriers flux ($|J_{\mathrm{ph}}|$) which add up a negative flux of charges:

$$J_{\mathrm{tot}} = J_{\mathrm{diode}}(V) - J_{\mathrm{ph}} = J_0 \left(exp\big(\frac{qV}{A\,k_{\mathrm{B}}T}\big) - 1 \right) - J_{\mathrm{ph}} \tag{2.4.1}$$

with the saturation current density of (J_0):

$$J_0 = J_{00}\,exp\left(-\frac{E_{\mathrm{A}}}{A\,k_{\mathrm{B}}T} \right). \tag{2.4.2}$$

where J_{00} is the reference current density and is weakly temperature dependent, E_{A} is the activation energy of the saturation current density, A is the diode quality factor. The photo-current density (J_{ph}) is defined as:

$$J_{\mathrm{ph}} = \eta(V)\,J_{\mathrm{SC}} \tag{2.4.3}$$

where $\eta(V)$ is the external collection efficiency and varies between [0, 1]. In the ideal case it is assumed that $\eta(V)$ is not voltage dependent and is equal to 1, within all voltage ranges [26]. The influence of the collection efficiency on the solar cell parameter will be discussed in chapter 4.

2.4.1. Solar cell parameters

To characterize a solar cell, a few parameters are briefly introduced in the following:

- open-circuit voltage (V_{OC}) is the voltage that can be achieved at $J = 0$.
  If the current density is set to zero in equation 2.4.1, the V_{OC} will be:

$$V_{\mathrm{OC}} = \frac{A\,k_{\mathrm{B}}T}{q}\,ln\left(\frac{J_{\mathrm{ph}}}{J_0} + 1 \right) \tag{2.4.4}$$

  Another term which is used in this dissertation is the V_{OC}-deficit. The V_{OC}-deficit is the difference between the open-circuit voltage and the bandgap value (E_{g}/q - V_{OC}). For low-gap CIGSe absorbers ($E_{\mathrm{g}} < 1.2$ eV) the V_{OC}-deficit is smaller than 0.5 V [2]. For wide-gap CIGSe absorbers ($E_{\mathrm{g}} > 1.2$ eV), the V_{OC} saturates and the V_{OC} - deficit increases to values above 0.7 V [2].

- short-circuit current density (J_{SC}) is the current density upon illumination at zero bias.

- maximum power point is the point where the product of the $V\,J(V)$ has its maximum

value ($P_{\mathrm{m}} = V_{\mathrm{mpp}} \, J_{\mathrm{mpp}}$). The maximum point can be found by a partial differential with respect to voltage [4, 26]:

$$\left. \frac{dJ(V)}{dV} \right|_{Vmpp} = -\frac{J_{\mathrm{mpp}}}{V_{\mathrm{mpp}}} \tag{2.4.5}$$

• fillfactor (FF) is the ratio of the maximum power density (P_{m}) to the product $J_{\mathrm{SC}} V_{\mathrm{OC}}$

$$FF = \frac{J_{\mathrm{mpp}} \, V_{\mathrm{mpp}}}{J_{\mathrm{SC}} \, V_{\mathrm{OC}}} \tag{2.4.6}$$

the fillfactor describes how squared the JV curve is [22]. and finally

• conversion efficiency (η) is the ratio of the maximum power density to the incident light power density which is 1000 Wm^{-2} (P_{i}) under the AM1.5G.

$$\eta = \frac{J_{\mathrm{mpp}} \, V_{\mathrm{mpp}}}{P_{\mathrm{i}}} \tag{2.4.7}$$

2.4.2. External quantum efficiency

The external quantum efficiency is the ratio of charge carriers that are collected to the amount of the incident photons per wavelength, per unit area. The EQE measurement is a valuable method to diagnose the origin of recombination losses. For instance, if the sample is limited by the interface recombination, then the photo-generated carriers recombine at the interface and this can be observed as a poor EQE signal at all wavelength regions. If the diffusion length of the minority carriers (L_{n}) is not large enough then the photo-generated carriers cannot be collected completely and reduces the EQE signal in the long wavelength region [27]. From the EQE results, the optical bandgap of the absorber can be determined by linearly fitting the long wavelength slope of the EQE spectrum, since the photons with energy smaller than the bandgap value cannot be absorbed ($h\nu = E_{\mathrm{g}}$).The EQE can be calculated with the collection function ($\eta_{\mathrm{C}}(z,V)$):

$$EQE = \int \eta_C(z, V) g(z, \lambda) dz \tag{2.4.8}$$

where $g(z, \lambda)$ is the normalized generation rate [4]. The maximum value of the EQE that can be achieved is one, however due the optical losses and electronic losses the value is smaller. In order to minimize the optical losses originated from the reflection losses usually an anti-reflection coating is used. From an absolute value of the EQE and integration over the solar spectrum the short-circuit current can be calculated:

$$J_{\mathrm{SC}} = q \int EQE(\lambda) \phi(\lambda) d\lambda \tag{2.4.9}$$
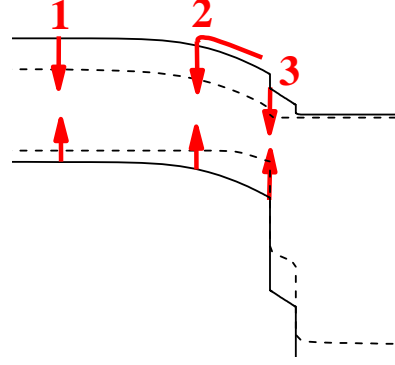
Figure 2.2: Band diagram under applied bias voltage for an absorber/buffer/window hetero-structure showing the possible recombination paths. The arrows indicate a recombination processes, (1) in the quasi-neutral region, (2) space charge region, (3) at the absorber/buffer interface. The image is adapted from reference [28].

Here, the photon flux ($\phi(\lambda)$) is the AM1.5G flux density per unit wavelength. The calculation of the short-circuit current density by integration over the EQE is advantageous since the effect of the shadowing from the finger grids can be neglected.

2.5. Regions of recombination

The recombination can occur at different regions of the solar cell. In figure 2.2, different recombination paths in a Cu(In,Ga)Se$_2$ cell under a small applied bias voltage are depicted. The recombination in the quasi neutral region (QNR) (path number 1), in the space charge region (SCR) (path number 2), and recombination at the buffer/absorber interface (path number 3) are indicated with arrows. In a solar cell all recombination paths are active in parallel and contribute to the diode current, however one recombination path is always dominant [4].

The total diode current density is described by [4]:

$$J_{diode} = qD_{\mathrm{n}}\frac{d}{dz}n(z)\big|_{z=-w_a} + q\int_{-w_a}^{0}(U_n(z) - G_0(z))dz + q\,R^{if} \qquad (2.5.1)$$

The right hand side of equation 2.5.1 describes the contribution of the QNR, SCR and interface recombination, respectively. In the following for each recombination path the net recombination rate is written and the open-circuit voltage is given.

2.5.1. Recombination in the quasi-neutral region

If the carrier lifetime is long, then the injected carriers can pass the SCR without recombination and enter into the QNR region. For a deep defect present in the bulk of the absorber the relation $p \gg n, p^*, n^*$ and $p = N_{\mathrm{A,a}}$ is valid. With these assumptions the equation 2.3.5 becomes [4]:

$$R = \frac{n\,p}{\tau_n\,N_{A,a}} \tag{2.5.2}$$

For an absorber limited by recombination in the QNR region, the V_{OC} can described by [29]:

$$V_{OC} = \frac{E_g}{q} - \frac{k_B T}{q}\,ln\left(\frac{q D_n N_{C,a}\,N_{V,a}}{J_{SC}\,N_A\,L_n^2}\right) \tag{2.5.3}$$

From equation 2.5.3, it can be understood that with the enhancement of the doping density the V_{OC} increases, and the extrapolation of V_{OC} to $T \to 0$ K leads to $E_A = E_g$. For a dominant recombination in the QNR, the diode quality factor is 1.

2.5.2. Recombination in the space charge region

The location of a maximum recombination is at the position where the condition

$$n\,\tau_n^{-1} = p\,\tau_p^{-1} \tag{2.5.4}$$

is fulfilled and this is within the SCR [4]. Close to the point of maximum recombination, it holds $n, p \gg n^*, p^*$. This simplifies the equation 2.3.5 to [4]:

$$R = \frac{n\,p - n_i^2}{\tau_n\,p + \tau_p\,n} \tag{2.5.5}$$

The recombination current in the SCR region can be obtained by integrating the recombination rate (Eq. 2.3.5) over the volume of the space charge region [4], this yields:

$$J(V) = \frac{\pi k_B T}{2\,F_m}\left(\frac{N_{C,a}\,N_{V,a}}{\tau_{n,a}\,\tau_{p,a}}\right)^{\frac{1}{2}} exp\left(-\frac{E_g}{2\,k_B T}\right) exp\left(\frac{q V}{2\,k_B T}\right) \tag{2.5.6}$$

The equation 2.5.6 shows that for a cell limited by space charge region the diode quality factor is 2, which means that the quasi Fermi levels of electrons and holes move symmetrically with respect to the dominating defect level under applied bias voltage [4, 29]. The F_m is the electrical field at the position of maximum recombination and is dependent on the doping density and the built-in voltage [4]. The V_{OC} can be written [29]:

$$V_{OC} = \frac{E_g}{q} - \frac{2\,k_B T}{q}\,ln\left(\frac{\pi\,k_B T\,D_n\,\sqrt{N_{C,a}N_{V,a}}}{J_{SC}\,F_m\,L_n^2}\right) \tag{2.5.7}$$

From equation 2.5.7, it can be understood that the extrapolation of V_{OC} to T $\to 0$ K results in an activation energy equal to the bandgap. Similar to equation 2.5.3, the equation 2.5.7 scales logarithmically with the doping density [29].

2.5.3. Recombination at the interface

The net recombination rate for a recombination at the interface is given by [15]:

$$R = U - G_0 = \frac{n^{if} \, p^{if} - n_i^2}{S_p^{-1}(n^* + n^{if}) - S_n^{-1}(p^* + p^{if})} \tag{2.5.8}$$

where p^{if} and n^{if} are the densities of holes and electrons at the interface. With the assumption that the absorber is inverted, i.e. that $n^{if} \gg p^{if}$ at the interface, the quantities n^* and p^* can be neglected. Hence the recombination rate reduces to [15]:

$$R^{if}(z) \approx p_{a_{z=0}}(z) \, S_p \tag{2.5.9}$$

with the surface recombination velocity [4]:

$$S_p = \tau_p^{-1} \, N_d^{-\frac{1}{3}}. \tag{2.5.10}$$

From the recombination rate, the current density can be calculated and the saturation current density for an absorber/buffer/window hetero-structure is [15]:

$$J_0 = qS_p N_{V,a} exp\left(-\frac{E_{n,w}}{k_B T}\right) exp\left(-\frac{E_A}{A \, k_B T}\right) \tag{2.5.11}$$

with the reference current density J_{00} [15]:

$$J_{00} = qS_p N_{V,a} exp\left(-\frac{E_{n,w}}{k_B T}\right). \tag{2.5.12}$$

while J_{00} does not have to be temperature dependent, the derived equation 2.5.12 by Wihelm et al. [15] shows strong temperature dependency. To eliminate the temperature dependency, it can be assumed that all the dopants are ionized and substitute the exp-term with the Boltzmann approximation [30]. The diode quality factor of a sample with a dominant interface recombination is a value between 1 and 2 [15]. The parameters such as doping density, built-in voltage, buffer thickness have an impact on the diode quality factor [15]. For dominant recombination at the CdS/Cu(In,Ga)Se$_2$ interface, the open-circuit voltage is [15]:

$$V_{OC} = V_{bi} - \phi_a^{if}(V = V_{OC}) + \frac{qN_{D,b}d_b^2}{2\epsilon_b} - \frac{d_b}{\epsilon_b}\sqrt{2\epsilon_a N_{A,a}q\phi_a^{if}(V = V_{OC})} \tag{2.5.13}$$

with the electrostatic potential ($\phi^{if}(V = V_{OC})$) [15]:

$$q\phi_a^{if}(V = V_{OC}) = k_B T \, ln\left(\frac{q \, S_p N_{V,a}}{J_{SC}}\right) - E_{p,a}. \tag{2.5.14}$$

As can be seen in equation 2.5.13, with the increase of the doping density the V_{OC} is being reduced. This is in contrast to the previous cases of QNR and SCR recombination, where the increase of the doping density was accompanied with the increase of the V_{OC} (Eq. 2.5.7 and 2.5.3).

In section 2.1, an introduction to the absorber/buffer/window hetero-structure was given. In the following, the challenges of wide-gap CIGSe cells are introduced, and a solution will be given.

2.6. Cu(In$_x$,Ga$_{1-x}$)Se$_2$ solar cells

The increase of the gallium concentration in a Cu(In$_x$,Ga$_{1-x}$)Se$_2$-absorber (CIGSe) increases the bandgap value. The bandgap of the Cu(In$_x$,Ga$_{1-x}$)Se$_2$ absorber changes according to the following equation [31]:

$$E_{\text{g}}(x) = (1-x)E_{\text{g}}^{CuInSe_2} + x\,E_{\text{g}}^{CuGaSe_2} - b\,x(1-x) \qquad (2.6.1)$$

where b is the bowing parameter and it's value is in the range of $0 \leq b \leq 0.3$ eV [31]. As the gallium concentration increases, the conduction band shifts to higher values and the valence band remains constant [32]. In figure 2.3 the effect of low and high gallium concentration on the band diagram is shown. For a low-gap CIGSe absorber, the band offset between the CIGSe and the CdS is positive ($\Delta E_{\text{C}} > 0$). This means that a large density of electrons is available at the hetero-interface and the absorber surface is inverted (Fig. 2.3(a)) [33]. The inversion induces a large hole barrier and suppresses the recombination at the interface [8]. In contrast to the low-gap CIGSe cells, the wide-gap CIGSe cells have a negative conduction band offset to CdS ($\Delta E_{\text{C}} < 0$) (Fig. 2.3(b)). The negative coduction band offset reduces the inversion strength and brings a high density of holes at the interface. As a result the interface recombination increases and the open circuit voltage does not increase linearly with increasing the bandgap [6, 34, 35].

But besides the detrimental band alignment of wide gap CIGSe cells at the hetero-interface [8], the low open-circuit voltage has other origins as well. For instance, it has been claimed that as the gallium concentration of the CIGSe absorber increases, the formation of Cu-poor phases is impeded. The existence of such phases is necessary to shift the valence band edge downward and increase the open-circuit voltage. One solution to lower the valence band edge is to sulfurize the absorber surface [36]. In the last few years, it has been shown that post-deposition treatement of alkalis is also a helpful method to increase the open-circuit voltage [36–38]. This matter will be discussed in the next section.
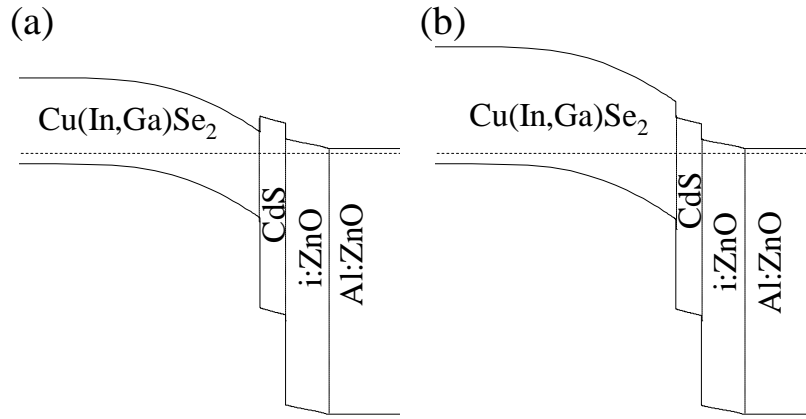
Figure 2.3.: The band diagram of $Cu(In_x,Ga_{1-x})Se_2$ solar cell with different gallium concentration, (a) low-gap, (b) wide-gap. As the gallium concentration increases, the conduction band offset changes from a spike to a cliff. All parameters except for the electron affinity and the bandgap of CIGSe are identical.

2.7. Review on the post-deposition treatment of alkalis

For many years sodium was assumed to be the sole alkali that is required to improve the efficiency of CIGSe devices. In the last few years, it has been found that besides sodium heavier alkali such as potassium, rubidium and caesium can further improve the efficiency [36–38]. The post-deposition treatment of alkalis (K, RbF, and CsF) improves mostly the V_{OC} and FF [36–38]. Jackson et al. have shown that a post-deposition treatment of the potassium on CIGSe absorbers independent of the gallium concentration increases the V_{OC} and can partially overcome the V_{OC} saturation [39]. In order to explain the increase of the V_{OC}, different explanations are given which are summarized in the following:

1. **Increase of the minority carrier lifetime** It has been reported that the post-deposition of alkalis on small bandgap CIGSe cells increases the minority carrier lifetime [36, 40–43]. Kato et al. have discovered that as the alkali gets heavier the transients of the TRPL are getting longer. The V_{OC} is logarithmically dependent on the minority carrier lifetime [44], thus an increase of the V_{OC} with the increase of the minority carrier lifetime can be expected.

2. **Influence on the doping density** The measurements of the doping density on alkali-treated and untreated cells have shown that the post-deposition treatment of alkali increases the doping density ($N_{A,a}$) of the low-gap CIGSe cells [42, 43, 45]. Usually, the low-gap CIGSe cells are limited by the recombination in the QNR or SCR, and for those cells the V_{OC} increases logarithmically with the $N_{A,a}$ (Eq.2.5.3).

3. **Modification of the band diagram** One model to explain the increase of the V_{OC} has been suggested by Pianezzi, claiming that the post-deposition treatment of potassium induces a high density of donor states at the interface [43]. The high

density of donor states shift the conduction band closer to the Fermi level and improve the inversion [43]. At the same time, it has been discovered that the post-deposition treatment of the alkalis depletes the copper content at the surface and forms a new surface layer [10–12, 37, 46, 47]. Handick et al. measurements indicated that the conduction band and the valence band are shifted away from the Fermi level when the sample is treated with KF-PDT [10]. Pistor et al. have found that the valence band edge of the KF-treated absorber surface is shifted downward [12]. For RbF-treated absorbers, the same effect has been reported [11]. Lowering the valence band edge depletes the holes at the interface and improves the V_{OC}.

In chapters 5 and 6 the influence of the post-deposition treatment of alkalis on the band diagram will be investigated and the proposed models will be simulated.

3. CIGSe solar cell preparation and characterization methods

In order to prepare Cu(In,Ga)Se$_2$ thin film solar cells, a stack of functional layers needs to be deposited on a substrate (Fig. 3.1). In section 3.1 different substrates used for this thesis are presented. The deposition methods for the individual layers are discussed in sections 3.2 through 3.5. Characterization and simulation methods for the completed solar cells are introduced in sections 3.6 and 3.7, respectively.

3.1. Substrate

A number of substrate materials can be used for the preparation of highly efficient CIGSe solar cells, among them polymer foils and various kinds of glasses [37, 48]. However, current champion cells are made with soda lime glass [48]. The latter was also used for this thesis together with two other types of glasses, which are described in the following subsections.

3.1.1. Soda-lime glass substrate (SLG)

Soda-lime glass (SLG) is a suitable substrate for CIGSe solar cells mainly because of its well-matched thermal expansion coefficient, smooth surface, and low production costs [49, 50]. Another advantage is that SLG delivers sodium at elevated temperatures, which
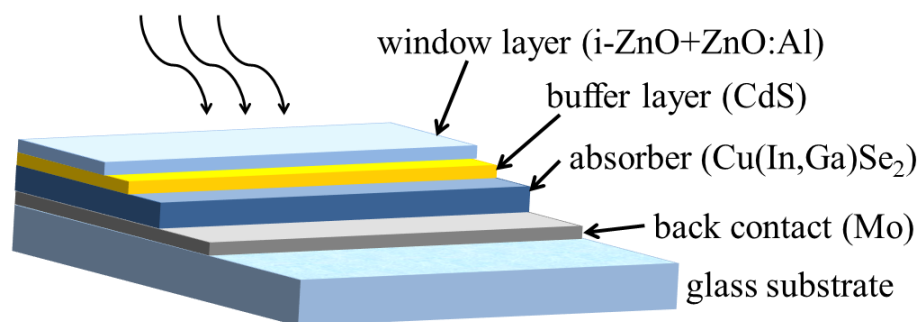
Figure 3.1.: Schematic of a Cu(In,Ga)Se$_2$-based solar-cell device.

incorporates in the absorber during its deposition and enhances the solar cell efficiency [50–53]. It has been shown that sodium passivates the donor defects at the grain boundary and increases the doping density. This effect increases the open-circuit voltage and fillfactor [50, 54, 55].

3.1.2. Sodium-free substrate

While sodium incorporation in the CIGSe absorber is required for high solar cell performance [56], the amount of sodium diffusing into the absorber can hardly be controlled when using plain soda-lime glass as a substrate [55]. However, for some of the experiments presented in this thesis control of the sodium content of the absorber was necessary, especially for the investigation of the influence of alkali metals. In these cases, SLG coated with a SiO_xN_y layer as a diffusion barrier for alkali metals was used. The sodium-free substrate and SLG substrates were provided by Guardian Industries.

3.1.3. High temperature substrate

One of the drawbacks of conventional SLG is that it deforms at temperatures above 850 K [2]. Lately, a specific kind of glass is available that tolerates temperatures above 850 K and is beneficial to improve the solar cell parameters of wide-gap CIGSe cells [2]. Therefore, some of the samples used for this thesis, were grown on more temperature-stable glass. This specific glass is manufactured by Schott AG and contains sodium, which releases during absorber growth [2].

3.2. Back contact

For all solar cell samples mentioned in this thesis a molybdenum layer covering the substrate was used as a back contact. During absorber deposition a thin $MoSe_2$ layer is created at the interface leading to good adhesion of the absorber layer [57]. No further chemical reaction whatsoever between molybdenum and CIGSe absorber occurs and good ohmic contact is readily established under suitable deposition conditions [58, 59]. The molybdenum-coated substrates were provided by the industry and no further optimization on the molybdenum was performed in the lab.
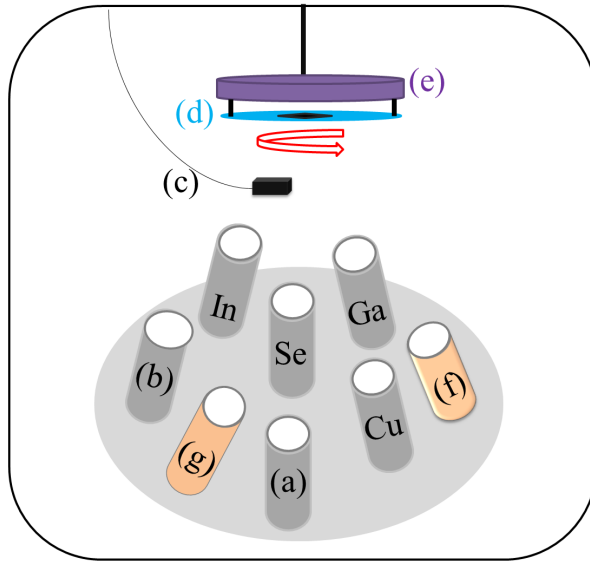
Figure 3.2.: Schematic of the co-evaporation chamber used for growing CIGSe absorbers, (a) crucible for KF/RbF or CsF, (b) crucible for NaF, (c) quartz crystal microbalance (QCM), (d) substrate holder, (e) substrate heater, (f) infrared and red-light lasers, (g) detector for in-situ laser light signals.

3.3. Growth of Cu(In,Ga)Se$_2$ absorber

3.3.1. The evaporation chamber

The Cu(In,Ga)Se$_2$ absorber layers investigated in this thesis were deposited by co-evaporation of the individual elements in the high vacuum chamber BAK600. The chamber is equipped with a rotary vane pump and an oil diffusion pump which establish a minimum pressure of the order of 10^{-6} mbar during the deposition processes and a base pressure of 1×10^{-7} mbar. A schematic diagram of the chamber interior is shown in figure 3.2. Effusion cells dedicated to the evaporation of copper, indium, gallium and selenium, respectively, are arranged within the chamber together with two additional cells for the evaporation of alkali fluorides. Prior to deposition, the evaporation rates were determined with the help of a quartz microbalance, which is mounted in the vicinity of the sample holder. Both the effusion cells and the sample holder are equipped with shutters. The sample holder is rotated during the deposition process. The temperature of the samples is monitored by a thermocouple, which is positioned at the back side of the sample holder, and can be controlled by heating from the back side. A laser light scattering system consisting of a red (650 nm) and an infrared (1550 nm) laser together with a light detector connected to a lock-in amplifier is installed inside the chamber in order to monitor the thickness of the layers during deposition.

3.3.2. Growth process of Cu(In,Ga)Se$_2$ absorber

The absorber layers were deposited in so-called three-stage processes. For this thesis, two process variations were used (Fig. 3.3(a-b)): one which will be referred to as the multi-stage process [60], and one which will be named the modified process. In the multi-stage process, the first stage starts with the evaporation of indium, gallium and selenium at a substrate temperature of 673 K. The evaporation rate of selenium is several times higher than the sum of the metal rates. During the first stage, an (In,Ga)$_2$Se$_3$-layer is created, that can be monitored by interference oscillations of the scattered light intensity of the infrared laser [61]. In the second stage the substrate temperature is increased to 898 K and – in case of the multi-stage process – only copper and selenium are evaporated until the copper content of the deposited layer exceeds the stoichiometric composition of CIGSe. The copper-rich phase, which is then present, has a higher surface roughness and an enhanced emissivity compared to the previous, copper-poor phase. Therefore, the crossing of the stoichiometric point can be detected as an increase of the scattered light intensity of the red laser as well as an increase of the sample heater temperature [62, 63]. The second stage continues until the [Cu]/([In]+[Ga]) (CGI) ratio reaches to 1.09. In the third stage, again indium, gallium and selenium are evaporated in order to return to the copper-poor phase. Once more, the crossing of the stoichiometric point is visible in the laser light signal and in the sample heater temperature. After that, the substrate temperature is kept constant for 250 seconds in a selenium atmosphere, before the sample is slowly cooled down. The final thickness of these absorbers are between 2.2 - 2.5 μm and have a CGI of 0.8 - 0.93.

The modified deposition process (Fig. 3.3(b)) was used for growing absorber layers on SLG with [Ga]/([Ga]+[In] (GGI) above 0.65. In the modified deposition process, gallium is evaporated in all stages. In the first stage, indium and gallium are evaporated in the presence of selenium. Due to the presence of gallium in the second stage, the first stage is shorter to obtain the same overall thickness as in the regular process, and the second stage needs to be longer until the copper-rich phase is reached. Finally, in the third stage, the evaporation ratio of gallium to indium was changed to reduce the front gradient. The aim of these modifications was to moderate the gallium gradient throughout the absorber layer. The gallium gradient will be discussed in more detail in chapter 4.

3.3.3. Post-deposition treatments of heavy alkalis

One of the main objectives of this thesis is the investigation of the influence of heavy alkali metals on the absorber, which were introduced by means of post-deposition treatment. Subsequent to the growth of the absorber layer the samples were cooled down to 723 K and the alkali metals were deposited from dedicated evaporation sources in a selenium atmosphere. Using this procedure, samples with differing gallium content were exposed to
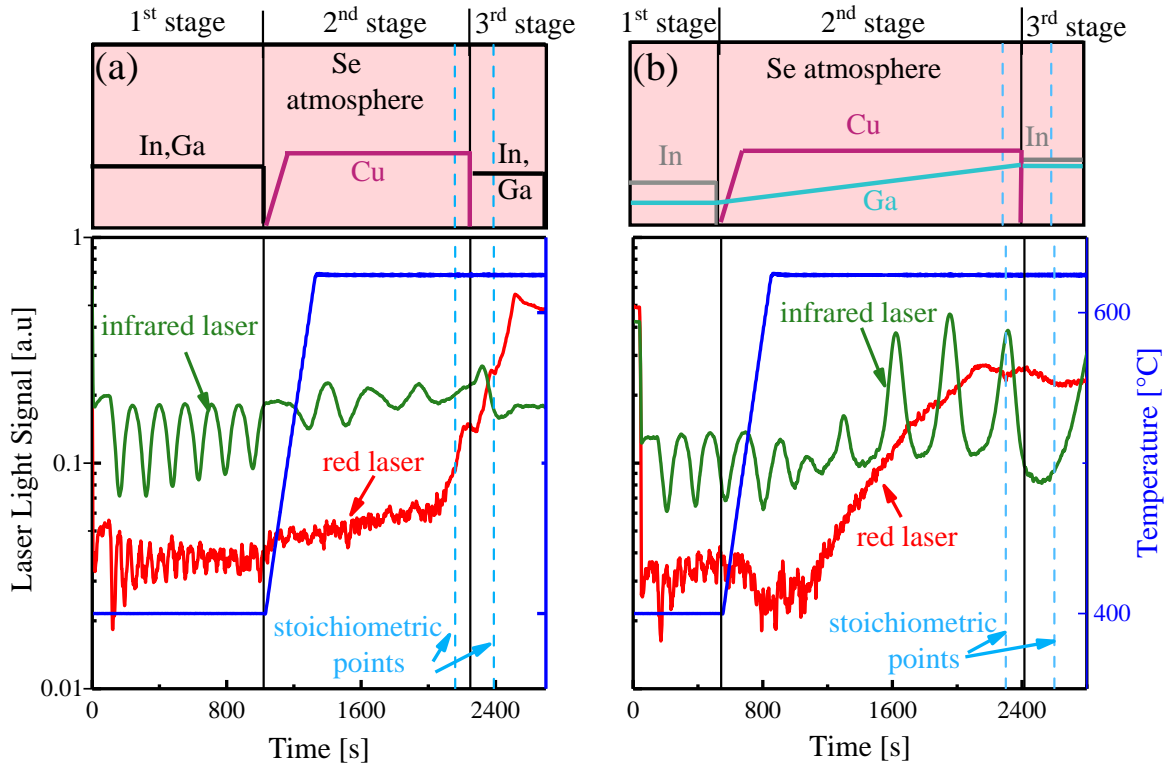
Figure 3.3.: Deposition recipe for CIGSe absorber (a) multi-stage process,(b) modified recipe. In the modified recipe (b), the first stage is shorter and the second stage is longer compared to deposition recipe (a). The modified recipe (b) is used for deposition of high Ga-content CIGSe absorbers (GGI > 0.65) on SLG.

different combinations and varying amounts of alkali metals. An overview of the prepared samples together with the chapters of this thesis containing the experimental results obtained from the respective samples is given in Table 3.1.

Table 3.1.: List of samples investigated in this work

Chapter	Substrate	PDT	GGI
4	Na-containing SLG	-	0.8
5	Na-containing SLG	KF/RbF/CsF	0.3 - 0.8
6	Na-containing SLG	KF/RbF/CsF	0.3 and 0.8
7	sodium-free substrates	NaF+KF	0.3 - 0.85
7	High-Temperature substrates	RbF	0.3 - 0.85

3.4. Buffer layer

CIGSe solar cells with the highest efficiencies have been achievd by a CdS buffer layer between the absorber and the window [36–38]. Despite a few drawbacks of CdS – namely its toxicity [64] and the relatively small band gap [65] – using it as a buffer layer is beneficial for the solar cell performance in several ways. Among them are the protection

of the absorber against the sputter damage from the window deposition [66] and the removal of shunts [67]. The CdS buffer layer was grown on the absorber in a chemical bath containing a solution of thiourea ($CS(NH_2)_2$), cadmium acetate ($Cd(CH_3COO)_2$) and ammonia (NH_3) [68]. A uniform CdS film of approx. 50 nm thickness was achieved after dipping the sample for 8 minutes at a bath temperature of 333 K. The thiourea and cadmium acetate serve as sulfur and cadmium sources, respectively. The ammonia provides the proper pH for the chemical reaction and simultaneously removes unwanted secondary phases like Cu_2Se and oxides from the absorber surface [67]. The removal of these secondary phases enhances the type inversion and consequently the efficiency [69].

3.5. Window layer and front contact

In the samples investigated in this thesis, the window layer consists of two sub-layers: 100 nm of intrinsic ZnO (i-ZnO) and 300 nm of aluminium doped ZnO (ZnO:Al). Both layers were deposited by means of RF sputtering at a substrate temperature of 413 K. Introduction of the i-ZnO layer below the actual ZnO:Al window layer with a band gap of 3.6 eV reduces shunts and enhances the open-circuit voltage of the final solar cell [70, 71]. Finally, a Ni/Al/Al grid was deposited as front contact by means of e-beam evaporation. Afterwards, individual solar cells were defined through mechanical scribing. A typical cell area is 0.5 cm^2 with little variation among the samples. None of the solar cells discussed in this thesis have received an anti-reflection coating.

3.6. Characterization method

3.6.1. Determination of the collection efficiency ($\eta(V)$)

As shown in equation 2.4.3, a voltage dependent collection efficiency will cause the photo-current to be voltage dependent. A voltage dependent photo-current (Eq. 2.4.3) reduces the FF and the V_{OC} [72]. In order to analyze the collection efficiency, the JV-curves of a sample were measured at different light intensities. But the parasitic losses such as series resistance (R_s) lowers the actual $\eta(V)$. Therefore, the measured voltage must be corrected for R_s to give the correct voltage across the absorber by [72, 73]:

$$V' \longrightarrow V - R_s J \tag{3.6.1}$$

In this thesis the R_s was determined in dark. The collection efficiency can be calculated by [72, 73]

$$\eta(V') = \frac{J(V', J^n) - J(V', J^m)}{J_{SC}^n - J_{SC}^m} \tag{3.6.2}$$

where $J^{n/m}$ denotes to different light intensities. In order to determine the collection efficiency, a Mathematica program written by Obereigner et al. was used [74].

3.6.2. Measurement of the V_{OC}-transient $(V_{OC}(t))$

Under red-light illumination the doping density of CIGSe absorber increases [4]. Depending on the dominant recombination path, this leads to different behavior of the open-circuit voltage of solar cells (see chapter 6). Hence, by monitoring the evolution of $V_{OC}(t)$ under red-light illumination, the dominant recombination path can be determined [14, 38, 75, 76]. Prior to measuring $V_{OC}(t)$, the samples were relaxed for 16 hours at 318 K in the dark and subsequently cooled down to 298 K. The measurement of $V_{OC}(t)$ was started simultaneously with illumination of the sample by opening a light shutter and continued for several hours. For red-light illumination, a xenon lamp solar simulator (AM 1.5, 1000 W/m^2) with an optical cut-off filter ($\lambda > 630$ nm) was used. The initial temperature deviation, which is connected to the heat flow from the lamp, was corrected using measured changes of V_{OC} at different temperatures [14].

3.6.3. Measurement of the doping transient $(N_{A,a}(t))$

The procedure of time-dependent measurement of the doping density $(N_{A,a}(t))$ follows the one introduced by Obereigner et al. [14]. Initially the samples were transitioned into the relaxed state by keeping them in the dark at 310 K for 16 hours. Subsequently, they were cooled down to 100 – 120 K in order to determine the doping density $(N_{A,a}(t_0))$. This was done by extracting the capacitance of the space-charge region from a frequency-dependent measurement of the sample capacitance and calculating the doping density after equations 2.1.5 and 2.1.1 [14]. In the next step, the samples were heated to 298 K, exposed to red light for a certain time and cooled down once more in order to determine the doping density again $(N_{A,a}(t))$. The measurement routine is illustrated in Fig. 3.4.
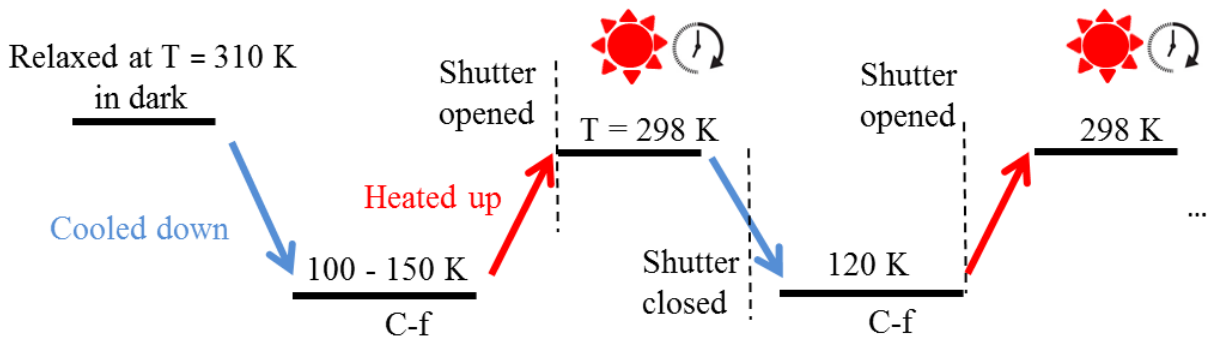
Figure 3.4.: Schematic measurement routine of C(f)-spectra to determine the doping density transients $(N_{A,a}(t))$. The image is adapted from the reference [14].

3.7. Simulation method

The simulations were performed with the help of Synopsys® TCAD, a multidimensional device simulator, in order to study the electronic transport in wide-gap CIGSe cells.
At the beginning of each simulation routine, the geometry of the cell under investigation has to be defined. Using Delaunay triangulation, the sample is decomposed into triangles or tetrahedra, thereby generating a mathematical mesh. Here, the mesh generation can be controlled with regard to number or maximum distance of the mesh points. Each vertex contains information on the material properties at the respective site. In the second step of the simulation routine, the discretized Poisson and the continuity equations for electrons and holes are solved self-consistently accounting for the applied boundary conditions. It is emphasized, that Senaturus TCAD (in contrast to plenty of other simulation tools) uses the Fermi-Dirac distribution rather than the Boltzmann approximation, which allows for accurate results even at low temperatures [77].

4. Band gap engineering of wide bandgap CIGSe

Increasing the bandgap is a tempting approach in order to get closer to the Shockley–Queisser limit [3]. However, in the case of CIGSe cells, the increase of the gallium content is accompanied by a strong voltage dependency of the carrier collection [7, 78]. A voltage dependent carrier collection ($\eta_C(V)$) influences the FF and the J_{SC} [7, 79]. This dependency can be partially suppressed if a gallium gradient is implemented in the absorber [7]. Shafarman et al. have observed that the films with gallium grading have a higher current collection and thereby an improved FF [7]. The benefit of the gradient on the electronic properties of low-gallium content CIGSe solar cells has been studied intensively (see e.g. [80–82]). Besides the beneficial effect of the gradients, both experiments [83] and simulations [20, 84] indicate that an excessive front gradient affects adversly the carrier collection and reduces the FF, and also blocks the current [83–85]. It has been suggested that one of the reasons of the low performance of the high-gallium content CIGSe materials is low fillfactor values. Therefore, the question that arises is if there is any room for the wide-gap CIGSe cells to adjust the gradient and improve the FF and J_{SC}. In the following chapter the influence of strong composition grading on the electronic transport will be studied. The improvement of the FF of wide-gap CIGSe solar cells by adjusting the bandgap grading of the absorber is going to be discussed.

4.1. Influence of the compositional gradient on the electronic properties of Cu(In$_x$,Ga$_{1-x}$)Se$_2$ solar cells

The influence of gallium concentration on the depth profile of CIGSe absorber is shown in figure 4.1(a). The absorbers were grown on a soda-lime glass by the typical multi-stage process (section 3.3.2-recipe (a)). In order to prepare the CIGSe absorbers with different gallium concentrations, the duration of each stage was kept constant and only the evaporation rate of gallium and indium was changed in the first and third stage. As a result, the time for inter-diffusion of materials in the second stage was approximately the same for all three processes.
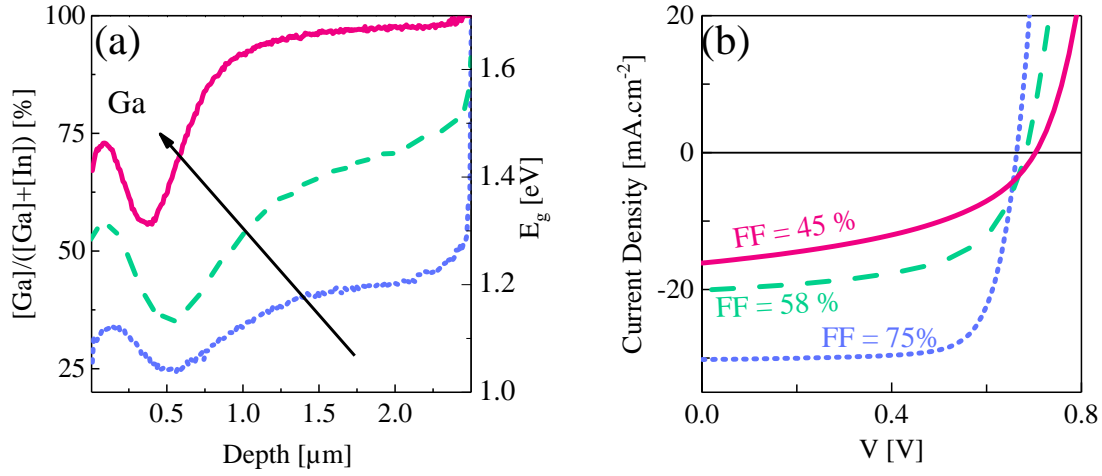
Figure 4.1.: Influence of the increased gallium concentration on the (a) gradient profile according to deposition recipe (a), (b) JV-curves of the corresponding GGI profiles. As the gallium concentration increases, the gradient profile of the CIGSe absorber gets more pronounced and FF reduces.

Simultaneously with the increase of the gallium concentration, the back gradient height as well as the front gradient height increases and results in a pronounced gradient profile (Fig.4.1(a)). Thus the increase of gallium concentration does not only shift the bandgap to higher values but also modifies the gradient profile (Fig.4.1(a)). The JV-curves of the corresponding GGI profiles are shown in figure 4.1(b). As the gallium concentration increases, V_{OC} increases and simultaneously J_{SC} reduces, but FF reduces to 45% for GGI of 0.80. The low FF of the wide-gap CIGSe absorbers is a known phenomenon and is one of the problems limiting the efficiency of wide-gap CIGSe [78]. But is the low FF arising from the pronounced gradient profile?

In order to address this issue, the deposition procedure of the absorber with the GGI of 0.8 was modified to smoothen the gradient profile. Therefore, the modified deposition recipe explained in section 3.3.2 (recipe(b)) was used. The resulting GGI depth profile of the absorber with the modified recipe and the multi-stage process is shown in figure 4.2(a). The modified deposition recipe has reduced the back barrier height of the sample and has removed the strong front gradient. As a result the notch is less deep compared to the reference sample.

The JV-curves of solar cells prepared by the multi-stage and modified recipe is shown in figure 4.2(b). As it can be seen, J_{SC} is enhanced for the sample with the modified deposition recipe (Figures 4.2(b) and 4.3(a)). The EQE signal of the sample deposited by the multi-stage process shows a very weak carrier collection in the long wavelength region (600 - 900 nm) (Fig. 4.3(a)), possibly due to an incomplete absorption originating from the strong gallium gradient. In contrast, the EQE signal of the modified recipe sample is substantially improved not only at long wavelength regions but also the whole spectrum
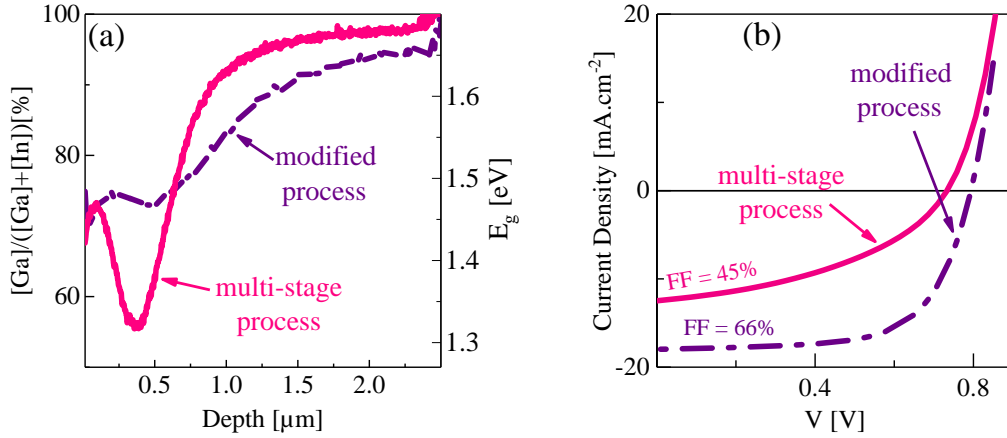
Figure 4.2.: Influence of different deposition recipes on the (a) gallium gradient (GGI depth profile), (b) corresponding JV-curves of the reference and modified-recipe sample with an integral GGI value ~ 0.8.

is higher than for the multi-stage process. The influence of the gallium gradient on the current density will be examined in more detail in section 4.2.

Besides the improved V_{OC} and J_{SC}, the JV curve of the modified recipe shows a more rectangular shape (Fig. 4.2(b)). By computing the collection efficiency ($\eta(V)$) from different light intensities of JV curves [73, 74], it can be observed that the collection efficiency of the modified recipe is improved (Fig. 4.3(b)), which is reflected in the FF [79]. The influence of the collection efficiency ($\eta(V)$) on the FF will be derived and discussed in section 4.3.
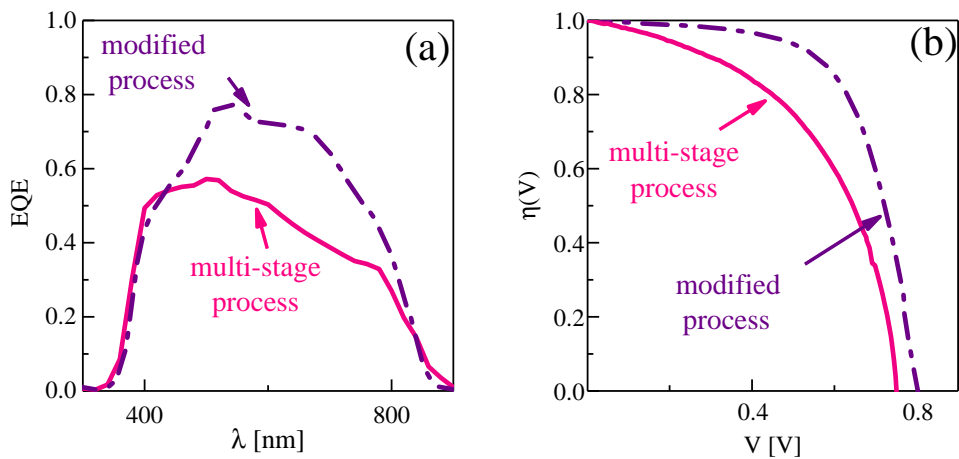
Figure 4.3.: Influence of the different gallium gradients of the reference and modified-recipe sample on the (a) EQE signal, (b) collection efficiency ($\eta(V)$) of the corresponding samples.

Figures 4.2 and 4.3 show that an excessive front grading deteriorates the FF and J_{SC}. This is also consistent with previous findings on small bandgap CIGSe cells [83, 86], and

indicates that indeed the compositional gradient is an important issue in wide bandgap CIGSe solar cells. Therefore, considerable attention must be paid to the deposition recipe of the wide-gap CIGSe absorbers.

So far, it has been shown that a pronounced gallium gradient deteriorates the electronic properties of wide gap CIGSe cells and the deposition recipe of the wide band gap CIGSe absorbers requires some modification. In the next section, the influence of a gallium gradient on the J_{SC} will be investigated by calculating the collection function (section 4.2). Then, in section 4.3 a relation between the collection efficiency and FF will be derived.

4.2. Influence of the gallium-gradient on the collection function $\left(\eta_{\mathsf{C}}(z)\right)$

In this section, the collection probability $(\eta_{\mathrm{C}}(z))$ for the GGI depth profiles of figure 4.2 is calculated. The gallium gradient induces an effective field that influences the carrier collection [18].

The influence of the gradient can be studied from the viewpoint of the reciprocity theorem [87] and, as shown in equation 2.2.6, is being reflected as the derivative of the electron affinity $(d\chi(z)/dz)$. In order to calculate the electron affinity, the gallium gradient was recalculated to the bandgap values according to equation 2.6.1, considering $b = 0.3$ eV. Further, it was assumed that the diffusion length is small and the carriers within the space charge region cannot be collected completely. This means the collection function is not unity within the depletion region and the boundary condition (2.2.7) is not valid. Therefore the electrostatic field is also considered in the calculation of the collection function $(\eta_{\mathrm{C}}(z))$ and equation 2.2.6 changes to (Eq 4.2.1):

$$\frac{d^2\eta_{\mathrm{C}}(z)}{dz^2} + \frac{1}{k_{\mathrm{B}}T}\left(\frac{d\chi(z)}{dz} - q^2\frac{N_{\mathrm{A,a}}}{\epsilon_{\mathrm{a}}}(w_{\mathrm{a}} - z)\right)\frac{d\,\eta_{\mathrm{C}}(z)}{dz} - \frac{n(z)}{L_{\mathrm{n}}^2} = 0 \qquad (4.2.1)$$

where w_{a} is the width of the space charge region and $N_{\mathrm{A,a}}$ is the doping density of the absorber. Solving the equation 4.2.1 numerically requires information on few parameters, which are given in Table 4.1. The resulting $\eta_{\mathrm{C}}(z)$ for both smooth and pronounced gradient is shown in figure 4.4(a). The collection function in CdS is assumed to be unity (similar to reference [4]) and falls off to zero after 0.1 μm in ZnO. The width of the space charge region is highlighted in figure 4.4(a) and is marked with $-w_{\mathrm{a}}$. The calculated collection function from the GGI profiles (Fig.4.2) shows that the sample with the pronounced gradient suffers from a low collection probability in the QNR (-2 μm < z < -0.3 μm) and SCR (-0.3 μm < z < 0) region, while the collection function of the sample from modified recipe sample is higher both in the SCR and in the QNR. As a result, the smooth gradient enhances the

Table 4.1.: parameters for computation of the collection function ($\eta_\mathrm{C}(z)$) in equation 4.2.1

simulation parameter	value
absorber doping ($N_\mathrm{A,a}$)	7×10^{15} cm^{-3}
width of space charge region (w_a)	0.3 μm
mobility of electrons (μ_n)	1 cm^2/(V s)
minority carrier lifetime (τ_n)	10^{-9} s
back surface recombination velocity (S_n0)	10^5 cm/s
buffer thickness (d_b)	0.05 μm
window thickness (d_n)	0.5 μm
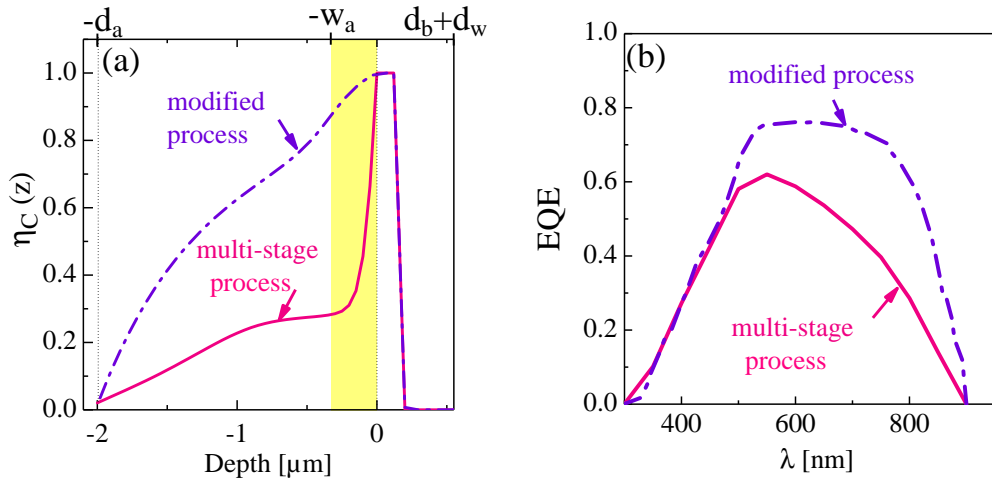
Figure 4.4.: Influence of the gallium gradient on (a) collection function ($\eta_\mathrm{C}(z)$), (b) calculated EQE for GGI profiles of figure 4.2. The width of the space charge region is highlighted and is marked with $-w_\mathrm{a}$.

carrier collection, while the pronounced gradient profile deteriorates the carrier collection. From the collection function in figure 4.4(a) the EQE can be calculated (Eq. 2.4.8). For this purpose the absorption coefficient for each layer must be known and the generation profile must be calculated. Optical absorption of the CIGS material with GGI = 0.78 is taken from experimental data reported by Orgassa [88]. Further, it was assumed that the optical absorption is constant through the absorber and any variation of the $E_\mathrm{g}(z)$ was omitted.

The calculated EQE's of both gradient profiles of figure 4.2 are shown in figure 4.4(b) and are very similar to the measured EQE's in figure 4.3(b). Both the measured and calculated EQE of the multi-stage process sample from recipe (a) show a weak signal at the long wavelength region. This is due to the low collection function at large depths and reflects the pronounced gradient. Thus, this gradient is the cause of the small of the short-circuit current density (J_SC) (Eq. 2.4.9). In contrast the calculated EQE for the modified recipe indicates the higher collection function is the reason for the larger J_SC of this sample. In the calculation of the collection function all the parameters were identical, except the

bandgap profile. Therefore, from a weak EQE signal of the multi-stage process can be understand that the pronounced gradient profile induces a barrier for the photo-current and reduces the current density.

4.3. Influence of the collection efficiency (η(V)) on the FF

In this section, the aim is to describe the FF as a function of the collection efficiency (η(V)). From the dependency of the V_{OC} to $\eta(V)$ a relation for the V_{mpp} is derived. From equation 2.4.4 and equation 2.4.3 the open-circuit voltage ($V_{\mathrm{OC}}(\eta(V_{\mathrm{OC}}))$) for a one-diode model can be written as:

$$
\begin{aligned}
V_{\mathrm{OC}}(\eta(V_{\mathrm{OC}})) &= \frac{Ak_{\mathrm{B}}T}{q} \, ln\left(\frac{J_{\mathrm{SC}}\,\eta(V_{\mathrm{OC}})}{J_0}\right) \\
&= V_{\mathrm{OC}}^0 + \frac{Ak_{\mathrm{B}}T}{q} \, ln\left(\eta(V_{\mathrm{OC}})\right).
\end{aligned}
\tag{4.3.1}
$$

where V_{OC}^0 is the open-circuit voltage if it is assumed that $\eta(V_{\mathrm{OC}}) = 1$ [79]. Note that $0 \leq \eta(V) <1$, therefore the ln-value is always a negative value. With improving the collection efficiency and getting closer to 1, the ln-value increases and has a smaller impact on the $V_{\mathrm{OC}}(\eta(V_{\mathrm{OC}}))$-losses.

In order to find a relation for the V_{mpp}, the power ($P(V) = VJ(V)$) is maximized with respect to the voltage (Eq. 2.4.5). In the next step, the $J_{\mathrm{mpp}}(V_{\mathrm{mpp}})$ of the one-diode model is inserted in equation 2.4.5. This gives:

$$
\begin{aligned}
J_0\Big(\frac{q}{Ak_{\mathrm{B}}T}\Big)exp\Big(\frac{qV_{\mathrm{mpp}}}{Ak_{\mathrm{B}}T}\Big) - J_{\mathrm{SC}}\frac{d}{dV}\eta(V)\Big|_{V_{\mathrm{mpp}}} &= \\
-\frac{1}{V_{\mathrm{mpp}}}\left(J_0\Big(exp\Big(\frac{qV_{\mathrm{mpp}}}{Ak_{\mathrm{B}}T}\Big) - 1\Big) - \eta(V_{\mathrm{mpp}})J_{\mathrm{SC}}\right).
\end{aligned}
\tag{4.3.2}
$$

This equation can be rearranged:

$$
\left(1 + \frac{qV_{\mathrm{mpp}}}{Ak_{\mathrm{B}}T}\right)exp\Big(\frac{qV_{\mathrm{mpp}}}{Ak_{\mathrm{B}}T}\Big) = 1 + \frac{J_{\mathrm{SC}}}{J_0}\left(\eta(V_{\mathrm{mpp}}) + V_{\mathrm{mpp}}\frac{d}{dV}\eta(V)\Big|_{V_{\mathrm{mpp}}}\right)
\tag{4.3.3}
$$

On the right hand-side of the equation 4.3.3, the relation between J_{SC} and J_0 can be substituted from equation 4.3.1. As a result the dependency of equation 4.3.3 on current density is removed and $V_{\mathrm{OC}}(\eta)$ is inserted. The collection function of $\eta(V_{\mathrm{OC}})$ in equation 4.3.1 can be expanded around $\eta(V_{\mathrm{mpp}})$. This results in $\eta(V_{\mathrm{OC}}) = \eta(V_{\mathrm{mpp}}) + (V_{\mathrm{OC}}\text{-}V_{\mathrm{mpp}})\frac{d}{dV}\eta(V_{\mathrm{mpp}})$. For the sake of simplicity, it is assumed that $\eta(V_{\mathrm{OC}}) \approx \eta(V_{\mathrm{mpp}})$. The substitution of J_{SC}/J_0 from equation 4.3.1 into equation 4.3.3 leads to:

$$\left(1 + \frac{qV_{\text{mpp}}}{Ak_{\text{B}}T}\right) exp\left(\frac{qV_{\text{mpp}}}{Ak_{\text{B}}T}\right) = exp\left(\frac{qV_{\text{OC}}(\eta)}{Ak_{\text{B}}T}\right) \qquad (4.3.4)$$

The derived relation is similar to the relation derived by De Vos [26], however, now the V_{OC} and V_{mpp} are also dependent on $\eta(V)$. In the next step, for convenience the term $\upsilon_{\text{mpp}} = \frac{qV_{\text{mpp}}}{Ak_{\text{B}}T}$ and $\upsilon_{\text{OC}} = \frac{qV_{\text{OC}}(\eta)}{Ak_{\text{B}}T}$ is introduced in equation 4.3.4 [26]. Taking logarithm from both sides of equation 4.3.4 yields to:

$$\upsilon_{\text{mpp}} + ln\left(1 + \upsilon_{\text{mpp}}\right) = \upsilon_{\text{OC}} \qquad (4.3.5)$$

For large υ_{OC}, the equation can be approximated as follows [26]:

$$\frac{\upsilon_{\text{mpp}}}{\upsilon_{\text{OC}}} = 1 - \frac{1}{\upsilon_{\text{OC}}}ln(\upsilon_{\text{OC}}) + \frac{1}{\upsilon_{\text{OC}}^2}ln(\upsilon_{\text{OC}} - 1) + ... \qquad (4.3.6)$$

This derivation suggests that the ratio of $\upsilon_{\text{mpp}}/\upsilon_{\text{OC}}$ has no dependency to $\eta(V_{\text{OC}})$, however extreme caution must be paid, since the υ_{OC} is logarithmically dependent on $\eta(V_{\text{OC}})$ (equation 4.3.1).

So far, a relation between υ_{mpp} and υ_{OC} was derived. In the next step the ratio of $J_{\text{mpp}}/J_{\text{SC}}$ will be calculated. For the one-diode model this ratio is defined as:

$$\frac{J_{\text{mpp}}}{J_{\text{SC}}} = \frac{J_0}{J_{\text{SC}}}\left(exp\left(\frac{qV_{\text{mpp}}}{Ak_{\text{B}}T}\right) - 1\right) - \eta(V_{\text{mpp}}) \qquad (4.3.7)$$

By inserting the ratio of J_0/J_{SC} from equation 4.3.1, equation 4.3.7 becomes:

$$\frac{J_{\text{mpp}}}{J_{\text{SC}}} = \eta(V_{\text{OC}})\frac{exp(\upsilon_{\text{mpp}}) - 1}{exp(\upsilon_{\text{OC}}) - 1} - \eta(V_{\text{mpp}}). \qquad (4.3.8)$$

Substitution of equation 4.3.5 into equation 4.3.8 and considering that $\eta(V_{\text{mpp}}) \approx \eta(V_{\text{OC}})$ gives:

$$\frac{J_{\text{mpp}}}{J_{\text{SC}}} = -\eta(\upsilon_{\text{OC}})\left(\frac{\upsilon_{\text{mpp}}}{\upsilon_{\text{mpp}} + 1}\right)\frac{exp(\upsilon_{\text{OC}})}{exp(\upsilon_{\text{OC}}) - 1} \qquad (4.3.9)$$

The appearance of a minus sign in equation 4.3.9 is due to the convention of taking the current flow to the right as a positive current. Thus, from equation 4.3.9, it can be perceived that $J_{\text{mpp}}/J_{\text{SC}}$ rises with $\eta(V)$. For large υ_{OC} the last-term in equation 4.3.9 approaches to unity and simplifies the equation 4.3.9. Furthermore υ_{mpp} can be substituted with the equation 4.3.6. By multiplying $J_{\text{mpp}}/J_{\text{SC}}$ (Eq. 4.3.9) with $\upsilon_{\text{mpp}}/\upsilon_{\text{OC}}$ (Eq. 4.3.6), the fill factor for a one-diode model is obtained:

$$FF\left[\eta(V_{\text{OC}}), \upsilon_{\text{OC}}\right] = -\eta(V_{\text{OC}})\frac{(\upsilon_{\text{OC}} - ln(\upsilon_{\text{OC}}))}{(\upsilon_{\text{OC}} - ln(\upsilon_{\text{OC}}) + 1)}\frac{(\upsilon_{\text{OC}} - ln(\upsilon_{\text{OC}}))}{\upsilon_{\text{OC}}} \qquad (4.3.10)$$

The obtained relation for the fillfactor is solely dependent on υ_{OC} and $\eta(V_{OC})$. The relation 4.3.10 shows the linear dependency of the FF from the $\eta(V_{OC})$. The relation further indicates that with the increase of the υ_{OC}, the fillfactor increases. This can be accomplished either by the increase of V_{OC} or decrease of the diode quality factor. The second term in equation 4.3.10 can be approximated as follows:

$$
\begin{aligned}
\frac{\upsilon_{OC} - ln(\upsilon_{OC})}{\upsilon_{OC} - ln(\upsilon_{OC}) + 1} &= \frac{\upsilon_{OC} - ln(\upsilon_{OC})}{(\upsilon_{OC} - ln(\upsilon_{OC}))\left(1 + \frac{1}{\upsilon_{OC} - ln(\upsilon_{OC})}\right)} \\
&= \frac{\upsilon_{OC} - ln(\upsilon_{OC}) - 1}{\upsilon_{OC} - ln(\upsilon_{OC})}.
\end{aligned}
\tag{4.3.11}
$$

Then the fillfactor reduces to:

$$
FF\left[\eta(V_{OC}), V_{OC}(\eta)\right] = -\eta(V_{OC}) \frac{\left(\frac{qV_{OC}(\eta)}{Ak_BT}\right) - ln\left(\frac{qV_{OC}(\eta)}{Ak_BT}\right) - 1}{\left(\frac{qV_{OC}(\eta)}{Ak_BT}\right)}
\tag{4.3.12}
$$

It must be mentioned, that the attained fill factor in equation 4.3.12 is an approximate solution and shows a good accuracy for large V_{OC}-values ($V_{OC} > 0.73$ V), which is in the range of wide-gap CIGSe solar cells. In general, it is found that the FF increases linearly with increasing $\eta(V_{OC})$.

4.4. Concluding remarks

In the first section, it was shown that as the gallium concentration in the CIGSe absorber increases, the depth profile of the gallium gradient from the typically multi-stage process becomes more pronounced. The investigated pronounced gradient profile of the high gallium content CIGSe cells has a few drawbacks including:

- reduction of the collection probability ($\eta_C(z)$), which is reflected in the short circuit current density (J_{SC}),

- strong voltage dependency of the collection efficiency ($\eta(V)$), that is reflected in the V_{OC} and FF.

Such a pronounced gradient can be avoided by modifying the deposition process. By modification of the multi-stage deposition process all the electronic parameters are improved to a large extent. Therefore, adjusting the gradient profile of wide bandgap CIGSe solar cells is necessary to achieve high efficiency.

5. Doping with heavy alkaline elements: K, Rb, and Cs

The main reason holding the efficiency of wide-gap CIGSe solar cells back is the saturation of V_{OC} [2]. This is mainly due to a high interface recombination, originating from a unfavorable band alignment at the interface [8, 89]. The interface recombination rate can be partially quenched by lowering the valence band edge at the hetero-junction interface [4, 8]. In this way, a higher degree of inversion is achieved and the V_{OC} increases. Recently, it has been shown that the post-deposition treatment of alkalis (K, Rb, and Cs) on small bandgap CIGSe absorbers induces a new phase near the surface region that widens the CIGSe surface bandgap and increases the V_{OC} [10, 11, 37]. Therefore, it becomes important to examine if the post-deposition treatment of alkalis has the same effect on wide-gap CIGSe solar cells. In this chapter the following questions will be explored: Does the post-deposition treatment with alkali elements improve the solar cell properties of wide-gap CIGSe absorbers; How does the post-deposition treatment with alkali elements influence the electronic charge transport in wide-gap CIGSe cells. To answer the last question, temperature dependent current-voltage curves on alkali treated and untreated wide-gap CIGSe cells are recorded and numerical simulations with Sentaurus® TCAD are conducted to explain the observed phenomena of the $JV(T)$ curves.

5.1. Introduction of heavy alkaline elements

5.1.1. Experimental section

The influence of heavy alkali post deposition treatment was examined on CIGSe samples with different GGI in the range of 0.3 - 0.85. The small bandgap CIGSe absorbers ($E_g <$ 1.3 eV), were grown according to the multi-stage process (chapter 3). But the high gallium-content absorbers ($E_g >$ 1.3 eV) were deposited according to the modified recipe introduced in chapter 3. In this way the formation of a pronounced gallium gradient of wide bandgap CIGSe absorbers could be avoided (chapter 4). The grown CIGSe absorbers were treated with KF, RbF, and CsF with an evaporation rate of 0.1 Å/s for 600 s, 1925 s, and 800 s, respectively. Afterwards the absorbers were finished to solar cells as described in chapter 3.
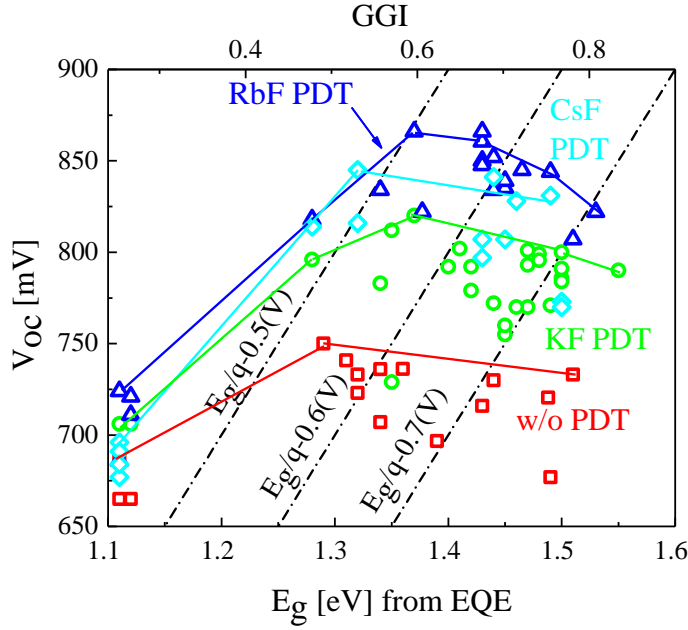
Figure 5.1.: Measured V_{OC} for alkali-treated and untreated CIGSe devices versus the bandgap value (E_g). The values of E_g were determined from the leading edge of the EQE. Dashed-dotted lines indicate different values of ΔV_{OC}. The CGI of these samples varies between 0.83 - 0.93. Reproduced with permission from [90].

5.1.2. Influence of alkali-PDT on the electronic properties

The measured V_{OC} versus the extracted bandgap (E_g) for treated and untreated samples is plotted in Fig. 5.1. The V_{OC} increases with an alkali-treatment and the highest gain is observed in V_{OC} is for cells with $E_g \sim 1.35$ eV. RbF-PDT proves to be the most effective treatment for increasing V_{OC}. However, in some cases the V_{OC} of CsF-treated samples is as high as that of RbF-treated samples. Despite the gain in V_{OC}, the V_{OC}-deficit increases as the bandgap increases. The increasing V_{OC}-deficit in wide-gap cells can originate from an increased deep defect density [91, 92] or from an interface band offset promoting interface recombination [6, 8]. The increased V_{OC} for the RbF and CsF-treated samples are in line with our inital report on KF-treated CIGSe samples [93]. In this case, however, the absorbers were grown in one-stage instead of the multi-stage process [93]. Furthermore, it was found that KF-PDT increases the V_{OC} of wide-gap CIGSe absorber devices and the V_{OC}-deficit increases as the gallium concentration increases [93].
A number of studies have shown that alkali-PDT on low-gap CIGSe absorbers suppresses the recombination at the interface and improves the V_{OC} [12, 37, 39]. Besides the beneficial effect of alkali-PDT on the solar cell parameters, Lepetit et al. report on the detrimental side of the KF-PDT [94]. They claim that potassium must be deposited in a Cu-poor phase of CIGSe absorber deposition, otherwise all the electronic parameters will reduce [46, 94]. In figure 5.1, there is one KF-treated sample which shows a lower V_{OC}-value than the untreated sample. The final CGI of this sample is 0.9 and the sample is Cu-poor. Therefore, the low V_{OC} of this sample cannot necessarily be explained by the copper
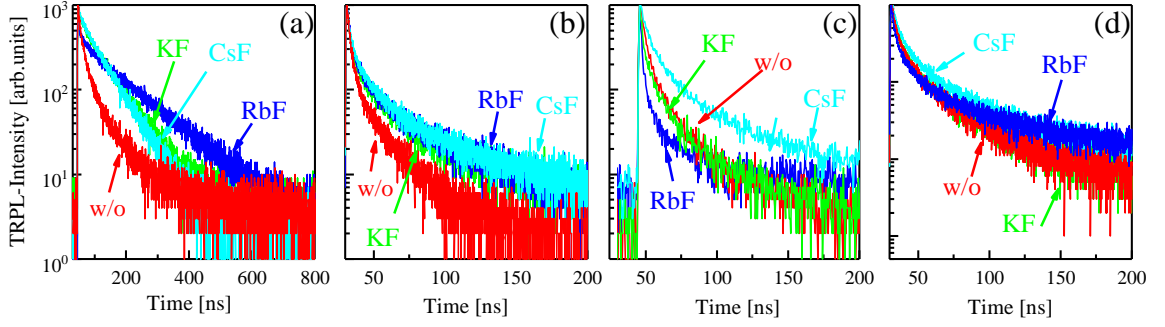
Figure 5.2.: TRPL transients of alkali-treated and untreated absorber layers for different bandgap value (a) E_g = 1.12 eV, (b) E_g = 1.34 eV, (c) E_g = 1.44 eV, and (d) E_g = 1.52 eV. Due to the shorter decay times of high gallium-content absorbers compared to low Ga-content absorbers, the time-axis of figures (b - d) are illustrated in a smaller range.

concentration. For RbF- and CsF-treated sample, such an effect was not observed.

While the influence of heavy alkalis on CIGSe devices with GGI = 0.3 is widely examined [11, 38, 95, 96], studies relating the influence of alkali-PDT on wide-gap CIGSe absorbers are very limited [6, 38]. For instance, Jackson et al. have shown that the saturation of V_{OC} for CIGSe cells with a bandgap value smaller than 1.30 eV can be partially suppressed by potassium treatment [39]. Ishizuka et al. have shown that the RbF-PDT does not increase the V_{OC} of CuGaSe$_2$ devices [6].

But what is the origin of the increased V_{OC} via alkali-PDT? One of the parameters which correlates with V_{OC} is the minority carrier lifetime (τ_n) [44, 97]. The time resolved photo-luminescence (TRPL) signals of treated and untreated samples with different bandgap values (E_g = 1.12, 1.34, 1.44 and 1.52 eV) are illustrated in figure 5.2. In order to allow meaningful interpretation of the TRPL decays, measurements were conducted on bare absorbers and the intensity of the laser was low, to be in the low injection regime [97, 98]. Due to the short decay times of wide-gap absorbers compared to small bandgap absorbers, the time-axis of figures 5.2(b - d) are depicted in a smaller range.

For samples with the bandgap value of 1.12 eV (GGI = 0.3) in figure 5.2(a), the post-deposition treatment with heavy alkali elements has lead to longer TRPL decay times. The TRPL curve of the untreated sample and RbF-PDT can be described by a bi-exponential function with a fast and slow decay-time component. The fast lifetime, is interpreted as an interface lifetime and the slow lifetime is correlated to the bulk lifetime that reflects the V_{OC} [99]. The TRPL curves of KF and CsF-treated absorbers, show a mono-exponential decay, which hints to a reduced recombination in the interface. Thus the figure 5.2(a) might suggest an increase of the lifetime of the minority carriers of the alkali treated samples. Reports on TRPL measurements on CIGSe absorbers with the bandgap value of 1.12 eV indicate that the post-deposition treatment of alkalis enhances the decay times and with heavier alkalis the decay curves gets longer [36]. It has to be noted that the interpretation of the TRPL decay curves is not straightforward, and it might be that the

longer decay curves are an indication of shallow defects [100].

In figure 5.2(b) the TRPL decay curves of samples with the bandgap value of 1.34 eV are presented. At this bandgap value, the maximum gain of V_{OC} for RbF-treated sample was achieved (Fig. 5.1). In comparison to samples with $E_g = 1.12$ eV, the curves show a faster decay time, which hints to a higher non-radiative recombination rate. But still it can be observed that the TRPL decay curves of the alkali-treated samples have a longer decay times than the untreated sample. To the best of our knowledge, no reports on the influence of alkali-treatment on TRPL on CIGSe with this bandgap value have been published yet. The TRPL-transients of CIGSe samples with $E_g = 1.44$ eV are depicted in figure 5.2(c). The KF-treated and untreated absorbers show the same TRPL-transients, but as can be seen in figure 5.1, the V_{OC} of the KF-treated sample shows an increase of at least 60 mV relative to the untreated sample. For RbF-treated sample can be seen the same. The V_{OC} of the RbF-treated is increased by about 120 mV compared to the untreated sample, but the TRPL decay curve shows a very fast initial decay and a slightly longer second decay-time compared to the untreated sample. The CsF-treated samples shows the longest decay time compared to other absorbers, but the open-circuit voltage of the RbF and CsF-treated cells are comparable as can be seen in figure 5.4. Hence, the TRPL-transients cannot explain the increase of V_{OC} of wide-gap CIGSe cells.

The TRPL-transients of the alkali-treated and untreated samples with the $E_g = 1.52$ eV (GGI = 0.83) show similar decay curves, but for instance the V_{OC} of the RbF-treated cell is about 100 mV higher than the untreated cell (Fig. 5.1), or the V_{OC} of the KF-treated is about 80 mV higher than the untreated sample. Therefore, the TRPL fails to explain the increased V_{OC} of the wide-gap CIGSe cells. In our initial report on KF-treated samples which was conducted in one-stage process, it was also mentioned that despite the increase of the V_{OC} the minority carrier lifetime of the untreated and KF-treated CIGSe absorbers are very similar [93]. Ishizuka has shown that the TRPL signal of the CuGaSe$_2$ sample does not change by alkali post-deposition treatment [6]. Therefore, the TRPL results of figure 5.2(c) confirm our earlier findings [93] and are well in agreement with [6].

The increased V_{OC} can also stem from the increased doping density provided that the cells are limited by SCR or QNR recombination [4]. For low-gap CIGSe cells with a dominant recombination in the bulk of the absorber, an increase of the doping density can explain the increase of the V_{OC}. It has been observed that the doping density of the KF-treated CIGSe samples increases one order by magnitude [41, 42, 46, 101], which corresponds to an increase of V_{OC} of about 60 mV. RbF-PDT has also shown to be an effective alkali to increase the doping density for small bandgap CIGSe cells [96, 102]. But for wide bandgap CIGSe solar cells whose dominant recombination path is at the interface [8, 89], the increase of the doping density cannot improve the V_{OC} of the solar cell. The reason is that the increase of the doping density reduces the inversion and thereby the V_{OC} [4]. Hence, another factor must be the origin of the increased V_{OC} of the alkali-treated wide
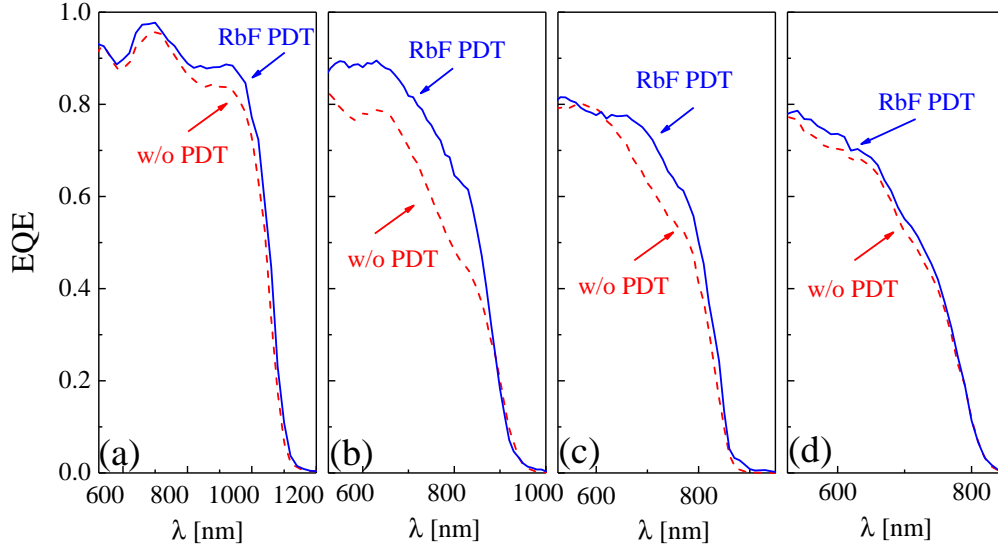
Figure 5.3.: EQE signal of RbF-treated and untreated samples for different bandgap values (a) $E_g = 1.12$ eV, (b) $E_g = 1.34$ eV, (c) $E_g = 1.44$ eV, and (d) $E_g = 1.52$ eV.

gap cells. This will be addressed in section 5.2.

The alkali-PDT on CIGSe absorbers not only had an impact on the V_{OC}, but also on the J_{SC}. In figure 5.3, the EQE signals of RbF-treated and untreated samples for CIGSe cells with different bandgap values are illustrated. Due to the similar EQE results of KF- and CsF-treated samples to RbF-PDT, the EQE results are presented in figure E.3. In order to compare the EQE signals accurately and eliminate any process variations, the untreated and RbF-treated samples were processed in the same CdS-bath and coated with i-ZnO and ZnO:Al in the same deposition run.

The EQE signals of RbF-treated samples with bandgap values of 1.12, 1.34, and 1.44 eV show an increase at long wavelengths. However, the relative increase is dependent on the GGI concentration. For instance, the highest gain in J_{SC} is observed for the bandgap value of 1.34 eV (Fig. 5.3(c)), where the smallest V_{OC}-deficit is achieved (Fig. 5.1), and the sample with the bandgap value of 1.52 eV shows no substantial increase in the EQE signal. Interestingly, for the samples with the $E_g = 1.34$ eV, the EQE signal of RbF-treated sample is not just increased at long wavelengths, but the overall spectra is higher than the untreated case (Fig. 5.3(b)), which hints of a reduced recombination rate at the interface. Most researchers have reported that the J_{SC} upon alkali-treatment increases [36, 37, 46, 103]. However the findings of the references [36, 37] need to be interpreted with caution, since they have also reduced the thickness of the buffer layer. For Ga-rich samples, Ishizuka et al. has shown that RbF-PDT increases the EQE signal at long wavelengths [6], which correlates fairly well with the findings in fig 5.3.

The increased spectral response at long wavelengths is an indication of an improved diffusion length (L_n) which is related to the minority carrier lifetime (τ_n) and the mobility
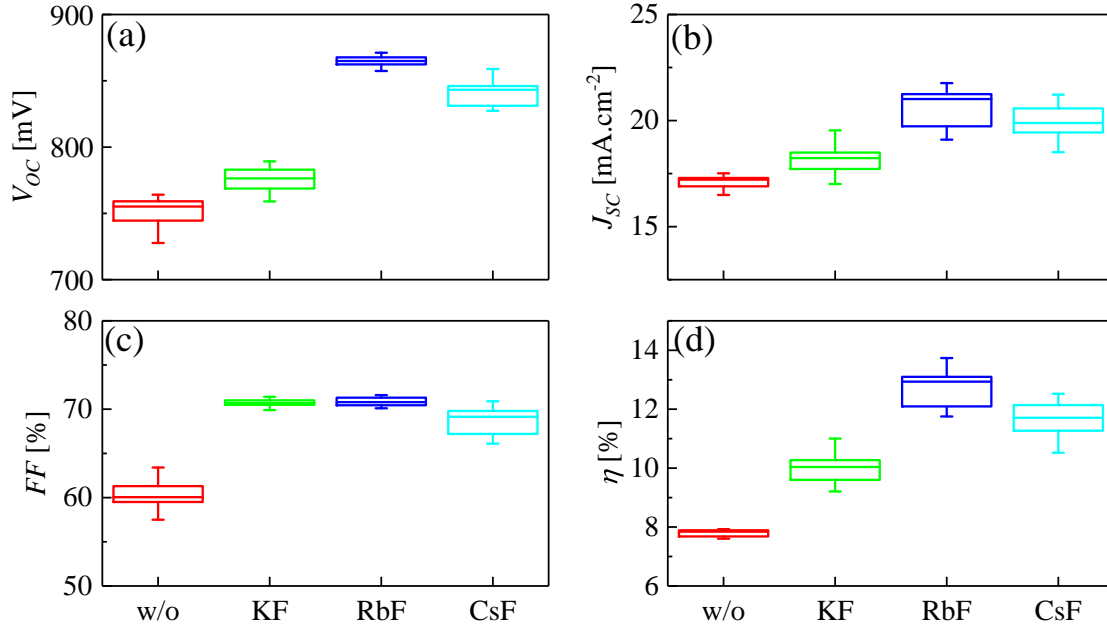
Figure 5.4.: The solar cell parameters of samples with the bandgap of 1.44 eV (a) V_{OC}, (b) J_{SC}, (c) FF, and (d) η. The samples have the final CGI of 0.85 - 0.88.

of the electrons (μ_n). In figure 5.2, the alkali-treated absorbers with the bandgap value of 1.12 eV, 1.34 eV show a longer decay curve but fails to explain the increase of EQE signal of the sample with $E_g = 1.44$ eV.

The solar cell parameters of a series with the bandgap value 1.44 eV and different alkali-PDT (KF, RbF, and CsF) is shown in figure 5.4. The absorbers were deposited according to modified recipe (see section 3.3.2) and then treated with heavy alkalis (section 5.1.1). The samples have the final CGI of 0.85 - 0.88. It can be observed that simultaneously with the improved V_{OC} and J_{SC} of alkali-treated cells, the FF and η (Fig. 5.4) have increased. RbF-PDT proves again to be the best alkali for increasing the efficiency.

In the next section (section 5.2), the electronic charge transport of CIGSe cells with a bandgap value of 1.44 eV is analyzed. For this purpose temperature dependent current-voltage curves are measured and numerical simulations are performed.

5.2. Temperature dependent current-voltage analysis

Dark and white light illuminated JV-curves of alkali treated and untreated CIGSe cells measured between 100 K and 300 K are shown in figure 5.5 (a - d). All the samples have the same bandgap value ($E_g = 1.44$ eV), and the lower open-circuit voltage of the untreated sample in figure 5.5(a) is due the absence of the alkali treatment (Fig. 5.1).

All samples in figure 5.5 show a crossover between the dark and light JV curves, i.e. at forward bias the current under illumination is higher than in darkness. This anomaly hints
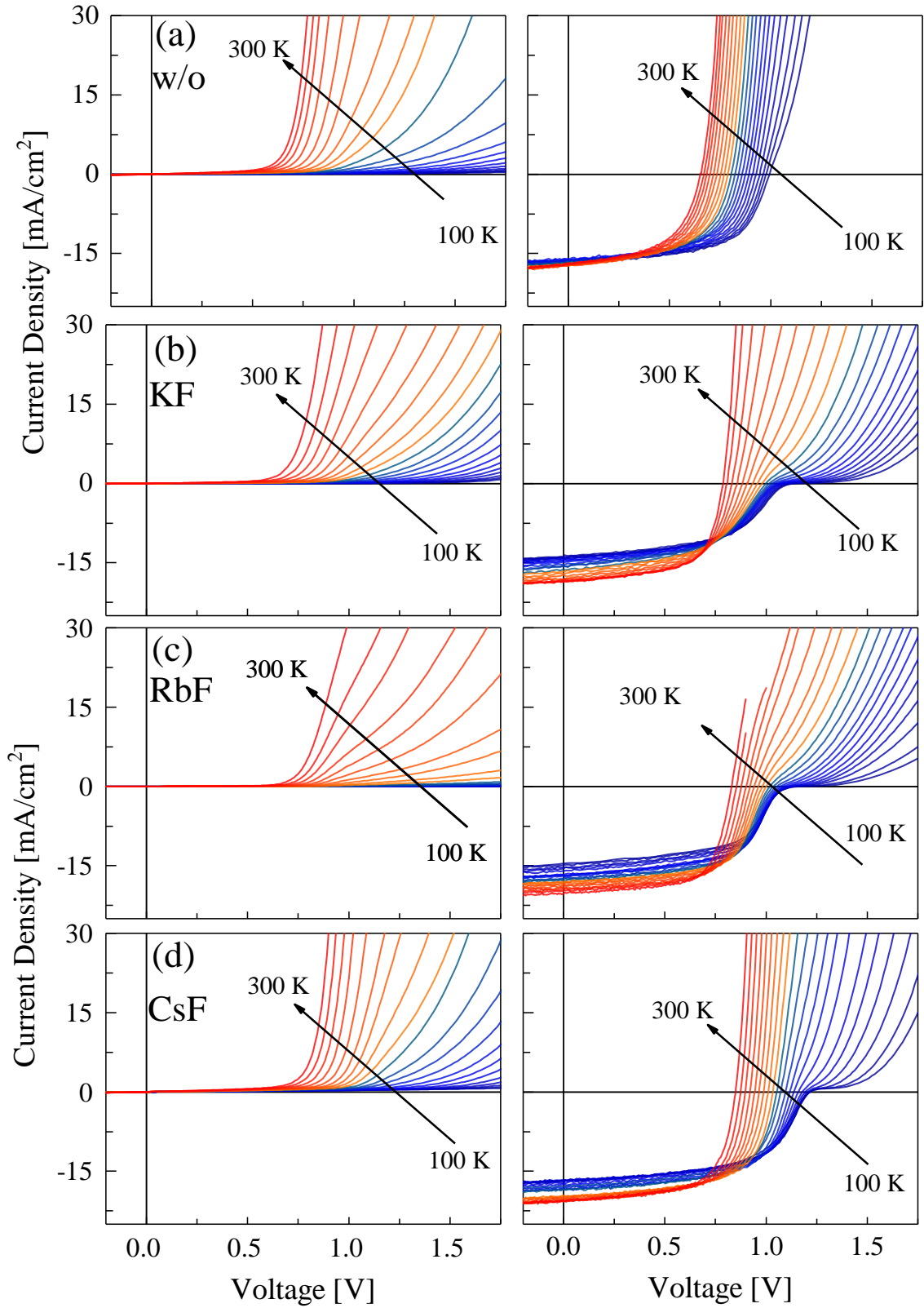
Figure 5.5.: Temperature dependent JV-curves (100 K to 300 K in 10 K steps) of samples (a) without alkali treatment, (b) KF-PDT, (c) RbF-PDT, and (d) CsF-PDT. All CIGSe layers have a bandgap value of 1.44 eV. Measurement in darkness (left column) and under white light of 100 mW/cm^2 (right column). The thickness of KF, RbF and CsF are 6 nm, 25 nm, and 8 nm, respectively.

to a barrier for the diode current and has been reported frequently for small bandgap CIGSe solar cells [104–106]. In addition, the alkali-treated samples reveal the double-diode behavior of the $JV(T)$ curves under white-light illumination, while the untreated CIGSe sample does not show a blocking behavior at low temperatures (Fig. 5.5(a)).

Studies performed on alkali-treated small band gap CIGSe cells, have never reported a double-diode behaviour so far [101, 107]. For small bandgap CIGSe cells with NaF and KF-PDT a rollover for the illuminated JV curves at low temperatures was observed which was explained by a barrier at the Mo/CIGSe interface [101]. For RbF-treated samples also a rollover was observed but the authors come to the conclusion that RbF induces a barrier at the front contact [107]. In the case of a barrier at the back contact both the dark and the illuminated $JV(T)$ curves have to show current saturation at large forward bias [4], which is not observed in figure 5.5(b - d). Therefore, it can be concluded that the double-diode behavior in figure 5.5 is due to a barrier at the front and not at the back contact.

Another important finding is that the short-circuit current density of the alkali-treated samples becomes temperature dependent (Fig. 5.5(b - d)). The short-circuit current density of the alkali-treated samples reduces as the temperature decreases (Fig. 5.5 (b - d)), while the short-circuit current density of the untreated sample is not influenced by temperature (Fig. 5.5 (a)).

The V_{OC}(a - d) data from figure 5.5 are plotted in figure 5.6 as a function of temperature. The extrapolation of V_{OC} measured at high temperatures (T > 200 K) towards T = 0 K roughly gives the activation energy of the saturation current density, E_A. The measurement result in figure 5.6 indicates that E_A of the untreated cell (w/o PDT) is smaller than the bandgap of $E_g = 1.44$ eV. The alkali treated samples, to the contrary, exhibit E_A approximately equaling the bandgap ($E_A \approx E_g + 3k_B T$). This indicates that the untreated device is limited by interface recombination [4, 15] and that the alkali treatment modifies the surface of the absorber. It has to be noted that a bandgap widening does not necessarily mean that the recombination path is changed into the bulk recombination. The recombination path of the alkali-treated samples will be investigated in chapter 6.

Another important finding is that the V_{OC} of the alkali-treated samples saturates at low temperature. Ott et al. suggested that the extrapolation of V_{OC} at low temperatures determines the barrier height at the back contact [108]. Therefore, one might conclude from figure 5.6 that the post-deposition treatment of alkalis induces a barrier at the back contact (Mo/CIGSe). But for a barrier at the back contact the JV-curves have to show a rollover at low temperatures, which is not observed for the alkali-treated samples. Hence, a barrier at the back contact cannot be the origin of the V_{OC} saturation at low temperatures. In the following, the distinct features in the temperature dependent JV curves of the wide gap CIGSe solar cells of figure 5.5(a - d) are summarized in Table 5.1. The Table 5.1 indicates that the alkali-treated samples regardless of the alkali (KF, RbF and CsF) show
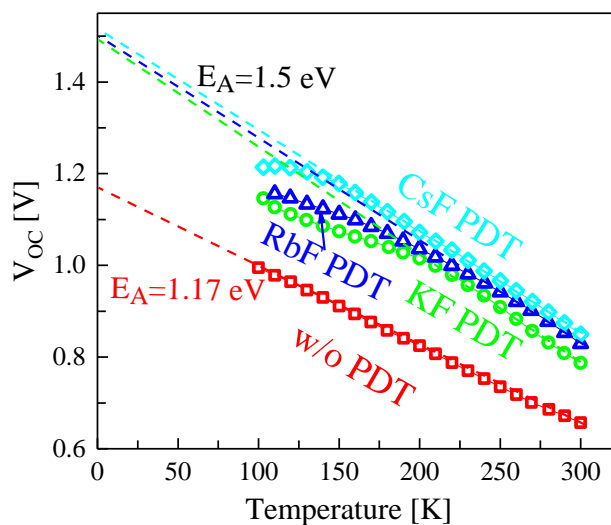
Figure 5.6.: Open-circuit voltages versus temperature from figure 5.5.

the same anomalies, while the untreated sample just exhibits a crossover.

Table 5.1.: Summary of the observed phenomena from the $JV(T)$ curves of the treated and untreated samples.

phenomena	crossover	double-diode	$J_{SC}(T)$	V_{OC}-saturation
wo PDT	✓			
KF-PDT	✓	✓	✓	✓
RbF-PDT	✓	✓	✓	✓
CsF-PDT	✓	✓	✓	✓

In the following, first different models for the crossover will be introduced and the JV(T)-curves of the untreated sample will be simulated (section 5.3). Then, in section 5.4, the observed phenomena of alkali-treated samples will be simulated.

5.3. Simulation of the untreated sample

One of the typically associated failures of CIGSe solar cells is the crossover between the light and dark JV-curves [109]. Some theories have been put forth in literature to explain this effect [104, 109, 110], which will be discussed in the following:

5.3.1. Impurities in CdS

The widely accepted model for the crossover is proposed by Eisgruber et al. [110]. The model suggests a crossover arises from an electron barrier for the injection (forward) current whose height reduces upon illumination [4]. An electron barrier (Φ_b) in the CIGSe

solar cell typically is referred to a negative conduction band offset, ΔE_C at the CdS/i-ZnO interface and a potential drop in the buffer layer (Fig. 5.7) [4]. The conduction band offset (ΔE_C (CdS/i-ZnO)) is a constant parameter and does not change upon illumination. Therefore, the potential drop in the CdS is the sole quantity which can be illumination dependent. In order to bring out the crossover, deep acceptor states in the CdS with very different capture cross section for carriers is required [110]. The acceptor states have a large capture cross section for the holes and small capture cross section for electrons ($\sigma_n \ll \sigma_p$) [111]. In darkness, the acceptor states are occupied by electrons compensating the ionized donors. This high compensation and low net doping causes a large potential drop in the CdS layer. Upon illumination, the acceptor states in the CdS are filled by holes, become neutral, the compensation is reduced, and a higher net positive charge (by uncompensated donors) lead to a band bending in CdS. This reduces the electron barrier (Φ_b). The reduced barrier height increases the recombination rate and lowers the voltage [110]. In figure 5.7 the conduction band of a wide-gap CIGSe cell with high acceptor density in CdS at the temperature of 300 K is shown. It can be seen that the barrier height decreases upon illumination, which leads to the crossover of the dark and light JV-curves. Following the model proposed by Eisgruber et al. [110], a high density of deep acceptor

Figure 5.7: The influence of deep acceptor states in CdS on the conduction band of a wide bandgap CIGSe/CdS/i-ZnO/Al:ZnO structure in dark (solid line) and upon illumination (dash-dotted line) at T = 300 K. Under illumination the acceptor states are ionized and shift the CdS conduction band downward. Hence, the electron barrier (Φ_b) upon illumination reduces compared to the dark case.
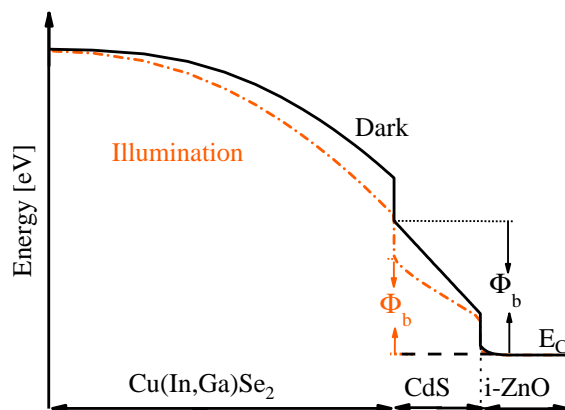
states in the CdS was introduced in the simulation. The doping density of the buffer layer was set 5×10^{18} cm^{-3} and the density of the acceptors was set 4.999×10^{18} cm^{-3}. As a result a net doping of 1×10^{15} cm^{-3} was used for the simulation of the buffer layer.

Concerning the band offset at the CdS/i-ZnO interface, Schmid et al have measured a band offset of ΔE_C (CdS/i-ZnO) = - 0.3 eV [112]. Researchers have always considered a negative value between [- 0.3, - 0.1] eV for the conduction band offset (ΔE_C) at CdS/i-ZnO layers [43, 107, 113, 114]. Therefore, the chosen band offset of ΔE_C (CdS/i-ZnO) $= -0.20$ eV for the simulation is in an agreeable range. It must be reminded that the ΔE_C (CdS/i-ZnO) has an impact on the crossover, a slight decrease of the ΔE_C (CdS/i-ZnO) leads to a pronounced crossover. But the ΔE_C(CdS/i-ZnO) is not a voltage dependent parameter, thus reducing the ΔE_C(CdS/i-ZnO) to values smaller than -0.3 eV blocks the forward
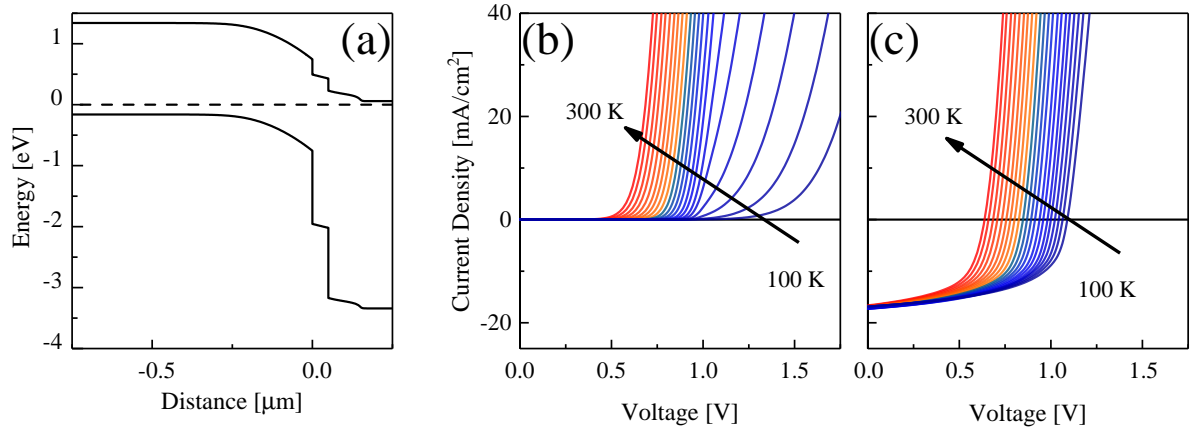
Figure 5.8.: Simulation results of deep acceptor states in CdS on wide bandgap CIGSe solar cells ($E_g = 1.5$ eV) (a) Band diagram in equilibrium at T = 300 K, (b) dark, and (c) illuminated $JV(T)$ evolution from T = 100 – 300 K in 10 K steps. The crossover between dark/illuminated JV is more pronounced at low temperatures (see Table A.1).

current completely and leads to a rollover in the simulated JV curves.

The bandgap of the absorber was chosen $E_g = 1.5$ eV. Due to the wide bandgap of the absorber, a negative conduction band offset between CIGSe and CdS was programmed (ΔE_C (CIGSe/CdS) = - 0.25 eV). For all layers in the simulation, a midgap defect similar to reference [4] was implemented.

The resulting band diagram and the simulated temperature dependent JV curves are shown in figure 5.8 (a - c). The comparison of figures 5.8(b) and (c) indicates that a crossover between the light/dark JV-curves occurs. Further, the simulated $JV(T)$ curves upon white light illumination do not show any distortion and shift with a constant rate to higher voltages.

So far, the corresponding model has always been examined for CIGSe cells with small bandgap value, where a positive conduction band offset between CIGSe and CdS exist [105, 106, 110]. But figure 5.8(b - c) indicates that the presence of deep acceptor states in the CdS, can also simulate the crossover between the dark and light JV curves of wide-gap CIGSe cells. It has to be reminded again that the important parameter in this simulation is the ratio of σ_n/σ_p which was set here to 10^5. By reducing the ratio to 10^3 the potential drop in CdS will not change very large and the crossover will disappear.

5.3.2. p^+-layer on the surface of CIGSe layer

An alternative model for the crossover is a high acceptor concentration (p^+-layer) at the interface between CIGSe and CdS [104]. In equilibrium the negative charge density of

Figure 5.9: Conduction band of a wide bandgap CIGSe/p^+-layer/CdS/i-ZnO/Al:ZnO structure in dark (solid line) and upon illumination (dash-dotted line) with high density of donor states at the p^+-layer/CdS interface. The high density of acceptor states in the p^+-layer shifts the conduction band upward in darkness. Under illumination the photo-generated holes reduce the acceptor charge in the p^+-layer and thereby the Φ_b.
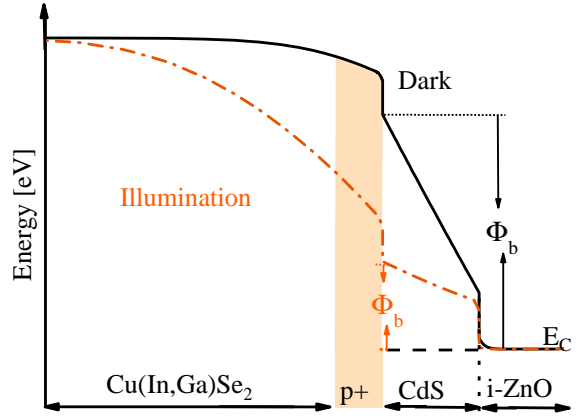
the p^+-layer induces a large potential drop in CdS and a small drop in CIGSe absorber. Upon illumination, the holes photo-generated in the buffer layer are transported to the p^+-layer reduce the acceptor charge in the p^+-layer and thereby reduce the electron barrier [4, 104, 106]. A schematic band diagram of a wide-gap CIGSe cell with a p^+-layer within CIGSe and CdS at T = 300 K is shown in figure 5.9, that the barrier height reduces under illumination.

In order to simulate the suggested model by Niemegeers et al. [104], a thin p^+-layer (10 nm) next to the absorber, between the CIGSe and CdS was added. In simulation, the maximum acceptor density of the p^+-layer was 1.5×10^{17} cm^{-3}. Nimegeers et al. [104] have considered a larger bandgap for the p^+-layer due to the existence of Cu-poor phase at the surface of CIGSe. But in this simulation, the p^+-layer has the same bandgap value of the CIGSe absorber, since lowering the valence band offset of the p^+-layer does not influence the crossover. The p^+-layer shifts the conduction band upward and eliminates the inversion. In order to increase the inversion, donor states with the density of 1×10^{13} cm^{-2} and capture cross section of $\sigma_n = 10^{-15}$ cm/s and $\sigma_p = 10^{-13}$ cm/s at the interface between the p^+-layer and CdS were considered. The simulated band diagram and $JV(T)$-curves are shown in figure 5.10(a - c). The dark JV-curves at temperatures of 110 K and 120 K had some convergence problems and could not be simulated for very large forward bias, but still it can be observed that between the dark and illuminated JV-curves the crossover is formed. Furthermore, the simulated illuminated $JV(T)$ curves do not show any distortion and is consistent with the measurement results in figure 5.5(a). It has to mentioned that the doping density of the p^+-layer and the interface states are very important. For instance, if the doping density of the p^+-layer increases or the density of interface states reduces, the conduction band of the p^+-layer is shifted upward and leads to a barrier for the photo-current [4].

In section 5.3, two different models for the crossover between the light and dark JV-curves were introduced and simulated. In the first simulation model, deep acceptor states
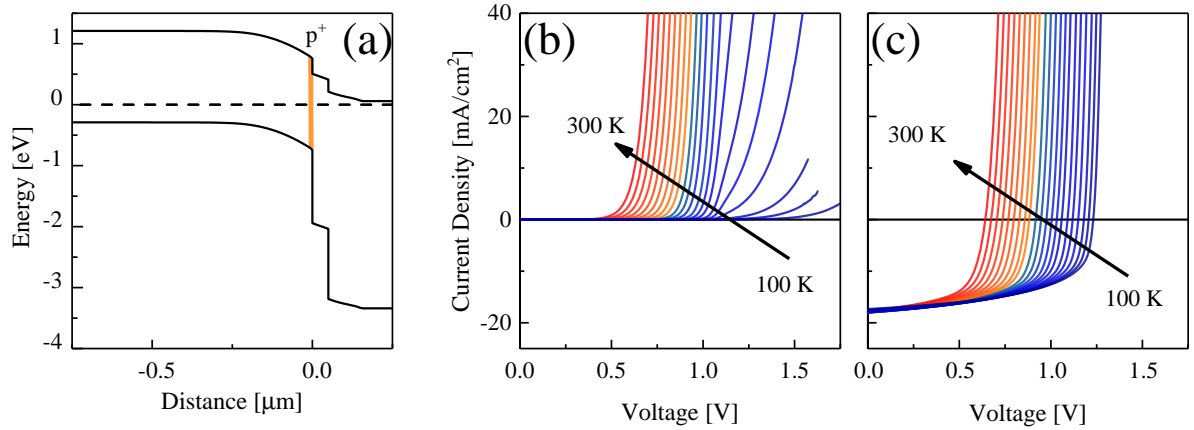
Figure 5.10.: Simulation results of p^+-layer within CIGSe and CdS for wide bandgap CIGSe solar cells ($E_{\mathrm{g}} = 1.5$ eV) (a) band diagram in equilibrium at T = 300 K, (b) dark, and (c) illuminated $JV(T)$ curves from T = 100 – 300 K in 10K steps (see Table A.2).

were programmed in the buffer layer. In the second simulation model, a p^+-layer between CIGSe and CdS was considered. The simulation results in figures 5.7 and 5.9 indicate that the crossover between the dark and light JV-curves can be simulated for the wide-gap CIGSe cells by the proposed models. In section 5.4, the model presented in section 5.3.1 will be further extended to simulate the observed phenomenon of alkali-treated samples. The model in section 5.3.2 will be discussed in chapter 7, where sodium-free substrates are studied and sodium is introduced as a post-deposition treatment.

5.4. Simulation of the alkali-treated samples

5.4.1. Modeling the $J_{\mathsf{SC}}(T)$

A temperature dependent $J_{\mathrm{SC}}(T)$ was also reported for KF treated small bandgap CIGSe solar cells [115]. It was shown that KF-PDT induces a shallow donor state below the conduction band of CIGSe (below E_{C}) that can act both as recombination center or as trap state depending on temperature [115]. At low temperature, the electrons captured in the defect state recombine instead of being re-emitted. This reduces J_{SC}. At higher temperatures, however, the electrons are re-emitted from the defect state before they recombine and thus can contribute to J_{SC} [115]. An alternative explanation for the temperature dependent J_{SC} would be a mobility of electrons $\mu_{\mathrm{n}}(T)$ which is strongly varying with temperature. This would mean that the carrier scattering mechanism is drastically changing upon alkali-treatment providing a higher temperature dependence than without alkali. For simulation of the $J_{\mathrm{SC}}(T)$ in figure 5.11, defect states with asymmetric capture
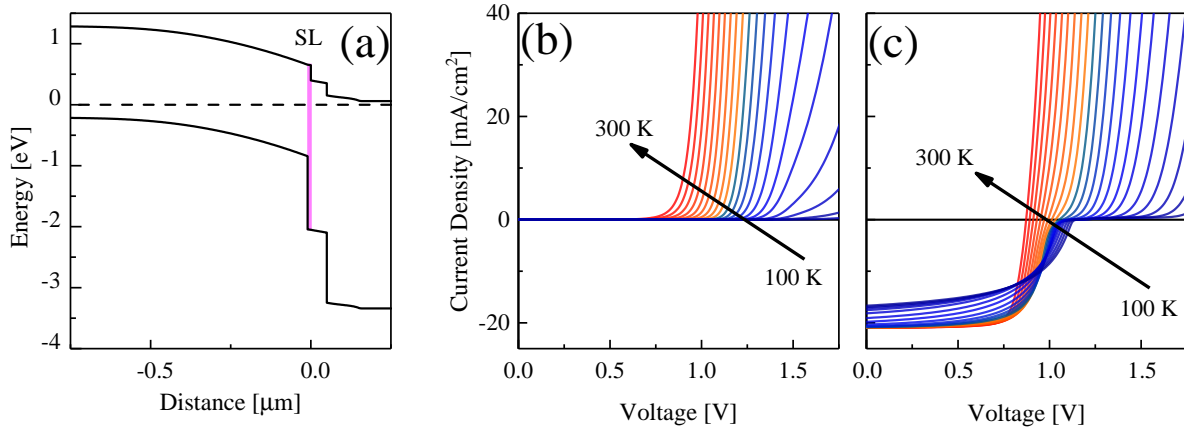
Figure 5.11.: Simulation results of a deep valence band edge of the surface layer on the CIGSe/SL/CdS/i-ZnO/ZnO:Al hetero-structure. The surface layer has a bandgap of 2.7 eV, (a) band diagram, (b) dark, and (c) illuminated $JV(T)$ evolution from T = 100 – 300 K in 10K steps. In the CdS, deep acceptor states was programmed to simulate the crossover (see Table A.3).

cross sections below the CIGSe conduction band was considered (for parameters see Table A.3). Similar to the experimental data in figure 5.5, the short circuit current density comes out temperature dependent.

5.4.2. Modeling the double-diode behavior

In figure 5.5(b - d), a double-diode behavior was observed for the alkali-treated samples. This form of illuminated JV-curve is a sign for a secondary barrier in the solar cell [86, 116, 117]. In contrast to a kink which occurs in the third or fourth quadrant of the JV-curve and which is due to a barrier for the photo-current [4], the resumption of the injection current depicting a double-diode behavior occurs in the first quadrant. It indicates a barrier for the diode current which is not removed by illumination.

In order to simulate the double-diode behavior in figure 5.5(b - d), a surface layer formed by the alkali-PDT is used which has the following properties: (i) a conduction band alignment to the underlying CIGSe, (ii) aligned valence band edges at the SL/CdS interface, and (iii) defect states present at the newly formed CIGSe/SL interface. All other physical properties such as doping density and mobility are programmed identical to the CIGSe layer. The resulting band diagram and the simulated $JV(T)$ curves are shown in figure 5.11(a - c). The crossover is simulated with deep acceptor states in the buffer layer and the $J_{SC}(T)$ by a shallow donor state. Comparing figure 5.11(a) with figure 5.8(a) reveals that the main difference of the band diagrams is the local position of the valence band discontinuity which is shifted by introducing the SL, with respect to the conduction band discontinuity.
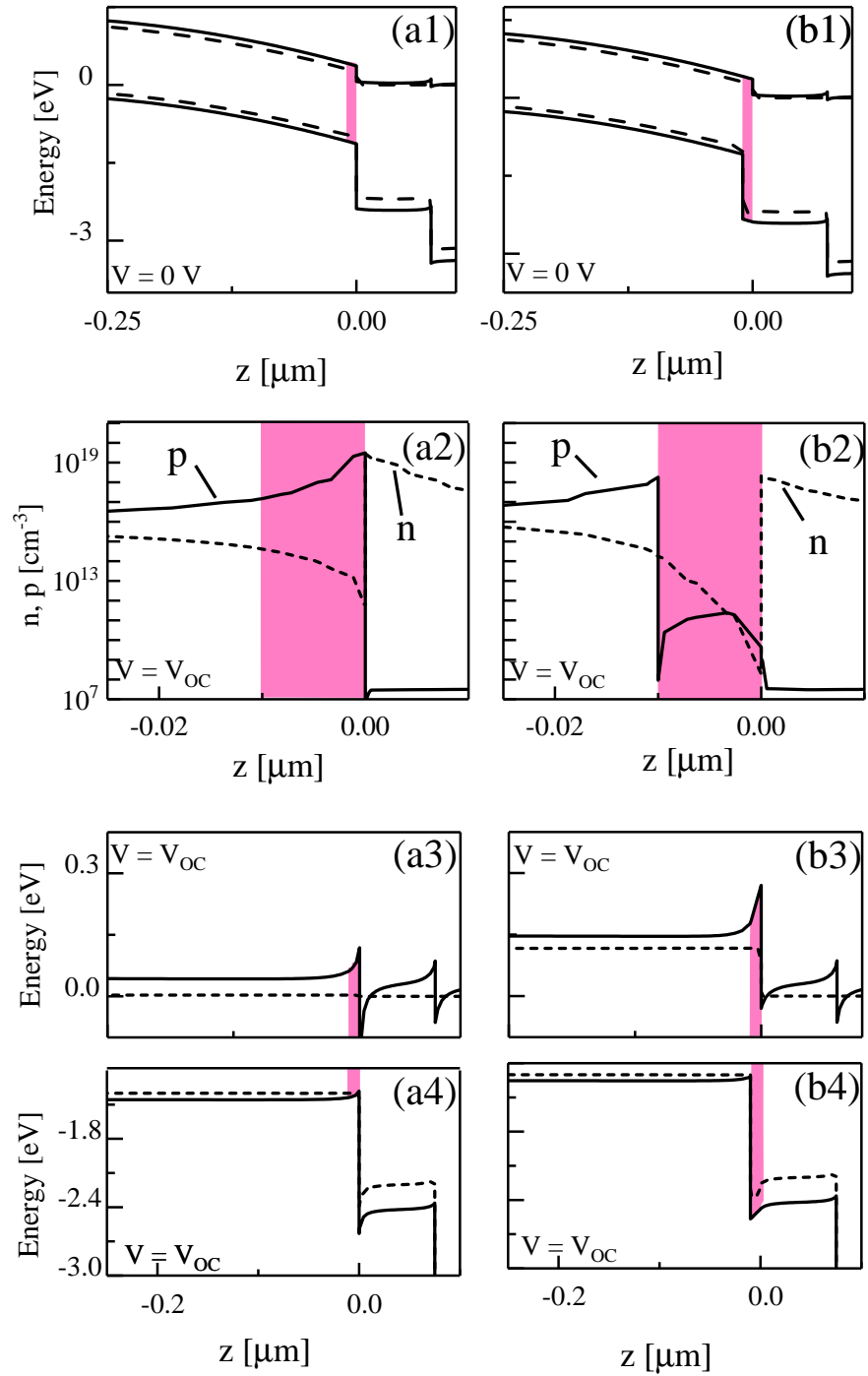
Figure 5.12.: Simulated band diagram and carrier densities for a device without (left column) and with (right column) SL at T = 100 K. (a - b) Band diagram at $V = 0$ under illumination. (a2,b2) Carrier densities in CIGSe/SL/CdS structure. (a3, b3) E_C and E_{Fn} at $V = V_{OC}$, (a4, b4) E_V and E_{Fp} at $V = V_{OC}$. The pink layer is the SL layer.

In figure 5.11(c) it is visible that this band diagram produces the double-diode behavior as found in the measurement results of the alkali-treated sample in figure 5.5. Above V_{OC}, the simulated JV-curves at low temperature show a plateau at around zero current in case of the applied SL in figure 5.11(a). By simulation it was found that reducing the SL thickness to 5 nm instead of 10 nm substantially reduces the double-diode behavior. This indicates that the thickness of the SL is in the range of 10 nm.

In order to explain the formation of the double-diode behavior of the alkali-treated sample, first the untreated case will be discussed based on figure 5.12(a) where no double-diode behavior is observed. For large forward bias in figure 5.12(a), an accumulation layer for electrons on the CdS side and an accumulation layer for holes on the CIGSe side is formed (note that this simulation requires the use of Fermi-Dirac statistics implemented in Sentaurus TCAD). Both electron and hole densities form a double-layer of equal charge density as depicted in figure 5.12(a2). The high density of electrons on the CdS side now allows thermionic emission of electrons over the remaining barrier. This explains why there is no double-diode behavior for the untreated cell in experiment (Fig. 5.5) and simulation (Fig. 5.8). However, if the two accumulation layers for n and p become more distant through implementation of an additional layer, the charge densities in the accumulation regions reduces (see Fig. 5.12(b2)) and the electron concentration (at intermediate voltage bias) does not suffice to drive a high current by thermionic emission. This brings out the double-diode behavior also in simulation (Fig. 5.11). Only under strongly increased simulated voltage bias, the thermionic emission current is reestablished as is the case for the experimental JV-curve of alkali- treated devices in figure 5.5(b - d). In figure 5.13(a - b), the influence of the valence band edge position of the surfae layer on the interface carrier densities versus the voltage at T = 300 K is illustrated. If the surface layer has the same bandgap of the absorber layer, then the holes and electrons at the interface increases with the voltage (Fig. 5.13(a)). However, if the bandgap of the SL is increased to 2.7 eV (Fig. 5.13(b)), the hole densities are reduced for all voltage biases. As the hole density decreases, the recombination rate at the interface reduces (Eq. 2.5.9), which in turn increases the V_{OC} [118].

5.4.3. Modeling the V_{OC} saturation

Figure 5.14 gives the data of $V_{OC}(T)$ simulated for the devices in figure 5.8 and figure 5.11. As for the untreated experimental device in Figure 5.5, an overall reduced $V_{OC}(T)$ is simulated in figure 5.14 (red open squares) which extrapolates to 1.29 V at 0 K. The simulated small extrapolated $V_{OC}(0\ K)$ indicates the dominance of interface recombination under open-circuit condition which was programmed by defect states at the CIGSe/CdS interface (see Table A.3). The $V_{OC}(T)$ curve of the untreated device can be fitted by a mostly linear relation over the complete temperature range. Figure 5.14 also includes the
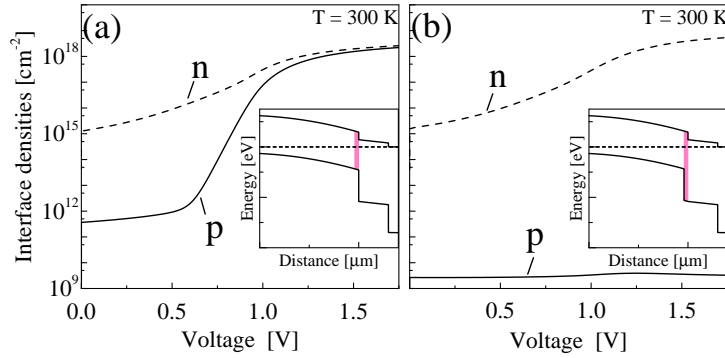
Figure 5.13.: Influence of the valence band edge on the interface carrier densities. Simulation results of the carrier densities at the interface, (a)E_g (SL) = 1.5 eV, and (b) E_g (SL) = 2.7 eV. The low valence band edge, reduces the hole concentration at the interface.
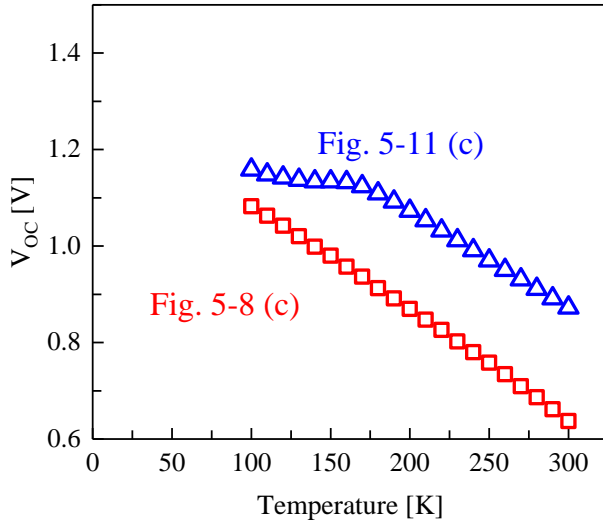
Figure 5.14: The open circuit voltage (V_{OC}) versus temperature from figure 5.8 and 5.11. The V_{OC} of the samples with the double-diode behavior saturates at low temperatures, although no back barrier height was programmed in the simulation.

simulated $V_{OC}(T)$ for the solar cell in Figure 5.11 (blue open triangles) which represents the RbF-treated device. In agreement with the experimental data in figure 5.6, a saturation of $V_{OC}(T)$ towards low temperatures is simulated. This saturation is the result of a reduction of the collection efficiency $\eta(V)$ at high voltages (see Fig. E.4). Consulting figure 5.12(b3), an electron barrier in the conduction band – formed by the accumulation layer at distance -0.01 μm plus the potential drop in the SL – can be seen. This barrier impedes the electron current towards the n-side of the junction at low temperature and leads to a small $\eta(V_{OC})$ for the device in figure 5.11(a). In consequence, the $V_{OC}(T)$ for the device with SL deviates from the linear behavior at low temperatures. This deviation is similar to a back barrier [108, 119]. Also the untreated device shows a barrier for the photo-current in figure 5.12. However, this barrier consists only of the band bending in the accumulation layer and therefore is smaller than the barrier from accumulation layer plus potential drop in the SL. Thus, the potential drop in the SL is a result of the lowered valence band edge.

5.4.4. Discussion on the simulation model

As shown in figure 5.11 a good correlation between the simulation and measurement results in figure 5.5(b - d) was obtained. The simulation model in figure 5.11 suggests that the alkali-PDT forms a new surface layer between the CIGSe and the CdS (see Fig. 5.11). The addition of the surface layer next to the CIGSe absorber explains the double-diode behavior and the saturation of the V_{OC} at low temperatures of the alkali-treated samples (see figures. 5.11 and 5.14). Reports on KF-treated CIGSe samples with low bandgap have revealed that the potassium forms a new phase on the CIGSe surface and shifts the valence band edge downward [10, 12]. For RbF-treated samples, it has also been indicated that the valence band edge is lower compared to an untreated sample [11]. But all these findings are limited to CIGSe absorbers with small bandgap value and such an examinations is not conducted for wide-gap CIGSe absorbers, yet. Nevertheless, it was assumed that the alkalis lower the valence band edge and does not have any impact on the conduction band. The reason is that a positive conduction band leads to a barrier for the photo-current and brings a kink in the fourth quadrant.

Another phenomenon of the alkali-treated samples was the temperature dependency of the short-circuit current density. Simillar to Pianezzi et al. a shallow donor state below the conduction band in the bulk of the absorber was considered to bring out the $J_{SC}(T)$ [115]. The alkali-treated samples (see Table 5.1) induced three different phenomena, and two of them (the double-diode behavior and the saturation of the V_{OC}) could be explained by a surface layer with a deep valence band edge at the CIGSe/CdS hetero-interface, and the $J_{SC}(T)$ could be simulated by programming a defect in the bulk of the absorber. The exact origin of the temperature dependency of the alkali-treated requires further investigations, but it might that the $J_{SC}(T)$ is also related to a modification at the hetero-interface and not the bulk.

In chapter 6, it will be shown that the recombination at the interface is still dominant for wide-gap alkali-treated samples. Therefore, interface states between the CIGSe absorber and the surface layer was programmed to keep the dominant recombination at the interface (see Table A.3).

5.5. Concluding remarks

In agreement with the previous reports on small bandgap CIGSe cells, it was observed that the introduction of alkalis (K, Rb, and Cs) after the deposition of CIGSe improves the V_{OC} and the efficiency. It was shown that although the V_{OC} of RbF-treated cell increases about 100 mV compared to the untreated sample, the TRPL-transients of the untreated

and alkali-treated samples show the same decay curves.

In section 5.2, the electronic charge transport of wide-gap CIGSe cells was studied. For this purpose, the temperature dependent JV curves in dark and upon white light illumination were measured and simulated. For the untreated and treated samples a crossover between the dark and the light JV curves was observed. This anomaly could be simulated in two different ways; either considering deep midgap defects in CdS or a p^+-layer between the CIGSe and CdS. As indicated in figures 5.8 and 5.10, both models could explain the crossover between the light and dark JV-curves of wide-gap CIGSe cells.

Besides the crossover, for the alkali-treated samples a double-diode behavior at low temperatures was observed. The numerical simulations suggests that the post-deposition treatment of the alkalis introduce a new surface layer (SL) next to CIGSe layer (between CIGSe and CdS) and shifts the valence band edge downward (Fig. 5.11), which correlates fairly well with the previous findings [10–12].

6. Dominant recombination path Cu(In$_{1-x}$,Ga$_x$)Se$_2$

In chapter 5, it has been shown that the V_{OC} of the CIGSe cells with different gallium concentrations increases when the absorber is treated with heavy alkalis (K, Rb and Cs). Furthermore, the activation energy (E_A) of the wide-gap cells increases to values close to the bandgap values ($E_A \approx E_g$), while the untreated cell was showing an E_A below the bandgap value ($E_A < E_g$). Although an activation energy smaller than the bandgap value hints to a dominant recombination at the interface, an E_A equal to the bandgap is not necessarily an indication of a dominant recombination in the bulk [4, 120]. An experiment which can be used to diagnose the dominant recombination path is monitoring the open-circuit voltage upon illumination [28, 75, 121]. In this chapter, the V_{OC} transients ($\Delta V_{OC}(t)$) of samples with GGI = 0.3 and GGI = 0.75 for both treated and untreated are studied to evaluate the dominant recombination path. At the end for each recombination path a relation for $\Delta V_{OC}(t)$ is derived and the meaning of different slopes of the measured $\Delta V_{OC}(t)$ are explained.

6.1. Review

Upon red-light illumination, the doping density of the CIGSe increases and dependent on the dominant recombination path different transients of open-circuit voltage can be observed [14, 28]. This can be summarized as follows:

- For a cell limited by recombination in the QNR, the $V_{OC}(t)$ increases under illumination because the increased doping density shifts the hole-Fermi level closer to the valence band and increases the built-in voltage and thereby the $V_{OC}(t)$ [122]. The band diagrams of a device limited by recombination in the QNR at V_{OC} with doping densities of 1×10^{16}cm^{-3} and 5×10^{16}cm^{-3} are illustrated (Fig. 6.1(a - b)). The red line below the conduction band is a shallow defect state. As can be seen in figure 6.1(b), the splitting of the quasi-Fermi levels is increased upon higher doping density which increases the V_{OC}.
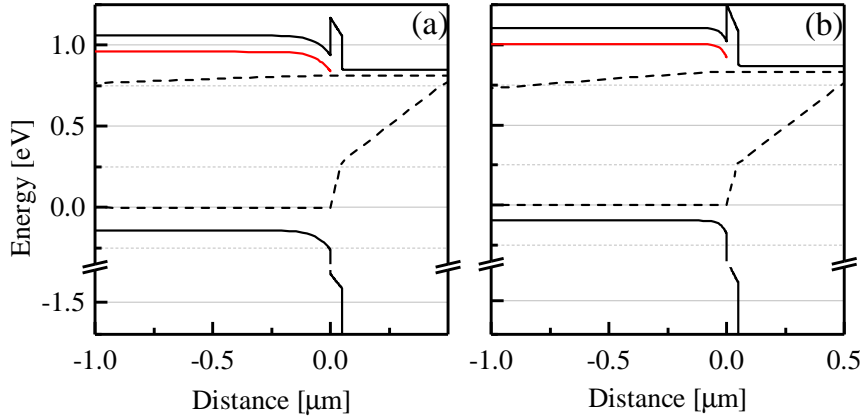
Figure 6.1.: The band diagrams of a sample limited by recombination in the QNR under red-light illumination at V_{OC} for different doping densities, (a) $N_{A,a} = 1 \times 10^{16} \mathrm{cm}^{-3}$, (b) $N_{A,a} = 5 \times 10^{16} \mathrm{cm}^{-3}$. The red line below the conduction band is a shallow defect state. Under red-light illumination the net doping density increases and the V_{OC} increases.

- If a device is limited by recombination in the SCR, the increased doping density (Fig. 6.2(b)) reduces the total width of the SCR. The band diagrams of a sample limited by SCR recombination at two different doping densities are illustrated in figure 6.2. For a device limited by recombination in the SCR, a midgap defect is programmed which is sketched with a red solid line (Fig. 6.2(a - b)). As the doping density increases (Fig. 6.2(b)), the zone of the highest recombination rate reduces, this effect leads to a gradual increase of V_{OC} during illumination.
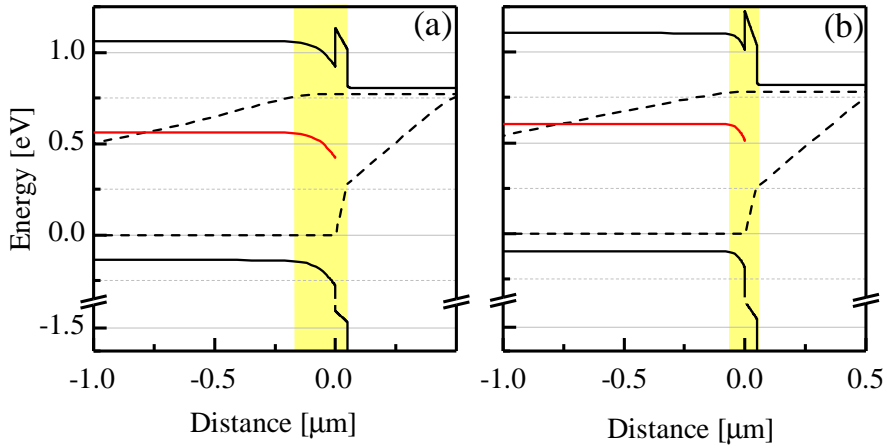
Figure 6.2.: The band diagrams of a sample limited by recombination in the SCR under red-light illumination at V_{OC}, (a) $N_{A,a} = 1 \times 10^{16}$ cm^{-3}, (b) $N_{A,a} = 5 \times 10^{16}$ cm^{-3}. The red line is a midgap defect state, and the recombination zone is highlighted in yellow. Under red-light illumination, the recombination zone reduces and V_{OC} increases.

- If the device is limited by the interface recombination, then the open-circuit voltage decreases upon illumination. The reason is that the recombination is controlled by holes at the interface (Eq. 2.5.9). With the increase of the doping density the hole
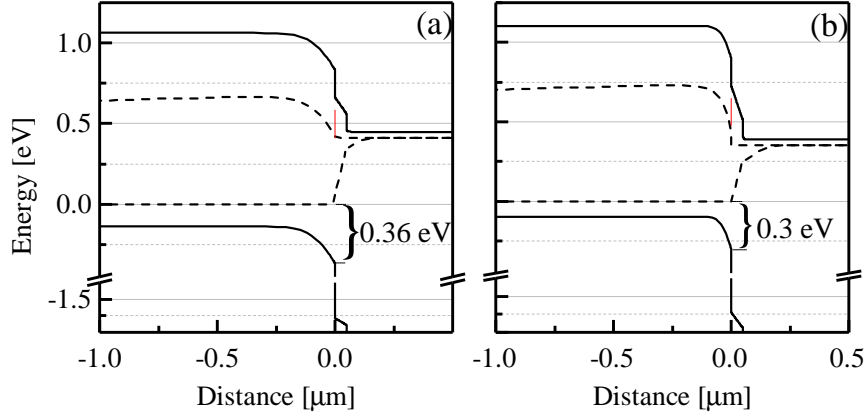
Figure 6.3.: The band diagrams of a sample limited by recombination at the interface under red-light illumination at V_{OC}, (a) $N_{A,a} = 1 \times 10^{16} \text{cm}^{-3}$, (b) $N_{A,a} = 5 \times 10^{16} \text{cm}^{-3}$. The red line marks the position of the interface state.

barrier ($E_{p,a}^{if}$) decreases (Fig. 6.3(b)). In figure 6.3, the band diagrams of a sample limited by interface recombination with two different doping densities are depicted. In comparison to figures 6.2 and 6.1 a negative band offset between the absorber and the buffer layer is programmed and defect states at the absorber/buffer interface are introduced. It can be observed that when the doping density increases from 1×10^{16} cm^{-3} to 5×10^{16} cm^{-3}, the hole barrier is reduced from 0.36 to 0.3 eV. The reduced hole barrier increases the hole density at the interface and thus the recombination rate at the interface (Eq. 2.5.9). The increased recombination rate at the interface results in a V_{OC} drop under illumination. The reduced splitting of the quasi-Fermi levels at the interface (Distance = 0 μm) due to the higher doping density of the absorber can be seen in figure 6.3.

6.2. Open circuit voltage transients ($V_{OC}(t)$)

The V_{OC}-transients of the two series of samples with GGI = 0.3 and 0.75 are shown in figure 6.4(a - b). The $V_{OC}(t)$ data of the first 600 s have been discarded due to anticipated thermal instability after initial light exposure. All samples with GGI = 0.3 exhibit V_{OC}-transients with positive slope, which indicates dominant recombination in the bulk (space charge or quasi-neutral region) [14, 75]. The slopes of the $\Delta V_{OC}(t)$ (treated and untreated samples) change to negative values as the GGI ratio increases to 0.75. The decline of the $V_{OC}(t)$ for high gallium content samples confirm a dominant recombination path at the interface [14, 28, 75], regardless of the increased E_A of the alkali-treated samples as shown in figure 5.6. Such a difference between low GGI cells and high GGI cells is known and indicates that the recombination path changes from the Bulk/SCR to the interface [14, 75].
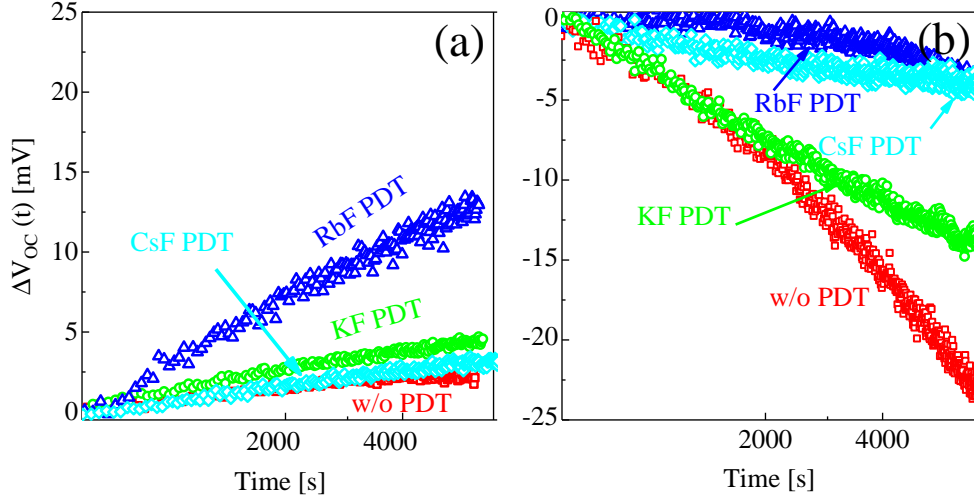
Figure 6.4.: The V_{OC}-transient of untreated and treated samples with the (a) GGI = 0.3, and (b) GGI = 0.75. The CGI of samples with the GGI = 0.3 varies between 0.83 - 0.85 and the CGI of the samples with the GGI = 0.75 changes between 0.85 - 0.88. The thickness of KF, RbF and CsF are 6 nm, 25 nm, and 8 nm, respectively.

While the sign of $d\Delta V_{OC}(t)/dt$ points out the dominant recombination path, one has to notice the different slopes for one identical GGI. As can be seen for GGI = 0.3 devices (Fig. 6.4(a)), the $\Delta V_{OC}(t)$ of the RbF-treated sample increases at a faster pace, while the ΔV_{OC} of the untreated sample grows slowly. The $\Delta V_{OC}(t)$ of samples with the GGI = 0.75 show different slopes for the alkali-treated and untreated cells as well (Fig. 6.4(b)). The $V_{OC}(t)$-slope of the untreated sample falls down sharply, while the $V_{OC}(t)$ of RbF and CsF-treated samples decreases in a slower rate.

In order to explain the different slopes of the alkali-treated and untreated samples a relation for the $\Delta V_{OC}(t)$ is required. From the JV-curve of the one-diode model the time dependent V_{OC} can be written as [4]:

$$V_{OC}(t) = -\frac{A(t)\, k_{B}\, T}{q}\, ln\left(\frac{J_0(t)}{J_{ph}}\right). \qquad (6.2.1)$$

For samples with the dominant recombination path at the interface, the diode quality factor ($A(t)$) changes under light soaking. The reason is that the doping density ($N_{A,a}(t)$) is hidden in the diode quality factor [4, 15, 30], which makes the diode quality factor not a constant but a variable parameter. Therefore the notation $A(t)$ is used in equation 6.2.1. The changes of $V_{OC}(t)$ (i.e. $\Delta V_{OC}(t)$) is defined as:

$$\Delta V_{OC}(t) = V_{OC}(t) - V_{OC}(t_0) = -\frac{k_{B}T}{q}\left[A(t)\, ln\left(\frac{J_0(t)}{J_{ph}}\right) - A(t_0)\, ln\left(\frac{J_0(t_0)}{J_{ph}}\right)\right]. \qquad (6.2.2)$$

Here, t_0 is the initial state or the relaxed state. The relaxed state is achieved after keeping the sample for few hours at elevated temperatures in the dark [4]. At this state, the doping density ($N_{A,a}$) and the V_{OC} are very low [4]. In the next step the logarithm of equation

6.2.2 is expanded and equation 2.4.2 is used to replace the saturation current density (J_0) with the reference current density (J_{00}). A more detailed derivation is shown in appendix B. The final relation for $\Delta V_{\mathrm{OC}}(t)$ is reduced to:

$$
\begin{aligned}
\Delta V_{\mathrm{OC}}(t) = & - \frac{k_{\mathrm{B}}T}{q} A(t_0) \, ln \left(\frac{J_{00}(t)}{J_{00}(t_0)} \right) \\
& - \frac{k_{\mathrm{B}}T}{q} (\Delta A) \, ln \left(\frac{J_{00}(t)}{J_{\mathrm{ph}}} \right).
\end{aligned}
\tag{6.2.3}
$$

Equation 6.2.3 indicates that the $\Delta V_{\mathrm{OC}}(t)$ is related to the reference current density ($J_{00}(t)$), photo current density (J_{ph}), and the diode quality factor ($A(t)$). The term ΔA is the changes of the diode quality factor and is defined via $A(t) = A(t_0) + \Delta A$. In order to calculate the $\Delta V_{\mathrm{OC}}(t)$, the $J_{00}(t)$ must be known, but $J_{00}(t)$ is related to the dominant recombination path. Therefore, in the following $\Delta V_{\mathrm{OC}}(t)$ for different recombination paths is derived. For the sake of the simplicity instead of the absorber/buffer/window structure, a simple absorber/window (p/n^+) is assumed.

6.2.1. $\Delta V_{\mathrm{OC}}(t)$ for QNR recombination

The reference current density ($J_{00}(t)$) for a dominant recombination path in the QNR is [4]:

$$
J_{00}^{qnr}(t) = \frac{D_{\mathrm{n}} N_{\mathrm{c,a}} N_{\mathrm{v,a}}}{N_{\mathrm{A,a}}(t)} \frac{d\eta(z)}{dz} \bigg|_{z=-w_{\mathrm{a}}}
\tag{6.2.4}
$$

To calculate $\frac{d\eta(z)}{dz} \big|_{z=-w_{\mathrm{a}}}$, it is assumed that the electron diffusion length (L_{n}) is shorter than the absorbers thickness ($L_{\mathrm{n}} \ll d_{\mathrm{n}}$). In this case the recombination at the back contact is not the dominant process and the collection function is defined by $\exp\left((z + w_{\mathrm{a}})/L_{\mathrm{n}}\right)$ [18]. As a result the derivative of $\frac{d\eta(z)}{dz} \big|_{z=-w_{\mathrm{a}}}$ is a constant parameter (L_{n}^{-1}) and does not change upon illumination. Furthermore, the diode quality factor of the samples with dominant recombination in the QNR is equal to one. Consequently, $\Delta A = 0$, and the second term in equation 6.2.3 vanishes. With these considerations, for a dominant recombination in the QNR the relation for $\Delta V_{\mathrm{OC}}^{qnr}(t)$ is obtained:

$$
\Delta V_{\mathrm{OC}}^{qnr}(t) = \frac{k_{\mathrm{B}}T}{q} \, ln \left(\frac{N_{\mathrm{A,a}}(t)}{N_{\mathrm{A,a}}(t_0)} \right).
\tag{6.2.5}
$$

From equation 6.2.5, it can be understood that $\Delta V_{\mathrm{OC}}(t)$ is logarithmically dependent on the variation of the doping density $N_{\mathrm{A,a}}(t)$. As a result, with the fast growth of the doping density $N_{\mathrm{A,a}}(t)$, a larger positive slope for $\Delta V_{\mathrm{OC}}(t)$ is calculated.

6.2.2. $\Delta V_{OC}(t)$ for SCR recombination

The $J_{00}(t)$ for a dominant recombination in the SCR is [4]:

$$J_{00}^{scr}(t) = \frac{\pi\, k_B T}{2\, F_m(t)} \left(\frac{N_{c,a} N_{v,a}}{\tau_{n0,a} \tau_{p0,a}} \right)^{\frac{1}{2}}. \tag{6.2.6}$$

In order to derive a relation for $\Delta V_{OC}^{scr}(t)$ the equation 6.2.6 is inserted in equation 6.2.3. The diode quality factor is constant, but the electric field (F_m) is dependent on the doping density and changes upon illumination. To obtain the $\Delta V_{OC}^{scr}(t)$, some assumptions are made which are shown in appendix B. The final relation for $\Delta V_{OC}^{scr}(t)$ reduces to:

$$\Delta V_{OC}^{scr}(t) = \frac{k_B T}{q}\, ln\left(\frac{N_{A,a}(t)}{N_{A,a}(t_0)} \right) \tag{6.2.7}$$

Comparing the equations 6.2.7 and 6.2.5 indicates that the $\Delta V_{OC}(t)$ for the QNR and SCR are identical and solely dependent on the doping density. Therefore, by monitoring the V_{OC}-transients upon red light illumination the dominant recombination path between SCR and QNR cannot be distinguished.

6.2.3. $\Delta V_{OC}(t)$ for interface recombination

In chapter 5, it has been shown that the post-deposition treatment of alkalis introduces a new surface layer (SL) that shifts the valence band edge downward at the hetero-interface. Therefore, a simple absorber/window junction cannot describe the V_{OC}-transients of the alkali-treated samples. Obereigner et al. have suggested that considering an absorber/buffer/window layer would be more precise to describe the V_{OC}-transients of wide-gap CIGSe cells [14]. Therefore, there was a motivation to find the accurate band-diagram model that describes the V_{OC}-transients. In the following two different band diagrams are examined:

- an absorber/SL/window hetero-structure, where the surface layer has a low valence band edge relative to the absorber,

- an absorber/SL/buffer/window hetero-structure, where the surface layer has a deep valence band edge relative to the absorber layer.

The absorber/SL/window hetero-structure

For an inverted interface, the electrons are the majority carriers at the interface and their recombination rate is $R^{if} \approx p^{if} S_p$. The hole density for an absorber/SL/window structure
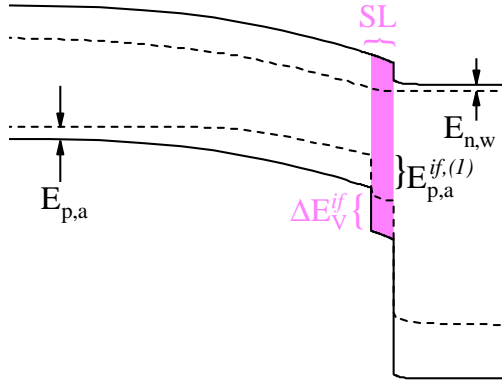
Figure 6.5: The band diagram of an absorber/S-L/window hetero-structure. The surface layer has a deep valence band edge relative to the absorber layer.

according to figure 6.5 is given by [34]:

$$p^{if}(V) = N_{V,a}\,exp\left(-\frac{E_{p,a}^{if,(1)}(N_{A,a}, V_{OC}) + \Delta E_V^{if}}{k_B T}\right) \qquad (6.2.8)$$

From equation 6.2.8, it can be seen that a deep valence band edge reduces the hole density at the interface. If the valence band edge is not shifted downward ($\Delta E_V^{if} = 0$), then the hole barrier reduces to $E_{p,a}^{if,(1)}(N_{A,a}, V_{OC})$ and is given by [4]:

$$E_{p,a}^{if,(1)}(N_{A,a}, V_{OC}) = \left(\frac{\epsilon_w N_{D,w}}{\epsilon_w N_{D,w} + \epsilon_a N_{A,a}}\right) q\left(V_{bi} - V_{OC}\right) + E_{p,a} \qquad (6.2.9)$$

The term $(\epsilon_w N_{D,w})/(\epsilon_w N_{D,w} + \epsilon_a N_{A,a})$ influences the inversion degree of the hole barrier. It can be seen that if the term $\epsilon_w N_{D,w}$ becomes large then $E_{p,a}^{if,(1)}(N_{A,a}, V_{OC})$ increases [4]. In the next step, from equation 6.2.8, the recombination current density must be calculated and the saturation current density has to be extracted. For the simple case with $\Delta E_V^{if} = 0$, the equations are derived in appendix B, but as mentioned earlier, the absorber/window band diagram is just applicable for an untreated sample and not an alkali-treated sample. Due to the complexity of the relations, the equation 6.2.10 will be solved numerically [14] for different ΔE_V^{if}-values in order to determine the $V_{OC}(t)$.

$$0 = qS_p N_{V,a}\,exp\left(-\frac{E_{Fp}^{if,(1)}(N_{A,a}, V_{OC}) + \Delta E_V^{if}}{k_B T}\right) + J_{SC} \qquad (6.2.10)$$

The absorber/SL/buffer/window hetero-structure

In figure 6.6 an absorber/SL/buffer/window structure is assumed. Similar to figure 6.5, the surface layer has a deep valence band edge relative to the absorber layer. The modified hole barrier in this case is the sum of $E_{p,a}^{if,(2)}$ and the constant term ΔE_V^{if}. Therefore, the

Figure 6.6: The band diagram of an absorber/S-L/buffer/window hetero structure. The surface layer has a deep valence band edge relative to the absorber layer.
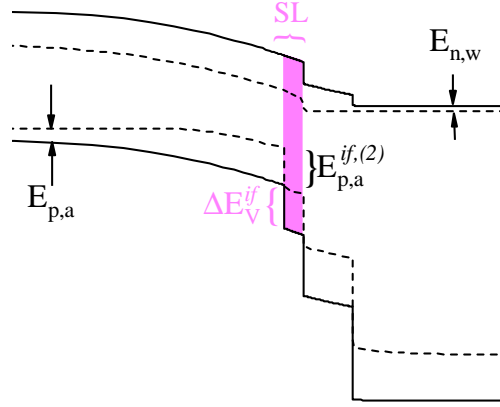
hole density at the interface is the same as in equation 6.2.8 but instead of $E_{\mathrm{p,a}}^{if,(1)}$, the term $E_{\mathrm{p,a}}^{if,(2)}$ must be employed. The $E_{\mathrm{p,a}}^{if,(2)}$ for an absorber/buffer/window is given in equation 2.1.2. In order to compute the $V_{\mathrm{OC}}(t)$ for an absorber/buffer/window structure, the term $E_{\mathrm{p,a}}^{if,(1)}$ has to be substituted by $E_{\mathrm{p,a}}^{if,(2)}$ in equation 6.2.10. The equation 6.2.10 has to be solved numerically. Except for the doping density and the built-in voltage in equation 2.1.2 other parameters are constant and their values can be found in reference [4]. In chapter 5, it has been shown that for an untreated sample, the bandgap of the absorber bulk and the near-surface region of the absorber are identical and the valence band edge is not shifted downward. Therefore for calculation of the $\Delta V_{\mathrm{OC}}(t)$ for the untreated case, the equation 6.2.10 is solved numerically with the condition that $\Delta E_{\mathrm{V}}^{if} = 0$. For the alkali-treated sample, the $\Delta E_{\mathrm{V}}^{if}$ is set as a variable parameter that changes between 0 - 0.4 eV.

So far, it was shown that samples with the same GGI have different slopes of ΔV_{OC} upon red-light illumination (Fig. 6.4). Therefore, in the second section, relations for $\Delta V_{OC}(t)$ were derived to obtain the influential parameters in the $\Delta V_{OC}(t)$-slope. The relations for $\Delta V_{OC}(t)$ in the QNR and SCR suggest that the slope of $\Delta V_{OC}(t)$ is dependent on changes of the doping density. For cells limited by interface recombination the doping density is also one of the parameters that can influence the slope of the $\Delta V_{OC}(t)$. Therefore, in the next section the doping transients of the untreated and RbF-treated samples will be examined.

6.3. Correlation of the doping transients and open-circuit voltage

In order to determine the doping transient of the absorber $(N_{\mathrm{A,a}}(t))$, the admittance spectra of the samples were measured as explained in section 3.6.3. The admittance spectra of the samples are shown in the appendix C. In the second step the capacitance

spectrum at the space charge region was extracted which is a function of doping density (Eq. 2.1.5) and the built-in voltage. The built-in-voltage is also dependent on the doping density (Eq. 2.1.1). Then by solving simultaneously the equations 2.1.5 and 2.1.1 the doping density was calculated [14]. The calculated doping densities were plotted versus time and are shown in the following. The time here is the duration that the sample was illuminated at a constant temperature of 298 K. To calculate the $\Delta V_{\mathrm{OC}}(t)$, the doping transient ($N_{\mathrm{A,a}}(t)$) was fitted with a power law function [14]:

$$N_{\mathrm{A,a}}(t) = N_{\mathrm{A,a}}(t_0) \left(1 + (\frac{t}{\tau_{\mathrm{c}}}) \right)^{\beta} \tag{6.3.1}$$

Here, $N_{\mathrm{A,a}}(t_0)$ is the doping density in the relaxed state, τ_{c}^{-1} is the transition rate, and β is the slope of the doping transients at large time scales [14].

6.3.1. Samples with GGI = 0.3

The doping transients, $N_{\mathrm{A,a}}(t)$, of samples with GGI = 0.3 are illustrated in figure 6.7(a). The fitted doping transients are shown as dashed lines in figure 6.7(a). The fitted parameters are shown in figure 6.7. In the relaxed state ($t = 0$) the doping density of the alkali-treated is slightly higher than the untreated sample (Fig. 6.7(a)). This is in agreement with previous reports that post deposition treatment of alkalis increases the doping density $N_{\mathrm{A,a}}(t_0)$ [6, 41, 45, 96].

	β	$\tau_{\mathrm{c}}^{-1}[\mathrm{s}^{-1}]$
untreated	0.025	2.7E19
RbF-treated	0.085	14895
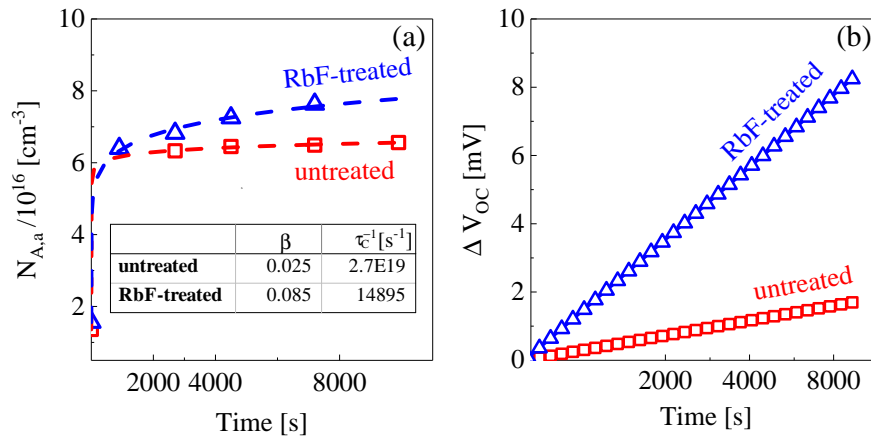
Figure 6.7.: The correlation between the doping transients and $\Delta V_{\mathrm{OC}}(t)$ for samples with the GGI = 0.3, (a) measured doping transients ($N_{\mathrm{A,a}}(t)$) of RbF-treated and untreated samples, (b) calculated $\Delta V_{\mathrm{OC}}(t)$ from the doping transients ($N_{\mathrm{A,a}}(t)$). In order to calculate the $\Delta V_{\mathrm{OC}}(t)$ the equation 6.2.7 was used.

As the samples are exposed to red light at 298 K, the doping densities ($N_{\mathrm{A,a}}(t)$) show a large increase from the relaxed state, followed by a slowing down of the growth rates at

larger times. As can be seen in figure 6.7, the doping densities of both samples increase, but the doping density of the RbF-treated sample shows a larger growth rate than of the untreated sample at larger times ($\beta^{RbF} > \beta^{wo}$).

In section 6.2.2, it was shown that regardless of the dominant recombination path either in SCR or QNR, the $\Delta V_{OC}(t)$ relations are identical. Therefore, from the known $N_{A,a}(t)$, the $\Delta V_{OC}(t)$ is calculated from equation 6.2.7 and is depicted in figure 6.7(b). As can be seen, the calculated $\Delta V_{OC}(t)$ of the RbF-treated sample increases faster than the untreated sample (Fig. 6.7(b)) and correlates favorably well with the measurement results in figure 6.4. This indicates that for devices with the dominant recombination in the QNR and SCR, the doping density is the crucial quantity to describe the slopes of the V_{OC}-transients.

6.3.2. Samples with GGI = 0.75

The doping transients of RbF-treated and untreated samples with high gallium concentration are shown in figure 6.8(a). In the relaxed state, the RbF-treated sample shows slightly a higher doping density ($N_{A,a}(t_0)$) than the untreated sample. This means similar to the case with GGI = 0.3, RbF-PDT increases the doping density in the relaxed state. In the initial phase of illumination, the doping density increases to larger values for both samples, however, there is a large difference in the magnitude. In the initial phase, $N_{A,a}$ of the RbF-treated sample increases by a factor of 6 times beyond its relaxed state value, while for the untreated sample it increases by a factor of just 2. The strong increase at the initial phase for RbF-treated is reflected in equation 6.3.1 by a small τ_c. The doping transients fitted with the power law function from equation 6.3.1 are shown with dashed lines in figure 6.8(a). It must be reminded that both samples were measured simultaneously. This means that the relaxation times of both samples were the same and the influence of any errors such as lamp intensity can be discarded.

In order to examine the reproducibility of the $V_{OC}(t)$-transients and the doping transients of high gallium content devices, another set of samples with a GGI of 0.83 (RbF-treated and untreated) was analyzed. The measured $\Delta V_{OC}(t)$ and doping-transients are shown in figure C.2(a - b). Both set of samples with high gallium concentration show a good reproducibility. Similar to figure 6.4, the $V_{OC}(t)$ of RbF-treated decreases with a smaller rate than the untreated samples (Fig. C.2(a)). For samples with GGI = 0.83 the doping transients ($N_{A,a}(t)$) of the RbF-treated sample shows a stronger increase than the untreated samples Fig. C.2(b) at the initial phase, which is similar to results in figure 6.8(a). In order to compute the $\Delta V_{OC}(t)$ for an absorber/SL/window, the interface recombination velocity (S_p) was set to 10^7 cm/s for both treated and untreated cells and the doping density of the window layer was 4×10^{17} cm^{-3}. With the known doping transients, $N_{A,a}(t)$ from figure 6.8(a) and the given parameters, the $\Delta V_{OC}(t)$ transients of both cells were
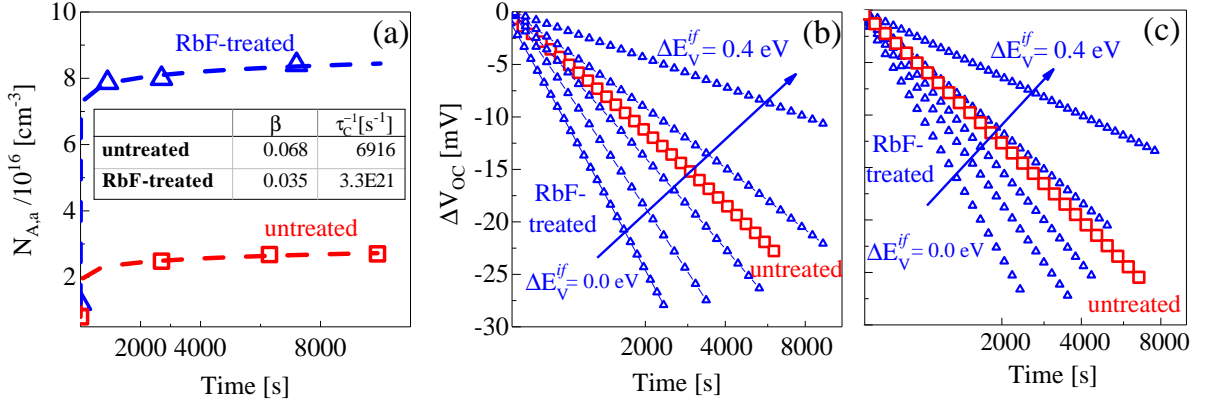
Figure 6.8.: The correlation between the doping density and $\Delta V_{OC}(t)$ for samples with the GGI = 0.75. (a) Measured doping transients for RbF-treated and untreated samples, (b) calculated $\Delta V_{OC}(t)$ considering an absorber/SL/window structure, where for the untreated sample the $\Delta E_V^{if} = 0$, (c) calculated $\Delta V_{OC}(t)$ considering an absorber/SL/buffer/window structure. The slope of the $\Delta V_{OC}(t)$ reduces in a slower rate when the valence band at the hetero-interface is shifted downward.

calculated according to equation 6.2.9 and are shown in figure 6.8(b).

The calculated ΔV_{OC} of the untreated sample (red squares) in figure 6.8(b) is in a good agreement with the measurement data in figure 6.4(b) by considering that $\Delta E_V^{if} = 0$. Thus, the assumption that the bandgap value of the absorber and the surface layer are the same for the untreated sample, confirms the previous model presented in section 5.3. The calculated ΔV_{OC} of the RbF-treated sample in figure 6.8(b) decreases with a faster rate than the untreated sample when $\Delta E_V^{if} = 0$, which is in disagreement with the experimental data in figure 6.4(b). Therefore, considering a simple absorber/window fails to describe the $\Delta V_{OC}(t)$ of the RbF-treated sample. However, if the ΔE_V^{if} of the alkali-treated sample increases to 0.4 eV, the slope of $\Delta V_{OC}(t)$ will reduce in a slower rate than the untreated sample and if ΔE_V^{if} increases above 0.45 eV, the calculated $\Delta V_{OC}(t)$ will show a positive slope.

In figure 6.8(c), the $\Delta V_{OC}(t)$ is calculated for the absorber/SL/buffer/window hetero-structure. The calculated $\Delta V_{OC}(t)$ of the untreated sample again shows a good agreement with measurement data in figure 6.4(b) provided that ΔE_V^{if} is equal to zero. For RbF-treated sample, the same behavior as in figure 6.8(b) can be observed. Considering that $\Delta E_V^{if} = 0$, then the ΔV_{OC} of the RbF-treated reduces sharply compared to the untreated sample, which is not in agreement with the data presented in figure 6.4(b). But if the valence band edge of the SL is shifted downward for the alkali-treated sample, then $\Delta V_{OC}(t)$ will reduce in a slower pace than the untreated sample. For ΔE_V^{if} above 0.45 eV, the $\Delta V_{OC}(t)$ shows a positive slope, which is also similar to the absorber/SL/window model in figure 6.8(b).

The figures 6.8(b - c) suggest that RbF- and CsF-treatment are the most effective alkalis

to widen the bandgap at the interface, while KF-treatment has a lower impact on the bandgap widening. This also explains why the RbF-treated samples had the largest gain in V_{OC} compared to other alkali-treated samples in (see Fig. 5.1). Further, figures 6.8(b - c) indicate that in order to overcome the interface recombination it would suffice to lower the valence band edge about 0.5 eV, which means that the bandgap at the surface must be about 2 eV. In section 5.4, it was assumed that for the alkali-treated samples the bandgap value of the surface-layer is 2.7 eV, to simulate the double-diode behavior in the first quadrant. These assumption was based on the previous findings [10, 11]. Therefore, there is a discrepancy between both models.

In the following the changes of $\Delta V_{OC}(t)$ for models presented in figures 5.8 and 5.11 are examined. In figure 6.8(a), it was shown that the doping density of the untreated sample increases by a factor of 2 beyond its initial value under red illumination. Therefore the JV-curves for the doping densities 1×10^{16}cm^{-3} and 2×10^{16} cm^{-3} were simulated for the model presented in figure 5.8. The doping density of the RbF-treated sample increases by a factor of 6 above its initial value (figure 6.8(a)). Therefore the JV-curves for the doping densities 1×10^{16}cm^{-3} and 6×10^{16} cm^{-3} were computed for the model presented in figure 5.11. The $V_{OC}(N_{A,a})$ of the resulting JV-curves for the RbF-treated and untreated samples are given in Table 6.1. In the last column the $\Delta V'_{OC}$ is given which is the difference between $V_{OC}(N_{A,a})$ and $V_{OC}(1 \times 10^{16})$.

As can be seen in Table 6.1, the V_{OC} decreases for both cases as the doping density

Table 6.1.: Simulation results of doping density on V_{OC} for models presented in figures 5.8 and 5.11.

	figure	$V_{OC}(1 \times 10^{16})$	$V_{OC}(2 \times 10^{16})$	$V_{OC}(6 \times 10^{16})$	$\Delta V'_{OC}$
wo PDT	5.8	637	621		-18
RbF-PDT	5.11	872		867	-5

increases. Thus both models are limited by interface recombination. The $\Delta V'_{OC}$ versus the doping density is plotted in figure 6.9. As can be seen in figure 6.9, the $\Delta V'_{OC}$ of the
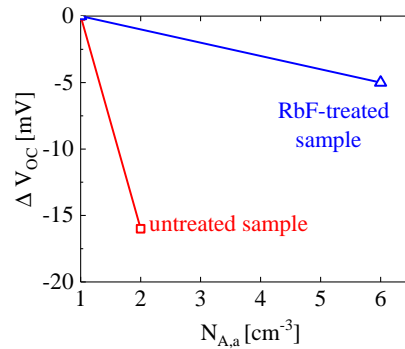
Figure 6.9: Influence of doping density on $\Delta V'_{OC}$ for models in figures 5.8 and 5.11.

RbF-treated sample decreases in a slower pace than the untreated sample, although the doping density is larger. Therefore the models presented in figures 5.8 and 5.11 can explain

the decrease of the $\Delta V_{\text{OC}}(t)$ slope, provided that interface states between the CIGSe and SL exists for the figure 5.11 exist.

Finally it has to be reminded that there are also other solutions to slow down the decrease of the $\Delta V_{\text{OC}}(t)$. For instance it is possible to reduce the recombination velocity of the holes (S_{p}). In this way the recombination rate at the interface reduces and the open-circuit voltage decreases in a slower rate. The influence of S_{p} on $\Delta V_{\text{OC}}(t)$ for RbF-treated sample is shown in figure 6.10(a -b). The $\Delta V_{\text{OC}}(t)$ is calculated for S_{p} between $10^7 - 10^3$ cm/s and considering $\Delta E_{\text{V}}^{if} = 0$. For a comparison the $\Delta V_{\text{OC}}(t)$ of the untreated sample is shown in figure 6.10 with red open squares. It can be seen that reducing the hole velocity has a small impact on $\Delta V_{\text{OC}}(t)$. Even for $S_{\text{p}} = 10^3$ cm/s, the $\Delta V_{\text{OC}}(t)$ reduces faster than the untreated sample. Thus, reducing the slope velocity cannot explain $\Delta V_{\text{OC}}(t)$ of RbF-treated samples.

Another solution, is to increase the degree of inversion. This can be accomplished by
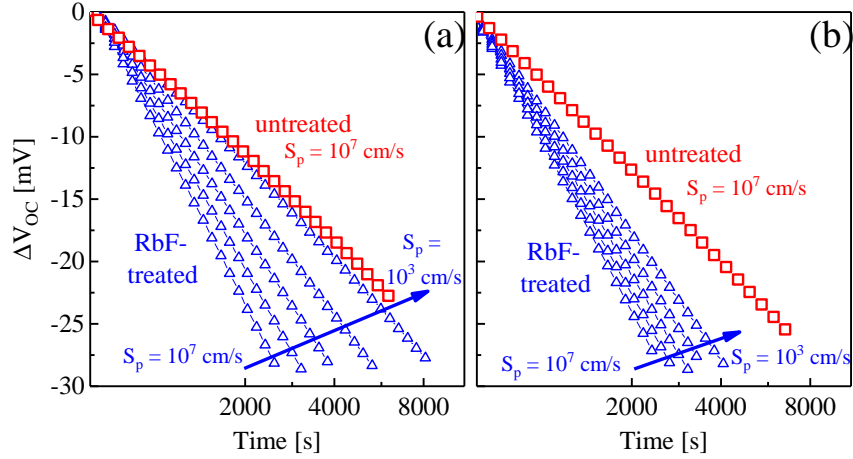
Figure 6.10.: The influence of S_{p} on $\Delta V_{\text{OC}}(t)$ for RbF-treated sample with $\Delta E_{\text{V}}^{if} = 0$. (a) Calculated $\Delta V_{\text{OC}}(t)$ for an absorber/SL/window structure, (b) Calculated $\Delta V_{\text{OC}}(t)$ for an absorber/SL/buffer/window structure. The $\Delta V_{\text{OC}}(t)$ is calculated for S_{p} between $10^7 - 10^3$ cm/s.

introduction of high density of interface defects [34] or increasing the doping density of window layer [4]. Increasing the inversion degree leads to a slow changing of the $\Delta V_{\text{OC}}(t)$ but it fails to explain the double-diode behavior in the first quadrant.

6.4. Concluding remarks

The aim of this chapter was to identify the dominant recombination path by measuring the open-circuit voltage transients upon red light illumination. The positive slope of the V_{OC}-transients indicated that the low-gallium content CIGSe cells are limited by bulk recombination. All devices with high-gallium concentration exhibited a negative $V_{\text{OC}}(t)$ slopes indicating dominant recombination at the interface.

In order to explain the different $V_{OC}(t)$ slopes, equations for V_{OC}-transients for different recombination paths were derived. It was shown that cells limited by QNR and SCR are described by the same $V_{OC}(t)$ relation (see equations 6.2.5 and 6.2.7). Therefore, from the V_{OC}-transients, it is not possible to diagnose the recombination path from the SCR to QNR.

The calculation of $\Delta V_{OC}(t)$ for interface recombination, indicated that the doping density is not the only quantity influencing the $\Delta V_{OC}(t)$-slope, but parameters such as the interface recombination velocity (S_p), and the position of the valence band at the interface needs to be taken into account.

By measuring the doping transient and recalculation of the V_{OC}-transients for the untreated sample a good agreement with the measurement data was achieved. But the $\Delta V_{OC}(t)$ of the RbF-treated sample could not be described properly by the deep valence band edge of the surface layer.

7. Influence of alternative substrates on CIGSe performance

In chapter 4, it has been shown that the deposition of wide-gap CIGSe absorbers on Na-containing substrates with the multi-stage process produces a pronounced gradient that deteriorates the electronic properties. One strategy to prevent the formation of the pronounced gallium gradient was to modify the deposition process to improve the electronic parameters. In this chapter, two other strategies are adopted to flatten the gallium gradient of wide-gap CIGSe absorbers. In the first section, the CIGSe absorber is grown in the absence of sodium (sodium-free substrates). The absence of sodium during growth of the absorber facilitates the inter-diffusion of the chemical elements and leads to a smooth gallium gradient [52, 123]. But sodium is mandatory to achieve a high solar cell efficiency with CIGSe. Thus, NaF post-deposition treatment is used to incorporate sodium into the sodium-free grown CIGSe absorber. This method allows controlling the sodium amount and at the same time does not hamper the inter-diffusion of the gallium and indium [53]. In effect, detrimental gallium gradients can be avoided. In the second section, the wide-gap CIGSe absorber is grown on high-temperature substrates. The increased substrate temperature enhances the inter-diffusion of the gallium and indium and hinders the formation of a pronounced gallium gradient [124].

7.1. The influence of sodium on CIGSe growth: barriers and non-barrier substrate

In this section, the wide-gap CIGSe absorbers were deposited according to the multi-stage process (Fig .3.3) on sodium-free substrate (section 3.1.2). After the absorber growth on sodium-free substrates, first sodium and then potassium was deposited in the presence of a selenium atmosphere. The effect of NaF and KF thicknesses was investigated in a NaF-KF thickness matrix in order to map out possible multiple efficiency maxima. Throughout this section, the term "barrier" sample will be used, due to the barrier layer that exists between SLG and molybdenum that prevents the diffusion of sodium during CIGSe growth.

The "non-barrier" sample is a KF-treated sample from chapter 5 that has the same bandgap value as the barrier sample and is used to evaluate the beneficial/negative effects of the barrier sample. The thickness of the KF-PDT of the non-barrier sample is 6 nm.
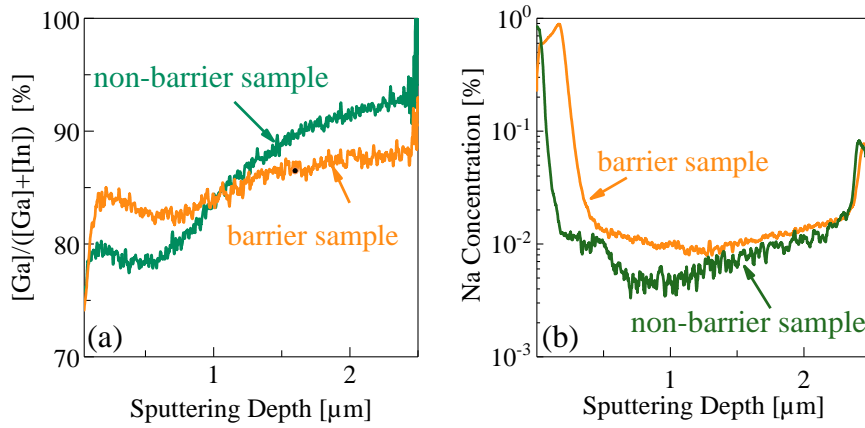
Figure 7.1.: The depth profiles of grown CIGSe absorbers deposited on barrier (with 15 nm NaF and 20 nm KF PDT) and non-barrier substrate (with 6 nm KF PDT), (a) GGI, (b) Na profile. Both CIGSe samples have an integral GGI value of ~ 0.83. The barrier sample is grown according to multi-stage process (recipe (a)) and non-barrier sample is grown according to the modified process (recipe (b)).

The non-barrier sample has been grown according to the modified process (recipe (b)) in order to avoid a detrimental gallium gradient.

7.1.1. Depth profile analysis

The depth profiles of the GGI and the Na concentration of barrier and non-barrier samples are shown in figure 7.1(a - b). The barrier sample was chosen from the matrix based on the highest solar cell performance parameters. The highest performance was achieved for the sample with 15 nm NaF and 20 nm KF-PDT. The GGI profile of the barrier sample has a smooth gradient (Fig. 7.1(a)), and the notch of the sample prepared on a barrier substrate is less deep than the non-barrier sample. For small bandgap CIGSe absorbers, it was also reported that deposition of CIGSe absorber on sodium-free substrates promotes the inter-diffusion of metals and leads to a smooth GGI profile [50, 125]. The small gallium gradient of the barrier sample indicates that the diffusion of the metals is higher compared to the non-barrier sample. It has been suggested that in the absence of sodium a large number of metal vacancies is available that facilitate the interdiffusion of the gallium and indium [125].

The sodium concentration of the barrier sample and the non-barrier sample is compared on a logarithmic scale (Fig. 7.1(b)). For the non-barrier sample, the sodium diffuses from the glass through the absorber and segregates at the surface and the back contact (Fig. 7.1(b)). The segregation of sodium at the surface is a known phenomenon and is also reported for low-gap CIGSe absorbers [126]. The sodium profile of the barrier sample in figure 7.1(b) indicates that although sodium is deposited at a low substrate temperature of 723 K, sodium diffuses through the absorber and shows the same amount of sodium at the back contact as in the case of non-barrier sample.

7.1.2. Solar cell parameters

The solar cell parameters of CIGSe devices on barrier substrates having different thicknesses of NaF and KF are presented as a color-map in figure 7.2. The effect of NaF and KF thicknesses were investigated in a large scale to be certain, that any specific combination of thicknesses that may results in a higher efficiency is not overlooked. The best efficiency for wide-gap CIGSe solar cells was achieved for 15 nm NaF and 20 nm KF post deposition treatment (Fig. 7.2(d)). The combination of these thicknesses is very close to the one of high efficiency small bandgap CIGSe solar cells [37]. Chirilă et al. has reported their high efficient solar cells has been achieved for the thickness of $\sim$ 26 nm NaF and $\sim$ 15 nm KF [37]. Other data for wide bandgap CIGSe do not exist.

The V_{OC}-deficit of different samples is plotted in figure 7.2(a). It can be seen that by keeping the thickness of the KF-PDT by 5 nm and increasing the thickness of Na-PDT, the V_{OC}-deficit increases. Since sodium increases the doping density, from figure 7.2(a) it can be understood that the cells with 5 nm KF-PDT are limited by recombination at the interface. Otherwise, the increase of the doping density must reduce the V_{OC}-deficit for cells dominated by recombination in the QNR and SCR. But samples with low amount of sodium concentration and large thickness of KF-PDT show also a poor V_{OC}. The possible explanation might be that the low amount of sodium cannot effectively passivate the defects. However, there is an optimum of NaF-PDT and KF-PDT thickness that reduces the V_{OC}-deficit to 0.56 V.

The difference between the maximum possible current density and the measured one, ($\Delta J_{SC} = J_{SC}^{max} - J_{SC}^{*}$) is shown in figure 7.2(b). The current density J_{SC}^{*} is derived from integration of the measured EQE over AM1.5G. The maximum possible current density, J_{SC}^{max}, is the integrated EQE over AM1.5G with the assumption that all the incident photons contribute to the current density. In figure 7.2(b), a large loss in the current density for samples with 30 nm NaF and low KF-thicknesses can be observed. Unfortunately, few problems arose as the thickness of the NaF-PDT was increased. Firstly, for NaF-PDT with a thickness above 20 nm (while keeping the thickness of KF-PDT by 5 nm), the excess alkali-PDT of the samples could not be washed away in the chemical bath. This led to the situation that the CdS came in contact with the alkali-PDT and formed a yellow layer on the absorber. In these cases, a large portion of light was lost and the samples were showing a low J_{SC}. Rinsing the samples with distilled water prior to the deposition of the buffer layer was not helping as well.

Another problem with increasing the thickness of NaF-PDT was that the samples were showing a kink at small voltag bias. In figures 7.3(a) and 7.4(b), a slight kink can be observed. This indicates that even for moderate amount of NaF-PDT a barrier for the
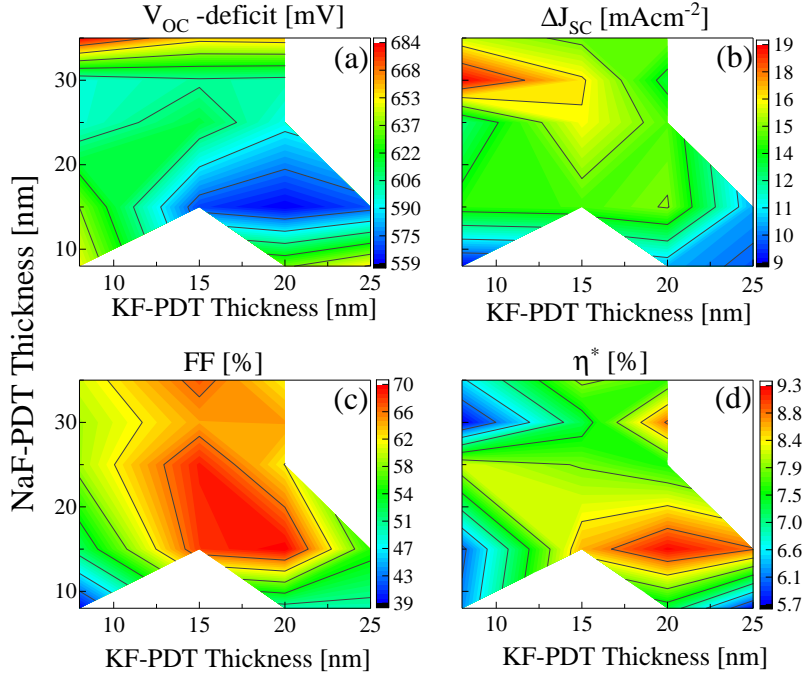
Figure 7.2.: The influence of NaF and KF-PDT thicknesses on the solar cell parameters. All absorbers prepared on barrier substrate according to recipe (a) in figure 3.3. The integral GGI of used absorbers is 0.80 ± 0.05, (a) V_{OC}-deficit is the difference between E_g/q and the measured V_{OC}, (b) ΔJ_{SC} is the difference between the maximum achievable J_{SC}^{max} and the measured J_{SC}^*, (c) FF, (d) η^*. The highest efficiency is achieved for 15 nm NaF and 20 nm KF-PDT.

photo-current is formed. This effect was more pronounced for thick NaF-PDT. The sodium increases the doping density [101], therefore it can be concluded that Na-PDT introduces a p^+-layer at the CIGSe interface and forms a barrier for the photo-generated electrons at the front contact. The kink in the fourth quadrant reduces the J_{SC} because the photo-generated electrons cannot overcome the barrier and recombine [4, 127]. Furthermore, the kink deteriorates the FF [4, 127].

The influence of NaF and KF-PDT thickness variation on the FF is shown in figure 7.2(c). As can be seen in figure 7.2(c), a high FF is achieved for cells whose V_{OC}-deficit is the lowest. This is in agreement with the equation 4.3.10, which states that the FF increases with V_{OC} [4]. The lowest FF is achieved for samples with very low sodium concentration. This low FF is partially related to the high V_{OC}-deficit but it is also related to the sodium concentration [50, 128]. A low sodium concentration reduces the conductivity and thereby the FF [50, 128]. From figure 7.2 it can be seen that the best efficiency is achieved where the highest V_{OC} (smallest V_{OC}-deficit) is obtained.

In figure 7.3, the JV-curves and EQE's of the non-barrier and barrier samples are shown. For these solar cells, an alternative i-ZnO/ZnO:Al with lower resistivity was used which has reduced the V_{OC}. The comparison of the JV-curves in figure 7.3(a) indicates that the V_{OC} and J_{SC} of the barrier sample is lower than of the non-barrier sample, this might originate from the small GGI back gradient [80, 86]. Dullweber et al. have suggested that

a back gradient reduces the recombination at the back contact and increases the V_{OC} [80]. Gloeckler has shown that the back grading improves the J_{SC} slightly [86]. In figure 7.3(b), the EQE signals of the corresponding JV-curves are given. It can be seen that the EQE signal of the non-barrier sample with the modified deposition recipe shows a gain in the long wavelength region. In chapter 4 it was shown that the appropriate gradient profile improves the collection function and as a result the J_{SC}. Since the V_{OC} and J_{SC} of the barrier sample is lower than the non-barrier sample, the final conversion efficiency of the barrier sample is lower than of the non-barrier sample.
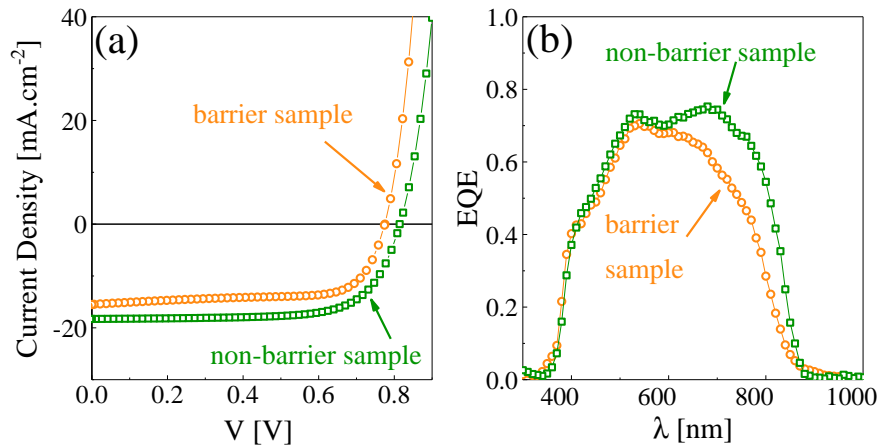
Figure 7.3.: Comparison of solar cell properties of CIGSe grown on barrier and non-barrier substrates (a) JV-curves and (b) EQE. The non-barrier sample was grown with the modified deposition recipe with 6 nm KF-PDT (recipe (b)). The barrier sample has 15 nm NaF and 20 nm KF-PDT. The GGI and Na profiles of these samples are given in figure 7.1.

Therefore, from figure 7.3 it can be concluded that sodium must be present during the growth of wide-gap CIGSe absorbers in oder to achieve high efficiency. This result is very similar to the previous report that the highest efficiency of low-gap CIGSe cells can be achieved on SLG glass [50].

7.1.3. Temperature dependent JV-curves on barrier sample

It has been reported, that the post-deposition treatment of heavy alkalis with small bandgap CIGSe absorbers grown on sodium-free substrates influences the back barrier height or increases the band offset at the absorber/buffer interface [101, 107]. This was a motivation to examine the temperature dependent $JV(T)$-curves of barrier samples (Fig. 7.4). Therefore, the barrier sample with the highest efficiency, 15 nm NaF-PDT and 20 nm KF-PDT was further examined.

As can be seen in figure 7.4(a - b), the $JV(T)$-curves of the barrier sample does not show any sign of rollover. Thus it can be concluded that the barrier height at the back contact (Mo/CIGSe) is not influenced or the conduction band offset at the hetero-interface is not changed. Similar to the results presented in section 5.2, there is a crossover between the
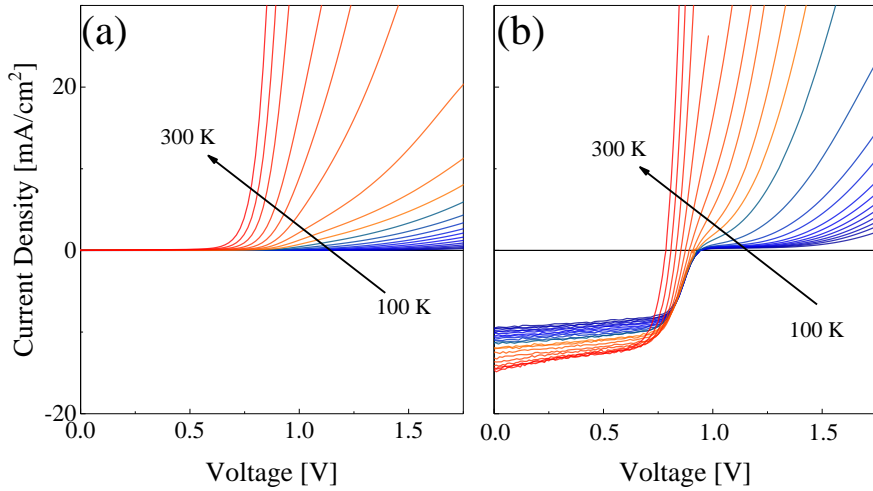
Figure 7.4.: Temperature dependent JV-curves of the barrier sample with 15 nm NaF-PDT and 20 nm KF-PDT. The results are similar as presented for the KF-treated sample in figure 5.5(b).

dark and illuminated JV-curves. As shown in section 5.3, the crossover might originate from the deep acceptor states in the buffer layer (section 5.3.1) or a p^+-layer between the CIGSe and buffer layer (section 5.3.2).

The JV-curves under white-light illumination show a double-diode behavior in the first quadrant at low temperature, similar to results of KF-treated sample in figure 5.5(b). As shown in chapter 5, a double-diode behavior in the first quadrant is an indication of a deep valence band edge at the hetero-interface. However, there is a slight difference between the results in figures 7.4(b) and 5.5(b - d). The current density of the barrier sample exhibits a slight kink at small voltage bias. For samples with heavy alkali-treatment no barrier for the photo-current barrier was observed (Fig. 5.5(b - d)). This implies that the effect of NaF-PDT is different from other heavy alkalis. The NaF-PDT forms a p^+-layer next to the CIGSe absorber and shifts the conduction band upwards. This is also in agreement with previous findings that sodium increases the hole density [50, 101, 128]. Furthermore, the J_{SC} is temperature dependent and increases with the temperature, this phenomenon is similar to the results in figure 5.5(b - d). As mentioned in section 5.4, this effect can be simulated with a shallow defect state below the conduction band or considering temperature-dependent electron mobility.

In order to simulate the $JV(T)$-curves of figure 7.4, a p^+-layer between the CIGSe and the buffer layer is programmed. The valence band of the p^+-layer is shifted downward and aligned with the buffer layer to simulate the double-diode in the first quadrant (E_g (p^+-layer) = 2.7 eV). The p^+-layer is also simultaneously responsible for the crossover between the light and dark JV curves (see section 5.3.2). Finally, a shallow donor state below the conduction band was added to to simulate the $J_{SC}(T)$ (see Table. A.4).

The simulation results in figure 7.5(a - c) indicate that the deep valence band edge of the p^+-layer can bring the double-diode behavior at low temperatures. Furthermore, due
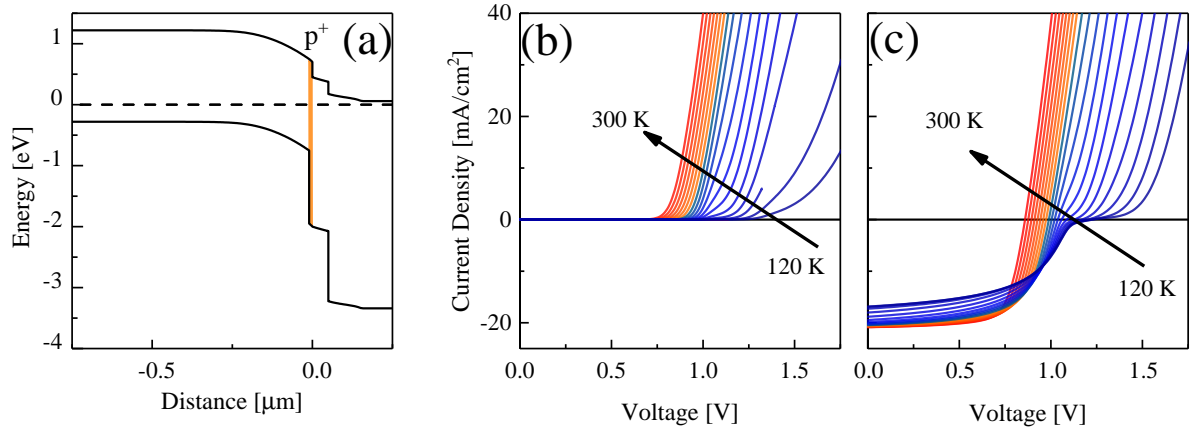
Figure 7.5.: Simulation results of lowering the valence band edge of the p^+-layer, (a) band diagram in equilibrium, (b) dark, and (c) illuminated $JV(T)$ evolution from T = 120 – 300 K in 10 K steps. Information regarding the parameters can be found in Table. A.4.

to the p^+-layer the crossover between the dark and light JV curves also exist. Thus the double-diode behavior and the crossover could be simulated with the addition of the p^+-layer between the CIGSe and CdS layer. Finally the $J_{SC}(T)$ increases with the temperature, which is also consistent with the measurement data in figure 7.4.

7.1.4. Concluding remarks

In this section, the influence of sodium-free substrates on the electronic properties of wide-gap CIGSe cells was examined. The results indicate that:

• The absence of sodium promotes the inter-diffusion of the indium and gallium. As a result a smooth gallium gradient is developed throughout the absorber.

• Although sodium is introduced at low substrates temperature (723 K), the depth profile analysis indicates that sodium providing by PDT is able to diffuse to the back contact.

• Due to the smooth gallium gradient of the barrier sample, the EQE signal of the barrier sample was lower than of the non-barrier sample in the long wavelength region. So with barrier the gradient becomes too small.

• The V_{OC} and J_{SC} of the barrier sample are lower than in the case of the non-barrier sample. Despite many variations of the thickness of NaF and KF, the samples grown on the non-barrier substrate with the modified recipe did show a superior efficiency. The plau-

sible explanations are different grain boundary properties and different band gap grading which influences the collection function and impedes recombination at the back contact [50].

- The NaF-PDT induces a barrier for the photo-current by shifting the conduction band upward. Thus the influence of NaF-PDT on the CIGSe cell is different from heavier alkalis.

- Temperature dependent JV-curves of the sample prepared on barrier substrate show a double-diode behavior in the first quadrant at low temperatures which hints to a deep valence band edge at the interface. The results are similar to the KF-treated sample in chapter 5.

7.2. The growth of CIGSe at elevated temperature

In 2014, it has been shown that growing the wide-gap CIGSe absorber at higher substrate temperatures increases the open-circuit voltage and consequently the efficiency [2]. At that time the influence of alkali-PDT on the electronic properties was unknown. Therefore, in the following high-temperature substrates are used (High-T sample) and the impact of RbF-PDT on wide-gap CIGSe cells is investigated, since the highest gain in V_{OC} was achieved for samples treated with this heavy alkali element (Fig. 5.1).

7.2.1. Deposition process

The wide-gap CIGSe absorbers were grown in the multi-stage process (section 3.3.2-recipe (a)), but the substrate temperature was increased to 948 K in the second and third stage. After the deposition of the CIGSe absorber, the sample was cooled down to 723 K and was treated with 25 nm RbF in the presence of selenium. The absorbers were finished to cells as explained in chapter 3. As a reference sample, a RbF-treated device from chapter 5 with the same bandgap value grown by modified process was chosen to evaluate the results of High-T sample. In the following section the term "SLG sample" is used for the reference sample to distinguish the sample from the High-T sample.

7.2.2. Depth profile analysis

In figure 7.6(a - b), the depth profiles of the High-T sample and the SLG sample are illustrated. The High-T sample shows a very small GGI gradient (Fig. 7.6(a)), this indicates that the high deposition temperature allows the gallium and indium atoms to better inter-diffuse. The small gradient in figure 7.6 correlates fairly well with the previous findings [124, 129].
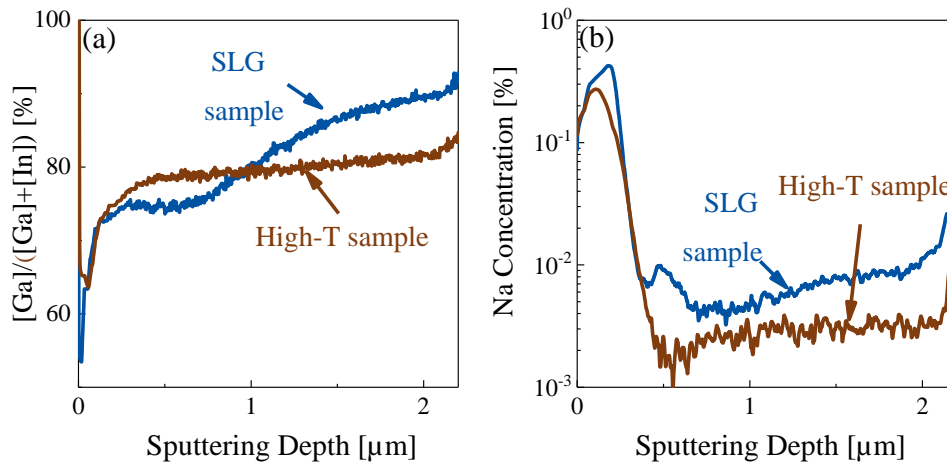
Figure 7.6.: Depth profiles from GDOES measurement of the High-T and SLG sample, (a) GGI, (b) sodium profile. The High-T sample is grown in the multi-stage process (recipe (a)) and the SLG sample is grown by the modified recipe (recipe (b)). Both samples have received a RbF-PDT with thickness 25 nm.

In figure 7.6(b), the sodium distribution is illustrated on a logarithmic scale. As can be seen in figure 7.6(b), the sodium concentration in the High-T sample is lower than in the SLG sample. As shown by Bertram et al. the low sodium concentration does not mean that the substrate itself provides less sodium, the reason is that sodium evaporates out of the sample at high substrate temperature and therefore less sodium can be detected [129].

7.2.3. Electronic properties

The JV-curves of the CIGSe solar cells deposited with two different substrate temperatures are shown in figure 7.7(a). The results indicate that the V_{OC} of the High-T sample increases by 40 mV relative to the SLG sample and reaches 880 mV. Such high V_{OC} value has never been reported for wide-gap CIGSe cells with the E_g of 1.4 eV. The highest V_{OC} that was achieved on this High-T substrates is about 815 mV [2]. Therefore, growing the CIGSe absorber on the High-T substrate and using alkali-PDT is an effective method to further reduce the V_{OC}-deficit to 0.52 V. The TRPL decay curve of a High-T sample and SLG sample is shown in figure 7.1(b). The High-T sample shows a longer decay time compared to the SLG sample, which might hint to a higher V_{OC}.

The J_{SC} of the High-T sample shows a slight increase relative to the SLG sample (Fig. 7.7(a - b)). Hence it can be understood that the high temperature has a negligible influence on the J_{SC}. But if the EQE signal of the High-T sample is compared to the barrier sample in figure 7.3(b) then a gain in the long-wavelength region is observed. This is interesting, because the field from the gradient is absent for the High-T sample, though an increase in the EQE signal in long wavelength region is obtained. This implies that growing the wide-gap CIGSe absorber at elevated temperature improves the bulk properties of the absorber. However, an increased bulk lifetime cannot be observed for the High-T sample

in figure 7.1(b).

Despite the gain in V_{OC} and J_{SC}, a lower FF than of the SLG sample was attained for the High-T sample (Fig 7.7 (a)), and consequently a lower efficiency for the High-T sample was achieved (Fig 7.7(d)). As mentioned earlier, the low FF is correlated to the V_{OC} and sodium concentration. However, for this specific sample the V_{OC} is very high.Therefore, it might be that the low FF originates from the sodium concentration. Granath et al. have reported that as the sodium concentration of CIGSe absorbers decreases, the conductivity reduces and detoriates the FF of the cell [130]. Rudmann suggests that sodium removes the defects states and reduces the resistivity of the CIGSe film [50].
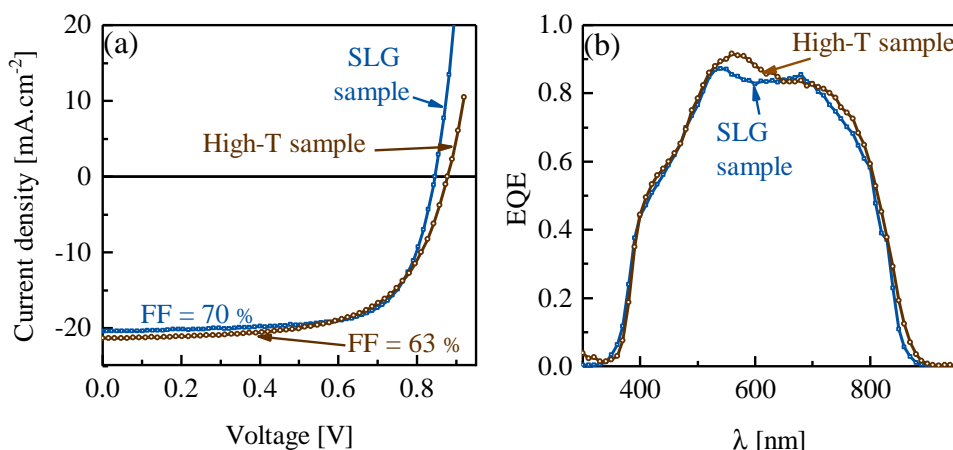
Figure 7.7.: The comparison of the solar cell properties between High-T and SLG sample, (a) JV-curves, (b) EQE signal. Both solar cells have a bandgap value of 1.4 eV. The V_{OC} of the High-T sample is 880 mV.

In order to examine the effect of sodium on electronic properties of the High-T samples, sodium was introduced to the CIGSe absorber as a precursor. In the previous section it was shown that the presence of sodium during the growth is beneficial, therefore NaF was deposited onto the molybdenum in the vacuum chamber at room temperature. The thickness of the deposited sodium was 8 nm. In the following, the sample will be referred as "High-T+NaF-pre". In order to eliminate any ambiguity arising from small deposition variations, another substrate without NaF-precursor was inserted into the chamber and both CIGSe absorbers were grown in the same run.

One of the concerns was, if the addition of sodium as a precursor hinders the inter-diffusion of the materials and creates a detrimental gradient in the absorber as shown in figure 4.1. Figure 7.8(a) shows that although sodium was present during the process, the high substrate temperature avoids the formation of the pronounced gradient similar to figure 4.1 and just a negligible back gradient can be observed.

The solar cell parameters of the new set of samples are shown in figure 7.9. A sample grown on a soda-lime glass with 25 nm RbF-PDT is also shown as a reference in figure 7.9. Similar to the previous case, the High-T sample shows the highest V_{OC} and J_{SC}^*, and simultaneously the lowest FF and η^*. The J_{SC}^* here is the integration of the measured
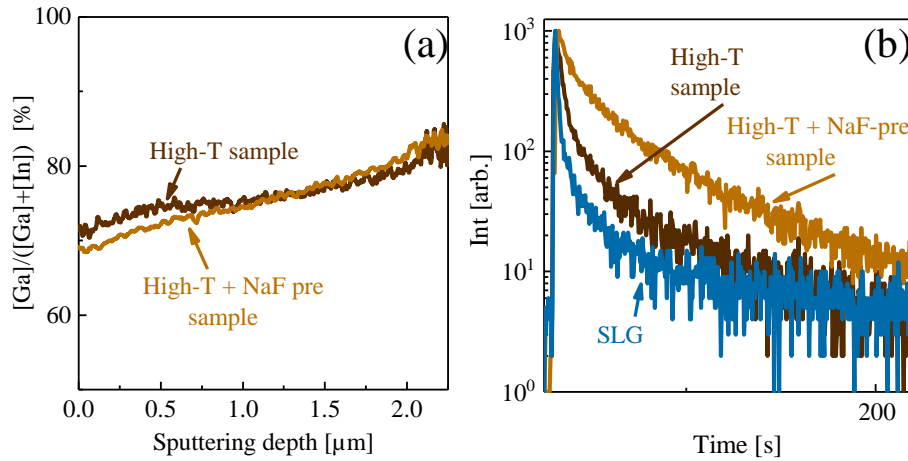
Figure 7.8.: The influence of the NaF-precursor on the (a) GGI gradient, (b) TRPL transients. The High-T + NaF-pre has received 8 nm NaF precursor prior the CIGSe growth. The absorbers were grown according to the multi-stage process (recipe (a)) and have received 25 nm RbF-PDT. The samples have the final CGI of 0.85. The TRPL signal of a RbF-treated sample grown on soda lime glass is shown in blue.

EQE over AM1.5G, and the efficiency (η^*) is also calculated based on the integrated J_{SC}^* (Eq. 2.4.7).

In figure 7.9(a), it can be seen that the introduction of sodium has reduced the V_{OC}, compared to the High-T sample. But still the V_{OC} is higher than of the SLG sample. If the TRPL transients of the High-T sample and High-T+NaF-pre are compared in figure 7.8(b), it can be observed that the TRPL-transient of High-T+ NaF-pre sample shows a longer decay curve than the High-T sample. This implies that, for the High-T+ NaF-pre sample a higher V_{OC} is expected, but the V_{OC} of the High-T+ NaF-pre sample is about 20 mV lower than the High-T sample. One explanation for the decrease of the V_{OC} might be that sodium has increased the doping density and for wide-gap CIGSe cells that are limited by interface recombination, an increased doping density is accompanied with an increased recombination rate at the interface (see chapter 6). The figure 7.9(c) indicates that the FF of the High-T+Na-pre sample is increased about 7% relative to the High-T sample. The increased FF improves the efficiency and yields a superior performance than the SLG solar cell. Comparing the results of High-T+Na-pre with the sample from reference [2] reveals that despite the higher V_{OC} than from the reference [2], the final conversion efficiency is lower, because the current density is lower compared to the reference [2]. This is due to the non-optimized window layer in terms of transparency and conductivity employed in this thesis.

7.2.4. Concluding remarks

In section 7.2, the influence of substrates that can tolerate higher temperatures than the standard soda lime glasses was examined. The comparison of the High-T substrates to
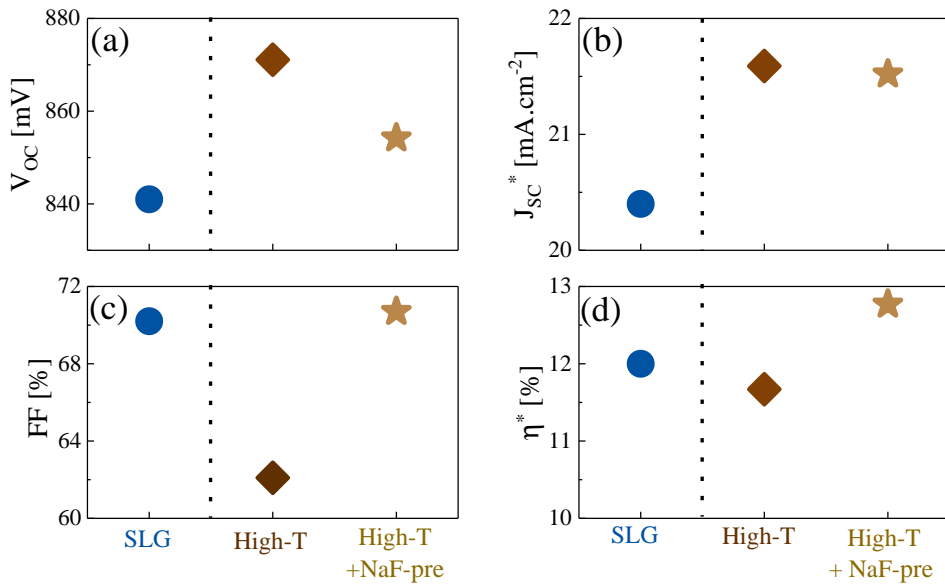
Figure 7.9.: The solar cell parameters of SLG sample (●), High-T sample (◆), High-T+ NaF-pre sample (★). The CIGSe cells have the bandgap value of 1.41 eV.

the soda-lime glasses indicates that:

- The increased substrate temperature promotes the inter-diffusion of elements and leads to a uniform GGI gradient.

- The high substrate temperature results in a loss of sodium. Therefore the CIGSe grown on High-T substrates have a lower sodium content compared to the SLG sample, which deteriorates the FF.

- Growing the CIGSe absorber on elevated substrate temperature improves the V_{OC} and J_{SC}.

- Introduction of sodium as a precursor on high-temperature samples increases the FF and leads to a superior performance in comparison to the SLG glasses.

Although the efficiency of the wide-gap CIGSe cells improves by the use of this specific substrate and treatment of heavy alkalis, the efficiency of the wide-gap CIGSe cells is still very low.

8. Closing remarks and outlook

The aim of this work was to study the influence of post-deposition treatment with heavy alkalis on wide bandgap $Cu(In,Ga)Se_2$ cells. In order to approach this goal, first the influence of the gallium gradient on solar cell parameters of wide-gap CIGSe cells was examined. It turned out that the high-gallium content CIGSe absorbers grown by the multi-stage process on SLG have a more pronounced gradient profile compared to low gallium-content CIGSe absorbers. The pronounced gallium gradient diminishes the collection probability and reduces the J_{SC}. Further, it was shown that the FF is linearly dependent on the collection efficiency, which in turn is also influenced by the gallium gradient. By modification of the deposition process of wide bandgap CIGSe absorbers a great improvement in the J_{SC} and FF was achieved. The presence of sodium during growth and the substrate temperature also influence the inter-diffusion of elements which was investigated in chapter 7.

It has been shown that the post-deposition treatment with heavy alkali elements (KF, RbF and CsF) increases the V_{OC} of CIGSe solar cells with different gallium concentration. But the highest gain of the V_{OC} upon alkali-treatment was achieved for bandgap value of 1.35 eV. Consequently, with the improvement of the V_{OC}, an increase in the FF and the efficiency was observed.

In order to understand how the post-deposition treatment with heavy alkalis does increase the V_{OC}, the electronic charge transport of wide-gap CIGSe solar cells was investigated using temperature dependent current–voltage analysis. Thereby, a variety of features were encountered, not all being exclusive for alkali-treated devices. The alkali-treated and untreated CIGSe cells have in common that a crossover between the light and dark current-voltage curves exist. In literature, two main diode models are suggested to explain the crossover:

- High density of acceptor states in the buffer layer,

- Addition of p^+-layer between CIGSe and CdS.

Numerical simulations have shown that in order to bring out the crossover by defect states in CdS, acceptor states with asymmetrical capture cross sections $\sigma_p \gg \sigma_n$ is required. In the second model, a highly-doped p^+-layer between wide-gap CIGSe and CdS is employed.

This p^+-layer shifts the conduction band upward, which removes the inversion at the surface and induces a large barrier for the photo-current [4]. In order to prevent the formation of a photo-current barrier, a high density of donor states at the interface of the p^+-layer and CdS was required to increase the inversion. As shown in chapter 5, the p^+-layer was able to simulate the crossover between the light and dark JV-curves of wide-gap CIGSe cells.

Besides the crossover, the alkali-treated wide-gap CIGSe cells have demonstrated the following phenomena:

- A double-diode behavior of the JV-curves at low temperatures,

- Saturation of the open-circuit voltage towards low temperatures,

- Temperature dependency of the short circuit current density (J_{SC}).

Simulations have revealed that a barrier for the diode-current leads to a double-diode behavior in the first quadrant of the JV-curve. The barrier is formed by the band offset between CdS and a new layer at the CIGSe/CdS hetero-interface with the property of a low-lying valence band edge. In agreement with the literature [10, 12, 46], this new layer is assigned to a K(In,Ga)Se$_2$ phase.

The saturated open-circuit voltage of alkali-treated samples at low temperature required an explanation different from the previously reported cases employing a barrier at the back contact [108], since here no rollover was observed for the JV curves. It was shown that the saturation of the V_{OC} at low temperature and the double-diode behavior have the same origin and both arise from the deep valence band edge of the surface layer at the hetero-interface.

Despite the reduced recombination rate at the interface of the alkali-treated wide-gap CIGSe solar cells, the measurement of time-dependent V_{OC}-transients indicated that the dominant recombination remains at the interface. Then, relations for the V_{OC}-transients were derived to explain the slopes of the V_{OC}. It was shown that the V_{OC}-transients of narrow bandgap CIGSe cells which are limited by recombination in the QNR or the SCR are solely dependent on the transients of the doping density. Further, it was shown that the V_{OC}-transient of wide-gap CIGSe cells which are limited by interface recombination depends on the doping density of the absorber and to a large extent on the valence band edge position of the surface layer at the hetero-interface. The calculation of $V_{OC}(t)$ from the measured doping transients for the untreated sample has shown a good agreement to the measurement data. But for RbF-treated, no appropriate model was found to describe the ΔV_{OC}.

Several incorporation techniques for sodium were examined, and the conclusion was that

sodium must be present during the growth in order to improve the efficiency of wide-gap CIGSe cells. Further, it was shown that the NaF-PDT induces a barrier for the photo-current and its effect is different than of the heavy alkalis. The deposition of CIGSe with elevated substrate temperature improved the V_{OC} and the J_{SC} to a large extent. By the use of the alkali-PDT and the high-T substrates the highest reported V_{OC} for CIGSe cells with the bandgap value of 1.4 eV was achieved.

Despite the great improvement in the V_{OC} and efficiency of wide-gap CIGSe cells, and better understanding on the effect of alkali-PDT on wide-gap CIGSe cells, several problems were not solved in this thesis:

• The temperature dependency of the short-circuit current density of the alkali-treated samples was simulated with a shallow defect below the conduction band in the bulk of the absorber. However, it is probable that the $J_{SC}(T)$ is related to a modification at the CIGSe/CdS hetero-interface, same as the V_{OC}-saturation at low temperature. Therefore, more in-depth investigations are required to find the origin of this phenomenon.

• In chapters 5 and 6, it was shown that the alkali-treated wide-gap CIGSe absorbers have a new surface layer that shifts the valence band edge downward. There are many reports indicating that the alkalis widen the bandgap of low-gap CIGSe absorbers, but no measurements are performed on wide bandgap CIGSe absorbers to confirm the existence of a new surface layer.

• Regarding the unfavorable band offset between the CIGSe/CdS, more investigations on an alternative emitter with an appropriate deposition method are suggested. For instance, the Zn(Sn,O) buffer layer might be a promising candidate to substitute the CdS buffer layer for wide-gap CIGSe absorber.

A. Simulation parameters

Parameter selection for simulation of the crossover

Table A.1.: Summary of the chosen parameter for simulation of the crossover in Fig. 5.8. For simulation of the crossover, high defect density of acceptors for CdS was considered.

	CIGSe	CdS	i-ZnO	Al:ZnO
Thickness [μm]	2.475	0.05	0.1	0.3
ϵ	$12\epsilon_0$	$10\epsilon_0$	$9\epsilon_0$	$9\epsilon_0$
E_g [eV]	1.5	2.45	3.4	3.4
χ [eV]	4.05	4.3	4.5	4.5
$N_\mathrm{A/D}$ [cm^{-3}]	1×10^{16}	5×10^{18}	1.01×10^{18}	1×10^{18}
μ_e [cm^2/Vs]	0.5	5	20	20
μ_h [cm^2/Vs]	0.2	0.2	20	20
N_C [cm^{-3}]	2×10^{18}	2×10^{18}	4×10^{18}	4×10^{18}
N_V [cm^{-3}]	1.5×10^{19}	1.5×10^{19}	1×10^{19}	1×10^{19}
Midgap Defect	Donor	Acceptor	Acceptor	Acceptor
	Single	Single	Single	Single
N_t[cm^{-3}]	5×10^{13}	4.999×10^{18}	1×10^{18}	1×10^{16}
σ_n[cm^2]	1×10^{-12}	1×10^{-17}	1×10^{-15}	1×10^{-15}
σ_p[cm^2]	5×10^{-13}	1×10^{-12}	1×10^{-12}	1×10^{-12}
Interface States	**CIGSe/CdS**			
Defect	Donor,Single			
N_t[cm^2]	2×10^{11}			
E_t[eV]	0.4 eV below lowest E$_\mathrm{C}$			
σ_n[cm^2]	1×10^{-12}			
σ_p[cm^2]	1×10^{-12}			

Table A.2.: Summary of the chosen parameter for simulation of the crossover in Fig. 5.10. A highly doped thin layer (p^+-layer) was added between CIGSe and CdS to simulate the crossover. In order to have an inversion, high density of donor states was added at the interface of the p^+-layer and CdS.

	CIGSe	p^+	**CdS**	**i-ZnO**	**Al:ZnO**
Thickness [μm]	2.475	0.01	0.05	0.1	0.3
ϵ	$12\epsilon_0$	$12\epsilon_0$	$10\epsilon_0$	$9\epsilon_0$	$9\epsilon_0$
E_g [eV]	1.5	1.50	2.45	3.4	3.4
χ [eV]	4.05	4.05	4.3	4.5	4.5
$N_{A/D}$ [cm^{-3}]	1×10^{16}	1.5×10^{17}	5×10^{15}	1.01×10^{18}	1×10^{18}
μ_e [cm^2/Vs]	3	3	5	20	20
μ_h [cm^2/Vs]	0.2	0.2	0.2	20	20
N_C [cm^{-3}]	2×10^{18}	2×10^{18}	2×10^{18}	4×10^{18}	4×10^{18}
N_V [cm^{-3}]	1.5×10^{19}	1.5×10^{19}	1.5×10^{19}	1×10^{19}	1×10^{19}
Midgap Defect	Donor	Donor	Acceptor	Acceptor	Acceptor
	Single	Single	Single	Single	Single
N_t [cm^{-3}]	6×10^{14}	6×10^{14}	$4.\times10^{15}$	1×10^{18}	1×10^{16}
σ_n [cm^2]	1×10^{-12}	1×10^{-12}	1×10^{-15}	1×10^{-15}	1×10^{-15}
σ_p [cm^2]	1×10^{-12}	1×10^{-12}	1×10^{-13}	1×10^{-12}	1×10^{-12}
Interface States	p^+/**CdS**				
Defect	Donor, Single				
N_t [cm^2]	1×10^{13}				
E_t [eV]	0.65 eV below lowest E_C				
σ_n [cm^2]	1×10^{-15}				
σ_p [cm^2]	1×10^{-13}				

Parameter selection for the simulation of the double-diode behavior

Table A.3.: Summary of the chosen parameter for simulation of the double-diode behavior in figure 5.11. To simulate the double diode-behavior a surface layer (SL) within CIGSe and CdS is assumed, which has a lower valence edge relative to the absorber. For the crossover, high defect density of acceptors for the CdS was considered.

	CIGSe	**SL**	**CdS**	**i-ZnO**	**Al:ZnO**
Thickness [μm]	2.475	0.01	0.05	0.1	0.3
ϵ	$12\epsilon_0$	$12\epsilon_0$	$10\epsilon_0$	$9\epsilon_0$	$9\epsilon_0$
E_g [eV]	1.5	2.70	2.45	3.4	3.4
χ [eV]	4.05	4.05	4.3	4.5	4.5
$N_\mathrm{A/D}$ [cm^{-3}]	1×10^{16}	1.0×10^{16}	5×10^{18}	1.01×10^{18}	1×10^{18}
μ_e [cm^2/Vs]	15	15	5	20	20
μ_h [cm^2/Vs]	3	3	0.2	20	20
N_C [cm^{-3}]	2×10^{18}	2×10^{18}	4×10^{18}	1×10^{18}	1×10^{18}
N_V [cm^{-3}]	1.5×10^{19}	1.5×10^{19}	1.5×10^{19}	1×10^{19}	1×10^{19}
Midgap Defect	Donor	Donor	Acceptor	Acceptor	Acceptor
	Single	Single	Single	Single	Single
N_t[cm^{-3}]	4×10^{14}	4×10^{14}	4.999×10^{18}	1×10^{18}	1×10^{16}
σ_n[cm^2]	5×10^{-13}	5×10^{-13}	1×10^{-17}	1×10^{-15}	1×10^{-15}
σ_p[cm^2]	5×10^{-13}	5×10^{-13}	1×10^{-13}	1×10^{-12}	1×10^{-12}
Defect	Donor	Donor			
	0.2 from CB	0.2 from CB			
N_t[cm^{-3}]	8×10^{15}	8×10^{15}			
σ_n[cm^2]	4×10^{-12}	4×10^{-12}			
σ_p[cm^2]	4×10^{-15}	4×10^{-15}			
Interface States	**CIGSe/SL**	**SL/CdS**			
Defect	Donor, Single	Donor, Single			
N_t[cm^2]	1×10^{10}	1.5×10^{11}			
E_t[eV]	0.55 eV below lowest E_C	0.65 eV below lowest E_C			
σ_n[cm^2]	1×10^{-12}	1×10^{-12}			
σ_p[cm^2]	1×10^{-12}	1×10^{-16}			

Table A.4.: Summary of chosen the parameter in figure 7.5 for simulation of the double-diode behavior. The valence band edge of the p^+-layer is shifted downward. Here the p^+-layer is responsible for the crossover and the kink.

	CIGSe	p$^+$-layer	CdS	i-ZnO	Al:ZnO
Thickness [μm]	2.475	0.01	0.05	0.1	0.3
ϵ	$12\epsilon_0$	$12\epsilon_0$	$10\epsilon_0$	$9\epsilon_0$	$9\epsilon_0$
E_g [eV]	1.5	2.70	2.45	3.4	3.4
χ [eV]	4.05	4.05	4.3	4.5	4.5
$N_{A/D}$ [cm^{-3}]	1×10^{16}	8×10^{16}	5×10^{15}	1.01×10^{18}	1×10^{18}
μ_e [cm^2/Vs]	10	10	5	20	20
μ_h [cm^2/Vs]	0.1	0.1	0.2	20	20
N_C [cm^{-3}]	2×10^{18}	2×10^{18}	2×10^{18}	1×10^{18}	1×10^{18}
N_V [cm^{-3}]	1.5×10^{19}	1.5×10^{19}	1.5×10^{19}	1×10^{19}	1×10^{19}
Midgap Defect	Donor	Donor	Acceptor	Acceptor	Acceptor
	Single	Single	Single	Single	Single
N_t[cm^{-3}]	5×10^{15}	5×10^{15}	4×10^{15}	1×10^{18}	1×10^{16}
σ_n[cm^2]	1×10^{-12}	1×10^{-12}	1×10^{-16}	1×10^{-15}	1×10^{-15}
σ_p[cm^2]	1×10^{-15}	1×10^{-15}	1×10^{-12}	1×10^{-12}	1×10^{-12}
Defect	Donor				
E_t	0.2 from CB				
N_t[cm^{-3}]	5×10^{15}				
σ_n[cm^2]	1×10^{-12}				
σ_p[cm^2]	1×10^{-15}				

Interface States	CIGSe/p$^+$	p$^+$/CdS
Defect	Donor,Single	Donor,Single
N_t[cm^2]	1×10^{11}	3×10^{11}
E_t[eV]	0.65 eV below lowest E_C	0.15 eV below lowest E_C
σ_n[cm^2]	1×10^{-12}	1×10^{-13}
σ_p[cm^2]	1×10^{-16}	1×10^{-15}

B. Derivation of $\Delta V_{\text{OC}}(t)$

Derivation of $\Delta V_{\text{OC}}(t)$

The equation 6.2.1 can be further expanded by using the law of logarithm:

$$\Delta V_{\text{OC}}(t) = -\frac{k_{\text{B}}T}{q} \left[A(t)\, ln(J_0(t)) - A(t_0)\, ln(J_0(t_0)) + (A(t_0) - A(t))\, ln(J_{\text{ph}}) \right]. \quad \text{(B.1)}$$

Substitution of the saturation current density from equation 2.4.2 into equation B.1 gives:

$$
\begin{aligned}
\Delta V_{\text{OC}}(t) = &- \frac{k_{\text{B}}T}{q} A(t)\, ln\left(J_{00}(t)\, exp\left(-\frac{E_{\text{A}}}{A(t)k_{\text{B}}T}\right) \right) \\
&+ \frac{k_{\text{B}}T}{q} A(t_0)\, ln\left(J_{00}(t_0)\, exp\left(-\frac{E_{\text{A}}}{A(t_0)k_{\text{B}}T}\right) \right) \\
&- \frac{k_{\text{B}}T}{q} \left(A(t_0) - A(t) \right) ln(J_{\text{ph}}).
\end{aligned}
\quad \text{(B.2)}
$$

By applying the law of logarithms in equation B.2, the terms with the E_{A} cancel each other out and the equation B.2 reduces to:

$$
\begin{aligned}
\Delta V_{\text{OC}}(t) = &- \frac{k_{\text{B}}T}{q} \left[A(t)\, ln(J_{00}(t)) - A(t_0)\, ln(J_{00}(t_0)) \right] \\
&- \frac{k_{\text{B}}T}{q} \left(A(t_0) - A(t) \right) ln(J_{\text{ph}}).
\end{aligned}
\quad \text{(B.3)}
$$

If we define ΔA via $A(t) = A(t_0) + \Delta A$, then $\Delta V_{\text{OC}}(t)$ can be written in the more compact form in equation 6.2.3.

Derivation of $\Delta V_{\text{OC}}(t)$ with the dominant recombination at the SCR

For an absorber/window hetero-structure the electric field is defined by (B.4):

$$F_{\text{m}}(t) \approx F_{\text{z}=0}(t) = \sqrt{\frac{2q}{\epsilon_{\text{a}}} N_{\text{A,a}}(t)(V_{\text{bi}}(t) - V_{\text{OC}}(t))} \quad \text{(B.4)}$$

Similar, to the QNR-case, the ratio of $J_{00}^{scr}(t)/J_{00}^{scr}(t_0)$ is required to calculate the $\Delta V_{\text{OC}}^{scr}(t)$. From equation 6.2.6, the ratio of $J_{00}^{scr}(\text{t})$ to $J_{00}^{scr}(t_0)$ reads:

$$\frac{J_{00}^{scr}(t)}{J_{00}^{scr}(t_0)} = \sqrt{\frac{N_{A,a}(t_0)}{N_{A,a}(t)}\frac{V_{bi}(t_0) - V_{OC}(t_0)}{V_{bi}(t) - V_{OC}(t)}} \tag{B.5}$$

Here, it is assumed that the changes of V_{OC} and V_{bi} in the square root have similar time dependencies. Hence the equation B.5 is simplified to the following equation B.6:

$$\frac{J_{00}^{scr}(t)}{J_{00}^{scr}(t_0)} = \sqrt{\frac{N_{A,a}(t_0)}{N_{A,a}(t)}} \tag{B.6}$$

By inserting the equation B.6 into equation 6.2.3, the equation 6.2.7 will be achieved, which describes the $\Delta V_{OC}(t)$ of a p/n^+ with a dominant recombination in the SCR.

Derivation of $\Delta V_{OC}(t)$ with dominant recombination at the interface

Inverted absorber

The voltage dependent hole concentration at the interface can be written as:

$$p^{if}(V) = N_{V,a} \, exp\left(-\frac{E_{p,a}^{if,1}(V)}{k_B T}\right) = N_{V,a} \, exp\left(-\frac{q\,(V_{bi}(t) - V(t)) + E_{p,a}}{A(t)\,k_B T}\right) \tag{B.7}$$

with a diode quality factor:
$$A(t) = 1 + \frac{\epsilon_a N_{A,a}(t)}{\epsilon_w N_{D,w}}. \tag{B.8}$$

The equation B.8 indicates that for a junction with a dominant recombination at the interface, the diode quality factor is dependent on the doping density and through $d\,N_{A,a}(t)/dt > 0$ increases with time. The dependency of the diode quality factor $(A(t))$ on $N_{A,a}(t)$ will influence the $\Delta V_{OC}(t)$ to a large extent, since the second term in equation 6.2.3 does not vanish anymore and the photo-current and the recombination velocity will have an influence on the $\Delta V_{OC}(t)$. This is in contrary to the previous equations for ΔV_{OC}^{scr} (Eq. 6.2.7) and ΔV_{OC}^{qnr} (Eq.6.2.5), where ΔA was considered 0. This leads to a reference current density of [4]:

$$J_{00}^{if}(t) = qS_p N_{A,a}(t) \left(\frac{N_{c,w} N_{v,a}}{N_{D,w} N_{A,a}}\right)^{\frac{1}{A(t)}} = qS_p \left(\frac{N_{c,w} N_{V,a}}{N_{D,w}}\right)^{\frac{1}{A(t)}} N_{A,a}^{1-\frac{1}{A(t)}}(t) \tag{B.9}$$

From equation B.9 the ratio of $J_{00}(t)/J_{00}(t_0)$ can be calculated:

$$\frac{J_{00}^{if}(t)}{J_{00}^{if}(t_0)} = \frac{qS_{\mathrm{p}}\left(\frac{N_{\mathrm{c,w}}N_{\mathrm{v,a}}}{N_{\mathrm{D,w}}}\right)^{\frac{1}{A(t)}} N_{\mathrm{A,a}}^{1-\frac{1}{A(t_0)}+\frac{\Delta A}{A^2(t_0)}}(t)}{qS_{\mathrm{p}}\left(\frac{N_{\mathrm{c,w}}N_{\mathrm{v,a}}}{N_{\mathrm{D,w}}}\right)^{\frac{1}{A(t_0)}} N_{\mathrm{A,a}}^{1-\frac{1}{A(t_0)}}(t_0)} \tag{B.10}$$

Since $\Delta A(t)$ is small compared to $A(t)$, the following approximations have been used:

$$\frac{1}{A(t)} - \frac{1}{A(t_0)} = \frac{-\Delta A(t)}{(A(t_0)+\Delta A(t))A(t_0)} \approx -\frac{\Delta A(t)}{A^2(t_0)} \tag{B.11}$$

By inserting equation B.9 into equation 6.2.3, the following relation (Eq.B.12) can be obtained:

$$\Delta V_{\mathrm{OC}}^{if}(t) = -\frac{k_{\mathrm{B}}T}{q}A(t_0)\, ln\left[\left(\frac{N_{\mathrm{c,w}}N_{\mathrm{V,a}}}{N_{\mathrm{D,w}}}\right)^{-\frac{\Delta A(t)}{A^2(t_0)}}\left(\frac{N_{\mathrm{A,a}}(t)}{N_{\mathrm{A,a}}(t_0)}\right)^{1-\frac{1}{A(t_0)}}\left(N_{\mathrm{A,a}}(t)\right)^{\frac{\Delta A(t)}{A^2(t_0)}}\right]$$

$$-\frac{k_{\mathrm{B}}T}{q}\Delta A(t)\, ln\left(\frac{J_{00}^{\mathrm{if}}(t)}{J_{\mathrm{ph}}}\right) \tag{B.12}$$

The equation B.12 is reformulated, so that $A(t)$ and $\Delta A(t)$ are separated:

$$\begin{aligned}
\Delta V_{\mathrm{OC}}^{if}(t) = &+\frac{k_{\mathrm{B}}T}{q}\frac{\Delta A(t)}{A(t_0)}\, ln\left(\frac{N_{\mathrm{c,w}}N_{\mathrm{V,a}}}{N_{\mathrm{D,w}}}\right)\\
&+\frac{k_{\mathrm{B}}T}{q}(1-A(t_0))\, ln\left(\frac{N_{\mathrm{A,a}}(t)}{N_{\mathrm{A,a}}(t_0)}\right)\\
&-\frac{k_{\mathrm{B}}T}{q}\frac{\Delta A(t)}{A(t_0)}\, ln(N_{\mathrm{A,a}}(t))\\
&-\frac{k_{\mathrm{B}}T}{q}\Delta A(t)\, ln\left(\frac{J_{00}^{\mathrm{if}}(t)}{J_{\mathrm{ph}}}\right)
\end{aligned} \tag{B.13}$$

The term $\Delta A(t)$ is defined:

$$\Delta A(t) = 1 + \frac{\epsilon_a\, N_{\mathrm{A,a}}(t)}{\epsilon_w\, N_{\mathrm{D,w}}} - 1 - \frac{\epsilon_a\, N_{\mathrm{A,a}}(t_0)}{\epsilon_w\, N_{\mathrm{D,w}}} = \frac{\epsilon_a\, \Delta N_{\mathrm{A,a}}(t)}{\epsilon_w\, N_{\mathrm{D,w}}} \tag{B.14}$$

By inserting the ΔA (Eq. B.14) into equation B.13 the final equation B.15 can be achieved:

$$\Delta V_{OC}^{if}(t) = + \frac{k_B T}{q}(1 - A(t_0)) \, ln\left(\frac{N_{A,a}(t)}{N_{A,a}(t_0)}\right)$$
$$+ \frac{k_B T}{qA(t_0)} \frac{\epsilon_a}{\epsilon_w} \frac{\Delta N_{A,a}(t)}{N_{D,w}} \, ln\left(\frac{N_{c,w} N_{V,a}}{N_{D,w} N_{A,a}(t)}\right) \quad (B.15)$$
$$- \frac{k_B T}{q} \frac{\epsilon_a}{\epsilon_w} \frac{\Delta N_{A,a}(t)}{N_{D,w}} \, ln\left(\frac{J_{00}(t)}{J_{ph}^{if}}\right).$$

Non-inverted absorber

So far, it was assumed that the absorber is inverted, and the recombination at the interface is controlled by the holes [34]. But if the junction is not inverted, the net recombination rate reduces to $R \approx n^{if} S_n$. Here, n^{if} is the density of the electrons at the interface, and S_n is the interface recombination velocity of the electrons. The electron concentration at the interface reads [4]:

$$n^{if}(V) = N_{D,w} \, exp\left(-\frac{q(V_{bi} - V)}{A' k_B T}\right) \quad (B.16)$$

To prevent any ambiguity with the inverted case, the notation A' is used for the diode quality factor of the non-inverted and defined in equation B.19. The built-in voltage here is defined as $qV_{bi} = E_{g,a} + \Delta E_C - E_{n,w} - E_{p,a}$ [30]. Here, $E_{g,a}$ is the bandgap of the absorber and ΔE_C is the band offset between the absorber and window layer. By the definition of the net recombination rate and the defined built-in voltage (V_{bi}), the diode current density (J_{diode}) can be obtained:

$$J_{diode}(V) = \underbrace{qS_n N_{D,w} \, exp\left(\frac{E_{n,w} + E_{p,a}}{A' k_B T}\right)}_{J_{00}} exp\left(-\frac{E_{g,a} + \Delta E_C}{A' k_B T}\right) exp\left(\frac{qV}{A' k_B T}\right) \quad (B.17)$$

Under the assumption that the dopants are completely ionized, the Boltzmann approximation can be used [30], this leads to a reference current density (J_{00}) of (Eq. B.18):

$$J_{00}(t) = qN_{D,w} S_n \left(\frac{N_{C,w} N_{V,a}}{N_{D,w} N_{A,a}(t)}\right)^{\frac{1}{A'(t)}} \quad (B.18)$$

with the diode quality factor $A'(t)$,

$$A'(t) = 1 + \frac{\epsilon_w N_{D,w}}{\epsilon_a N_{A,a}(t)}. \quad (B.19)$$

From equation B.19, it can be understood that for a non-inverted case the $\epsilon_w N_{D,w}$ must be comparable to $\epsilon_a N_{A,a}$. Furthermore, the diode quality factor reduces upon illumination, this means for a not-inverted cell, the changes of the diode quality factor is negative ($\Delta A'(t) < 0$). The computation of $J_{00}(t)/J_{00}(t_0)$ with the extracted $J_{00}(t)$ in equation B.18, gives:

$$\frac{J_{00}(t)}{J_{00}(t_0)} = \frac{qS_{n,0}N_{D,w}\left(\frac{N_{c,w}N_{V,a}}{N_{D,w}}\right)^{\frac{1}{A'(t)}}\frac{1}{N_{A,a}(t)}^{\frac{1}{A'(t_0)}}}{qS_{n,0}N_{D,w}\left(\frac{N_{c,w}N_{V,a}}{N_{D,w}}\right)^{\frac{1}{A'(t_0)}}\frac{1}{N_{A,a}(t_0)}^{\frac{1}{A'(t_0)}}} \tag{B.20}$$

Substituting equation B.20 into equation 6.2.3, the $\Delta V_{OC}(t)$ becomes:

$$\begin{aligned}
\Delta V_{OC}(t) = &- \frac{k_B T}{q}A'(t_0)\,ln\left(\frac{N_{c,w}N_{v,a}}{N_{D,w}}\right)^{-\frac{\Delta A'(t)}{A'^2(t_0)}} \\
&- \frac{k_B T}{q}A'(t_0)\,ln\left(\frac{N_{A,a}(t_0)}{N_{A,a}(t)}\right)^{\frac{1}{A'(t_0)}} \\
&- \frac{k_B T}{q}A'(t_0)\,ln\left(N_{A,a}(t)\right)^{\frac{\Delta A'(t)}{A'^2(t_0)}} \\
&- \frac{k_B T}{q}\Delta A'(t)\,ln\left(\frac{J_{00}(t)}{J_{ph}}\right).
\end{aligned} \tag{B.21}$$

with some modification, the final $\Delta V_{OC}(t)$ for a non-inverted case will be:

$$\begin{aligned}
\Delta V_{OC}(t) = &\frac{k_B T}{q}\,ln\left(\frac{N_{A,a}(t)}{N_{A,a}(t_0)}\right) \\
&+ \frac{k_B T}{q}(\frac{\Delta A'(t)}{A'(t_0)})\,ln\left(\frac{N_{c,w}N_{v,a}}{N_{D,w}N_{A,a}(t)}\right) \\
&- \frac{k_B T}{q}\Delta A'(t)\,ln\left(\frac{J_{00}(t)}{J_{ph}}\right).
\end{aligned} \tag{B.22}$$

Note that, due to the negative $\Delta A'(t)$, the first and last terms are positive in equation B.22 and results in an increasing trend of the ΔV_{OC} for the non-inverted structure. However, since the doping density of the initial states are lower than 2×10^{16} (cm^{-3}), the samples with the GGI = 0.3 are indeed inverted and are limited by recombination in the bulk.

C. Time evolution of the admittance spectrum

In order to extract the doping transients of the RbF-treated and untreated sample, the capacitance-frequency spectrum (C(f,t)) of the samples were measured as explained in section 3.6.3. The raw data from the capacitance spectrum of both RbF-treated and untreated samples with the GGI = 0.3 and 0.75 are shown in the figure C.1(a - b). The relaxed states are illustrated with dashed lines (C(f,t_0)). The C(f,t_0) signal of RbF-treated samples is higher than that of the untreated sample. This implies that the doping density of RbF-treated samples increases compared to the untreated sample. The space charge region capacitance (C_{scr}) is determined at the frequency f, where the logarithmic derivative of $-\frac{dC}{d(log f)}$ has its minimum value [14]. For instance for RbF-treated samples with GGI = 0.3, the C_{scr} is at the frequency of 10^5 Hz. Upon illumination, the RbF-treated and untreated samples with GGI = 0.3 change to larger capacitance values. However, this is different for samples with GGI = 0.75. For sample with the GGI = 0.75, the C_{scr} of the RbF-treated increases about 2.5 times above its relaxed state. Since the doping density is proportional to C_{scr}^2, the doping density increases about 6.2 times with respect to its initial value. But for the untreated sample the C_{scr} increases just 1.4 times with respect to its initial value.
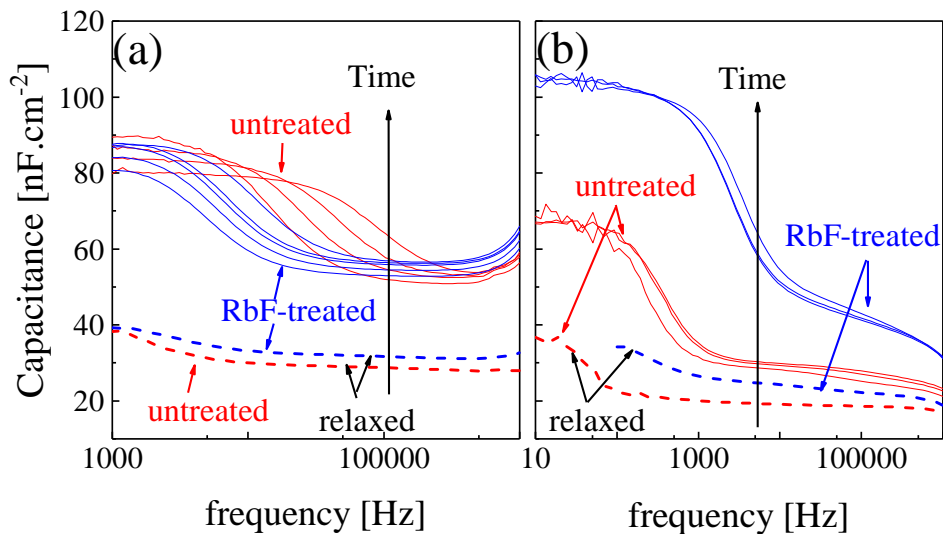
Figure C.1.: Linear plot of capacitance transients of RbF-treated (blue) and untreated (red) at 130 K and 298 K red-light illumination with corresponding power law fit (dashed), sample with (a) GGI = 0.3, (b) GGI = 0.75.

In order to confirm the reproducibility of doping transients observed in figure 6.8, another set of sample with the GGI = 0.83 was prepared. The buffer layer of both samples were processed in the same run, therefore, the influence of the buffer thickness and the defect density can be discarded. The measurement results of $\Delta V_{OC}(t)$ show that similar to graph 6.4, the $V_{OC}(t)$ of RbF-treated changes in slower rate compared to the untreated sample.
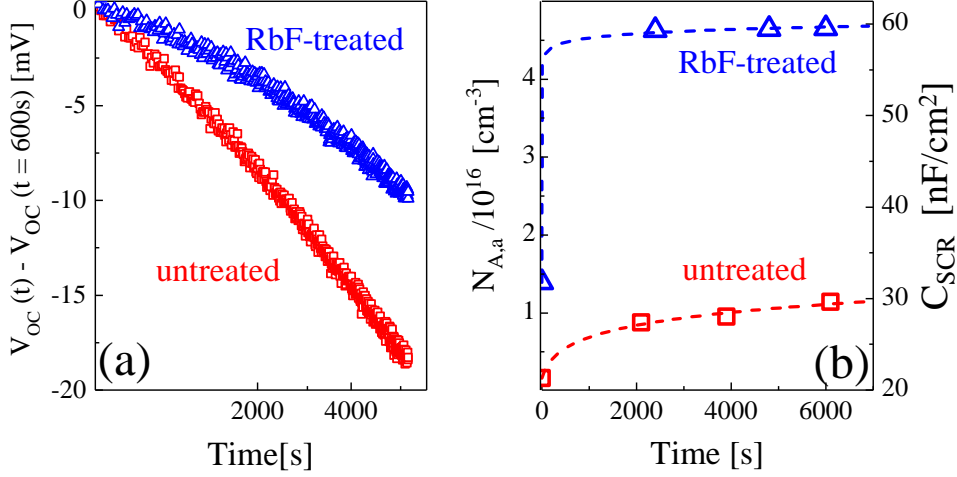
Figure C.2.: Time evolution of the RbF-treated and untreated CIGSe with GGI = 0.8 (a) time evolution of $V_{OC}(t)$, (b) doping density transients $(N_{A,a}(t))$ upon red light illumination.

In figure C.2(b), the doping transients of corresponding samples are shown. The measurement indicates that the capacitance of the RbF-treated sample increases strongly at the initial phase to higher doping densities similar to previous sample in figure 6.8, while the untreated sample just increases one order of magnitude with respect to its initial value.

D. Measurement of the quasi-Fermi level splitting

In chapter 7 it was shown that growing the CIGSe on High-T substrates increases the V_{OC}. But what is the maximum V_{OC} that can be achieved by a CIGSe absorber, when they are grown at elevated temperature and are treated with heavy alkali? And for which bandgap value of the CIGSe absorber, the negative band offset between the CIGSe and CdS have a detrimental impact on the V_{OC}? One method to determine the maximum achievable open-circuit voltage of final devices is to measure the photoluminiscence at room temperature and extracting the Bose-term in Planck's generalized law [131].
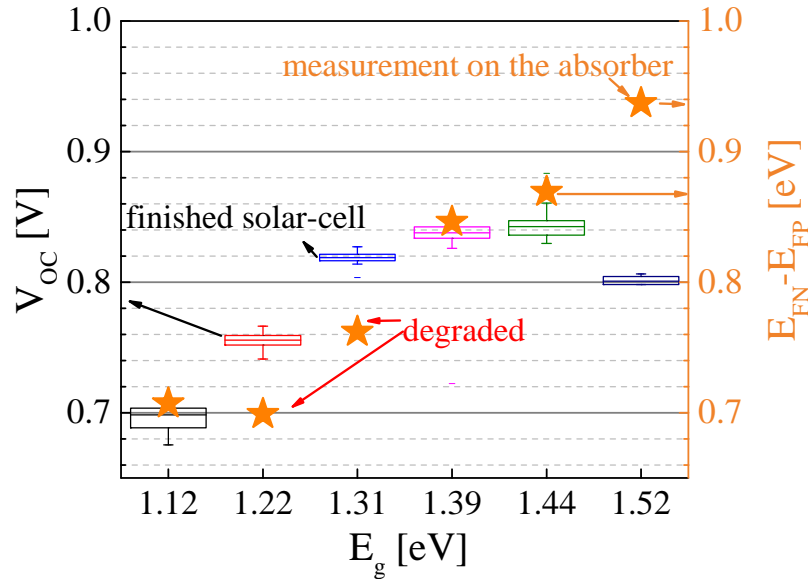
Figure D.1.: Comparison of the measured V_{OC} on the cell and the maximum quasi-Fermi level splitting on the bare Cu(In,Ga)Se$_2$ absorber for different bandgap values. The measured V_{OC} is 800 mV for E_g 1.52 eV, while the quasi-fermi level splits to 940 mV.

Therefore, RbF-treated CIGSe absorbers with different gallium concentration were prepared on High-T substrates. The absorbers were grown according to the multi-stage process (see section 3.3.2) and no NaF was introduced as a precursor. From each run an absorber was finished to solar cells (as explained in chapter 3) and one absorber was sent to Helmholtz Zentrum Berlin (HZB) to determine the maximum quasi-Fermi splitting. The measurement was performed at room temperature.

In figure D.1, the measured V_{OC} from the cell and the quasi-Fermi level splitting of the corresponding cells are marked with a star. The figure D.1 indicates that the quasi-Fermi level splitting of $E_g = 1.12$ eV is 707 meV which is equal to the measured V_{OC} value on the cell times the electron charge. Two of the samples with E_g of 1.22 eV and 1.31 eV were degraded and the quasi-Fermi level splitting value could not be determined accurately. For $E_g = 1.39$ eV, the quasi-Fermi level splitting reaches 846 meV and is again equal to the final V_{OC} device. This indicates that the band offset at the CIGSe and CdS is not having a detrimental influence on the V_{OC}. But as the bandgap of the CIGSe absorber increases to 1.44 eV, the quasi-Fermi level splitting and the V_{OC} start to deviate. While the quasi-Fermi level splitting of the absorber reaches 940 meV, the measured V_{OC} on the cell is only 800 mV. This experiment shows that the band offset between CIGSe and CdS is detrimental for CIGSe cells with bandgap of 1.44 eV, therefore in appendix E, two alternative buffer layers will be examined.

E. Influence of alternative buffer layers

Zn(Mg,O)/CIGSe

The small bandgap of CdS absorbs a large amounts of photons [132]. An alternative buffer layer which has a large bandgap and allows a higher portion of light to be transmitted is Zn(Mg,O) [132].
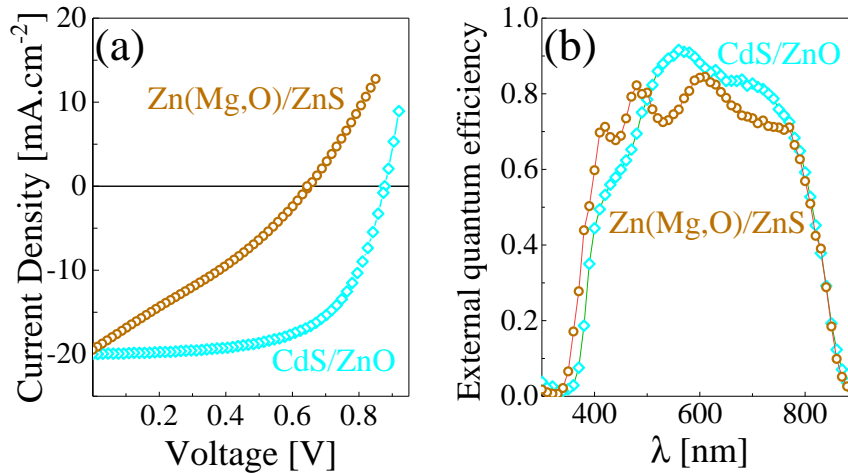
Figure E.1.: Comparison of the ZnS/(Zn,Mg)O and CdS/ZnO on the solar cell parameters. The wide-gap CIGSe sample with CdS/ZnO show a superior performance.

In order to examine the influence of the alternative buffer layer, in cooperation with ZSW, alkali-treated wide-gap absorbers were sent to ZSW to get finished cells with the deposition of ZnS/(Zn,Mg)O/ZnO:Al. From the same run as a reference, a sample with CdS/i-ZnO/ZnO:Al was finished to cells in MLU. The JV-curves of the cells with ZnS/(Zn,Mg)O and the CdS/i-ZnO/ZnO:Al are illustrated in figure E.1(a). Despite the gain of the current density in short wavelengths of the ZnS/(Zn,Mg)O sample (Fig.E.1(b)), the V_{OC} is very low compared to the reference sample. Unfortunately, annealing and light-soaking for two hours did not improve the efficiency of the cell further and the FF was very low.

Zn(Sn,O)/CIGSe

A small positive conduction band offset between the absorber and the buffer material is important to improve the solar cell efficiency [5]. In chapter 5 it was shown that the band

offset between the wide-gap CIGSe and CdS is negative, which is not favorable. This increases the recombination at the interface [8]. One way, to reduce the recombination is to improve the inversion. This was achieved by lowering the valence band edge with alkali post deposition treatment as shown in chaper 5. But as shown in chapter 6, the $V_{OC}(t)$ transients indicated that the alkali-treated samples are limited by interface recombination.
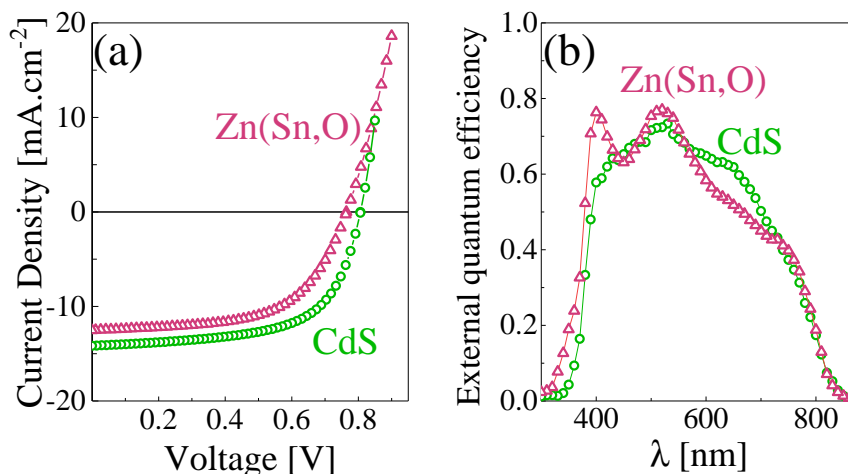
Figure E.2.: Comparison of the Zn(Sn,O)/ZnO:Al and CdS/ZnO on the solar cell parameters. The wide-gap CIGSe sample with CdS/ZnO show a superior performance.

Recently, Larsson et al.[5] have suggested Zn(Sn,O) as an alternative buffer layer for wide gap CuGaSe$_2$ cells to create a positive conduction band offset. Due to the specific deposition method which was not possible in MLU, the alkali-treated CIGSe absorbers were coated with CdS and half of them were sent to the university of Uppsala to complete to cells. Another half were finished to solar cells as described in chapter 3. The CdS was etched in Uppsala university and were coated with Zn(Sn,O) and then ZnO:Al. The steps taken to complete the cells are described in [5]. After the deposition of the Zn(Sn,O)/ZnO:Al, the cells were sent back to MLU, for further characterization. The cells required annealing and light soaked to improve the efficiency. In figure E.2 the annealed JV-curve and EQE results are shown. As can be seen in figure E.2, the final open-circuit voltage was lower than for the sample with CdS. Therefore substitution of the buffer layer with Zn(Sn,O) for alkali-treated wide-gap CIGSe samples failed.

Influence of alkali-PDT on EQE signal for different bandgap values of CIGSe absorber

In section 5.1.2, it was shown that RbF-PDT show a gain in the EQE signal at long wavelength compared to the untreated samples. In figure E.3, the EQE signal of KF and CsF-treated samples are compared to the untreated sample.
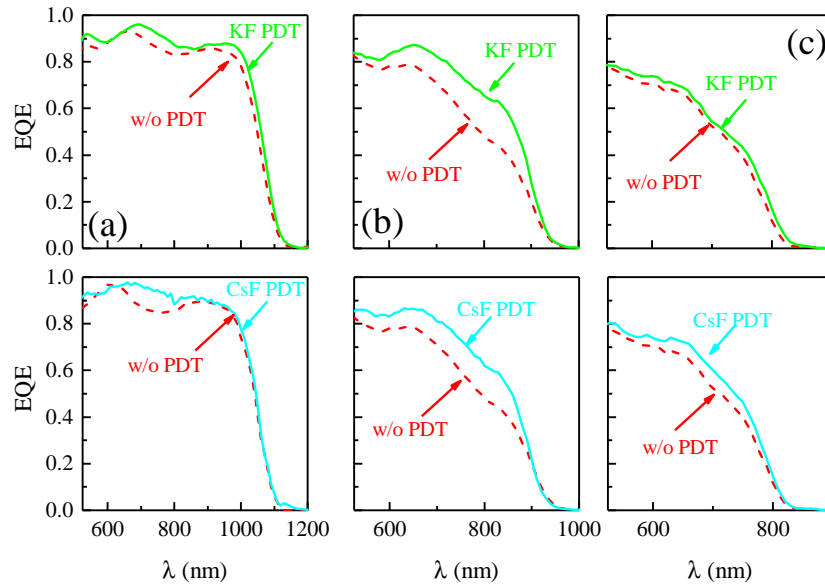
Figure E.3.: EQE signal of KF-treated (top) and CsF-treated (bottom) samples for different bandgap values, (a) $E_g = 1.12$ eV, (b) $E_g = 1.34$ eV, and (c) $E_g = 1.52$ eV.

Collection efficiency of the double-diode

In section 5.2, it was shown that the V_{OC} of the alkali-treated samples saturates at low temperatures. Meanwhile, in section 4.3, it was shown that the V_{OC} is dependent on the collection efficiency. Therefore, the collection efficiency of the double-diode JV-curve was computed with the simulation program. It can be observed that the saturation of the V_{OC} comes from the reduction of the collection efficiency at high voltages.
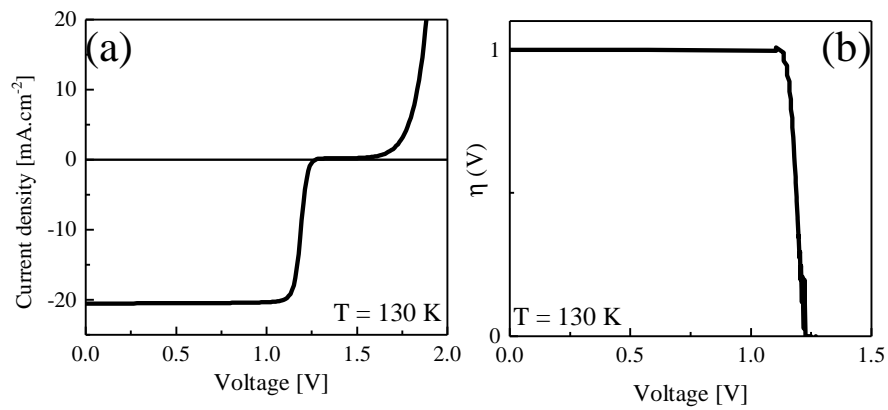
Figure E.4.: (a) The double-diode JV-curve, (b) the simulated collection efficiency at T = 130 K.

Bibliography

[1] S. Siebentritt and U. Rau. *Wide-gap chalcopyrites*. Vol. 1. Springer, 2006.

[2] MA. Contreras, LM. Mansfield, B. Egaas, J. Li, M. Romero, R. Noufi, E. Rudiger-Voigt, and W. Mannstadt. "Wide bandgap Cu(In,Ga)Se$_2$ solar cells with improved energy conversion efficiency". In: *Progress in Photovoltaics: Research and Applications* 20.7 (2012), pp. 843–850.

[3] W. Shockley and HJ. Queisser. "Detailed balance limit of efficiency of p-n junction solar cells". In: *Journal of applied physics* 32.3 (1961), pp. 510–519.

[4] R. Scheer and HW. Schock. *Chalcogenide photovoltaics: physics, technologies, and thin film devices*. John Wiley & Sons, 2011.

[5] F. Larsson, N. Shariati Nilsson, J. Keller, Ch. Frisk, V. Kosyak, M. Edoff, and T. Törndahl. "Record 1.0 V open-circuit voltage in wide band gap chalcopyrite solar cells". In: *Progress in Photovoltaics: Research and Applications* 25.9 (2017), pp. 755–763.

[6] S. Ishizuka. "CuGaSe$_2$ Thin Film Solar Cells: Challenges for Developing Highly Efficient Wide-Gap Chalcopyrite Photovoltaics". In: *physica status solidi (a)* (2019), p. 1800873.

[7] WN. Shafarman, R. Klenk, and MA. McCanGreen. "Characterization of Cu(In,Ga)Se$_2$ solar cells with high Ga content". In: *Conference Record of the Twenty Fifth IEEE Photovoltaic Specialists Conference-1996*. IEEE. 1996, pp. 763–768.

[8] M. Gloeckler and JR. Sites. "Efficiency limitations for wide-band-gap chalcopyrite solar cells". In: *Thin Solid Films* 480 (2005), pp. 241–245.

[9] T. Lavrenko, T. Ott, and T. Walter. "Impact of sulfur and gallium gradients on the performance of thin film Cu(In,Ga)(Se,S)$_2$ solar cells". In: *Thin Solid Films* 582 (2015), pp. 51–55.

[10] E. Handick, P. Reinhard, JH. Alsmeier, L. Köhler, F. Pianezzi, S. Krause, M. Gorgoi, E. Ikenaga, N. Koch, RG. Wilks, et al. "Potassium postdeposition treatment-induced band gap widening at Cu(In,Ga)Se$_2$ surfaces–reason for performance leap?" In: *ACS applied materials & interfaces* 7.49 (2015), pp. 27414–27420.

[11] D. Hauschild, D. Kreikemeyer-Lorenzo, P. Jackson, TM. Friedlmeier, D. Hariskos, F. Reinert, M. Powalla, C. Heske, and L. Weinhardt. "Impact of a RbF Postdeposition Treatment on the Electronic Structure of the CdS/Cu(In,Ga)Se$_2$ Heterojunction in High-Efficiency Thin-Film Solar Cells". In: *ACS Energy Letters* 2.10 (2017), pp. 2383–2387.

[12] P. Pistor, D. Greiner, CA. Kaufmann, S. Brunken, M. Gorgoi, A. Steigert, W. Calvet, I. Lauermann, R. Klenk, T. Unold, et al. "Experimental indication for band gap widening of chalcopyrite solar cell absorbers after potassium fluoride treatment". In: *Applied Physics Letters* 105.6 (2014), p. 063901.

[13] M. Ćwil, M. Igalson, P. Zabierowski, CA. Kaufmann, and A. Neisser. "Capacitance profiling in the CIGS solar cells". In: *Thin Solid Films* 515.15 (2007), pp. 6229–6232.

[14] F. Obereigner, N. Barreau, W. Witte, and R. Scheer. "Open-circuit and doping transients of Cu(In,Ga)Se$_2$ solar cells with varying Ga content". In: *Journal of Applied Physics* 117.5 (2015), p. 055704.

[15] H. Wilhelm, HW. Schock, and R. Scheer. "Interface recombination in heterojunction solar cells: Influence of buffer layer thickness". In: *Journal of Applied Physics* 109.8 (2011), p. 084514.

[16] SM. Sze and KK. Ng. *Physics of semiconductor devices.* John Wiley & Sons, 2006.

[17] J. Nelson. *The physics of solar cells.* World Scientific Publishing Company, 2003.

[18] MA. Green. "Do built-in fields improve solar cell performance?" In: *Progress in Photovoltaics: Research and Applications* 17.1 (2009), pp. 57–66.

[19] S. Fonash. *Solar cell device physics.* Elsevier, 2012.

[20] M. Topič, F. Smole, and J. Furlan. "Band-gap engineering in CdS/Cu(In,Ga)Se$_2$ solar cells". In: *Journal of applied physics* 79.11 (1996), pp. 8537–8540.

[21] C. Donolato. "A reciprocity theorem for charge collection". In: *Applied Physics Letters* 46.3 (1985), pp. 270–272.

[22] MA. Green. *Solar cells: operating principles, technology, and system applications.* Longman Higher Education, 1982.

[23] A. Niemegeers, M. Burgelman, and A. De Vos. "On the CdS/CuInSe$_2$ conduction band discontinuity". In: *Applied physics letters* 67.6 (1995), pp. 843–845.

[24] W. Shockley and WT. Read Jr. "Statistics of the recombinations of holes and electrons". In: *Physical review* 87.5 (1952), p. 835.

[25] U. Rau. "Tunneling-enhanced recombination in Cu(In,Ga)Se$_2$ heterojunction solar cells". In: *Applied Physics Letters* 74.1 (1999), pp. 111–113.

[26] A. De Vos. "The fill factor of a solar cell from a mathematical point of view". In: *Solar cells* 8.3 (1983), pp. 283–296.

[27] R. Kniese, M. Lammer, U. Rau, and M. Powalla. "Minority carrier collection in CuGaSe$_2$ solar cells". In: *Thin Solid Films* 451-452 (2004). Proceedings of Symposium D on Thin Film and Nano-Structured Materials for Photovoltaics, of the E-MRS 2003 Spring Conference, pp. 430 –433.

[28] V. Nadenau, U. Rau, A. Jasenek, and HW. Schock. "Electronic properties of CuGaSe$_2$-based heterojunction solar cells. Part I. Transport analysis". In: *Journal of Applied Physics* 87.1 (2000), pp. 584–593.

[29]   U. Rau and HW. Schock. "Electronic properties of Cu(In,Ga)Se$_2$ heterojunction solar cells–recent achievements, current understanding, and future challenges". In: *Applied Physics A* 69.2 (1999), pp. 131–147.

[30]   R. Scheer. "Activation energy of heterojunction diode currents in the limit of interface recombination". In: *Journal of Applied Physics* 105.10 (2009), p. 104505.

[31]   SH. Wei and A. Zunger. "Band offsets and optical bowings of chalcopyrites and Zn-based II-VI alloys". In: *Journal of Applied Physics* 78.6 (1995), pp. 3846–3856.

[32]   M. Turcu, IM. Kötschau, and U. Rau. "Composition dependence of defect energies and band alignments in the Cu (In$_{1-x}$,Ga$_x$)(Se$_{1-y}$S$_y$)$_2$ alloy system". In: *Journal of Applied Physics* 91.3 (2002), pp. 1391–1399.

[33]   S. Siebentritt. "Wide gap chalcopyrites: material properties and solar cells". In: *Thin Solid Films* 403 (2002), pp. 1–8.

[34]   M. Turcu and U. Rau. "Fermi level pinning at CdS/Cu(In,Ga)(Se,S)$_2$ interfaces: effect of chalcopyrite alloy composition". In: *Journal of Physics and Chemistry of Solids* 64.9-10 (2003), pp. 1591–1595.

[35]   M. Takashi, M. Takuya, T. Hideyuki, H. Yoshihiro, N. Takayuki, H. Yasuhiro, U. Takeshi, and K. Masatoshi. "Theoretical analysis of the effect of conduction band offset of window/-CIS layers on performance of CIS solar cells using device simulation". In: *Solar Energy Materials and Solar Cells* 67.1 (2001). PVSEC 11 - PART III, pp. 83 –88. ISSN: 0927-0248.

[36]   T. Kato, J. Wu, Y. Hirai, H. Sugimoto, and V. Bermudez. "Record efficiency for thin-film polycrystalline solar cells up to 22.9% achieved by Cs-treated Cu(In,Ga)(Se,S)$_2$". In: *IEEE Journal of Photovoltaics* 9.1 (2018), pp. 325–330.

[37]   A. Chirilă, P. Reinhard, F. Pianezzi, P. Bloesch, AR. Uhl, C. Fella, L. Kranz, D. Keller, Gretenothers., H. Hagendorfer, et al. "Potassium-induced surface modification of Cu(In,Ga)Se$_2$ thin films for high-efficiency solar cells". In: *Nature materials* 12.12 (2013), p. 1107.

[38]   P. Jackson, R. Wuerz, D. Hariskos, E. Lotter, W. Witte, and M. Powalla. "Effects of heavy alkali elements in Cu(In,Ga)Se$_2$ solar cells with efficiencies up to 22.6%". In: *physica status solidi (RRL)–Rapid Research Letters* 10.8 (2016), pp. 583–586.

[39]   P. Jackson, D. Hariskos, R. Wuerz, W. Wischmann, and M. Powalla. "Compositional investigation of potassium doped Cu(In,Ga)Se$_2$ solar cells with efficiencies up to 20.8%". In: *physica status solidi (RRL)–Rapid Research Letters* 8.3 (2014), pp. 219–222.

[40]   SA. Jensen, S. Glynn, A. Kanevce, P. Dippo, JV. Li, DH. Levi, and D. Kuciauskas. "Beneficial effect of post-deposition treatment in high-efficiency Cu(In,Ga)Se$_2$ solar cells through reduced potential fluctuations". In: *Journal of Applied Physics* 120.6 (2016), p. 063106.

[41] I. Khatri, H. Fukai, H. Yamaguchi, M. Sugiyama, and T. Nakada. "Effect of potassium fluoride post-deposition treatment on Cu(In,Ga)Se$_2$ thin films and solar cells fabricated onto sodalime glass substrates". In: *Solar Energy Materials and Solar Cells* 155 (2016), pp. 280–287.

[42] I. Khatri, M. Sugiyama, and T. Nakada. "Effects of combined additional indium deposition and potassium fluoride post-deposition treatments on Cu(In,Ga)Se$_2$ thin film solar cells". In: *Progress in Photovoltaics: Research and Applications* 25.10 (2017), pp. 871–877.

[43] FH. Pianezzi. "Electronic transport and doping mechanisms in Cu(In,Ga)Se$_2$ thin film solar cells". PhD thesis. ETH Zurich, 2014.

[44] IL. Repins, WK. Metzger, CL. Perkins, JV. Li, and MA. Contreras. "Measured minority-carrier lifetime and CIGS device performance". In: *2009 34th IEEE Photovoltaic Specialists Conference (PVSC)*. IEEE. 2009, pp. 000978–000983.

[45] S. Ishizuka, N. Taguchi, and PJ. Fons. "Similarities and Critical Differences in Heavy Alkali-Metal Rubidium and Cesium Effects on Chalcopyrite Cu(In,Ga)Se$_2$ Thin-Film Solar Cells". In: *The Journal of Physical Chemistry C* 123.29 (2019), pp. 17757–17764.

[46] T. Lepetit. "Influence of KF post deposition treatment on the polycrystalline Cu(In,Ga)Se$_2$ / CdS heterojunction formation for photovoltaic application". PhD thesis. Nantes, 2015.

[47] N. Nicoara, T. Lepetit, L. Arzel, S. Harel, N. Barreau, and S. Sadewasser. "Effect of the KF post-deposition treatment on grain boundary properties in Cu(In,Ga)Se$_2$ thin films". In: *Scientific reports* 7 (2017), p. 41361.

[48] P. Jackson, D. Hariskos, R. Wuerz, O. Kiowski, A. Bauer, TM. Friedlmeier, and M. Powalla. "Properties of Cu(In,Ga)Se$_2$ solar cells with new record efficiencies up to 21.7%". In: *physica status solidi (RRL)–Rapid Research Letters* 9.1 (2015), pp. 28–31.

[49] L. Margulis, G. Hodes, A. Jakubowicz, and D. Cahen. "Aggregate structure in CuBSe$_2$/Mo films (B= In,Ga): Its relation to their electrical activity". In: *Journal of Applied Physics* 66.8 (1989), pp. 3554–3559.

[50] D. Rudmann. "Effects of sodium on growth and properties of Cu(In,Ga)Se$_2$ thin films and solar cells". PhD thesis. ETH Zurich, 2004.

[51] R. Caballero, CA. Kaufmann, T. Eisenbarth, T. Unold, S. Schorr, R. Hesse, R. Klenk, and HW. Schock. "The effect of NaF precursors on low temperature growth of CIGS thin film solar cells on polyimide substrates". In: *physica status solidi (a)* 206.5 (2009), pp. 1049–1053.

[52] S. Ishizuka, A. Yamada, MM. Islam, H. Shibata, P. Fons, T. Sakurai, K. Akimoto, and Sh. Niki. "Na-induced variations in the structural, optical, and electrical properties of Cu(In,Ga)Se$_2$ thin films". In: *Journal of applied physics* 106.3 (2009), p. 034908.

[53] R. Wuerz, A. Eicke, F. Kessler, P. Rogin, and O. Yazdani-Assl. "Alternative sodium sources for Cu(In,Ga)Se$_2$ thin-film solar cells on flexible substrates". In: *Thin Solid Films* 519.21 (2011), pp. 7268–7271.

[54]   U. Rau, M. Schmitt, F. Engelhardt, O. Seifert, J. Parisi, W. Riedl, J. Rimmasch, and F. Karg. "Impact of Na and S incorporation on the electronic transport mechanisms of Cu(In,Ga)Se$_2$ solar cells". In: *Solid state communications* 107.2 (1998), pp. 59–63.

[55]   PMP. Salomé, H. Rodriguez-Alvarez, and S. Sadewasser. "Incorporation of alkali metals in chalcogenide solar cells". In: *Solar Energy Materials and Solar Cells* 143 (2015), pp. 9–20.

[56]   D. Rudmann, G. Bilger, M. Kaelin, FJ. Haug, H. Zogg, and AN. Tiwari. "Effects of NaF coevaporation on structural properties of Cu(In,Ga)Se$_2$ thin films". In: *Thin Solid Films* 431 (2003), pp. 37–40.

[57]   T. Wada, N. Kohara, S. Nishiwaki, and T. Negami. "Characterization of the Cu(In,Ga)Se$_2$ /Mo interface in CIGS solar cells". In: *Thin Solid Films* 387.1-2 (2001), pp. 118–122.

[58]   A. Duchatelet, G. Savidand, RN. Vannier, and D. Lincot. "Optimization of MoSe$_2$ formation for Cu(In,Ga)Se$_2$-based solar cells by using thin superficial molybdenum oxide barrier layers". In: *Thin Solid Films* 545 (2013), pp. 94–99.

[59]   N. Kohara, S. Nishiwaki, Y. Hashimoto, T. Negami, and T. Wada. "Electrical properties of the Cu(In,Ga)Se$_2$/MoSe$_2$/Mo structure". In: *Solar Energy Materials and Solar Cells* 67.1-4 (2001), pp. 209–215.

[60]   AM. Gabor, JR. Tuttle, DS. Albin, MA. Contreras, R. Noufi, and AM. Hermann. "High-efficiency CuIn$_x$Ga$_{1-x}$Se$_2$ solar cells made from (In$_x$,Ga$_{1-x}$)$_2$Se$_3$ precursor films". In: *Applied Physics Letters* 65.2 (1994), pp. 198–200.

[61]   P. Pistor, S. Zahedi-Azad, S. Hartnauer, LA. Wägele, E. Jarzembowski, and R. Scheer. "Real time observation of phase formations by XRD during Ga-rich or In-rich Cu(In,Ga)Se$_2$ growth by co-evaporation". In: *physica status solidi (a)* 212.9 (2015), pp. 1897–1904.

[62]   R. Scheer, A. Neisser, K. Sakurai, P. Fons, and S. Niki. "Cu(In$_{1-x}$Ga$_x$)Se$_2$ growth studies by in situ spectroscopic light scattering". In: *Applied physics letters* 82.13 (2003), pp. 2091–2093.

[63]   K. Sakurai, R. Hunger, R. Scheer, CA. Kaufmann, A. Yamada, T. Baba, Y. Kimura, K. Matsubara, P. Fons, H. Nakanishi, et al. "In situ diagnostic methods for thin-film fabrication: utilization of heat radiation and light scattering". In: *Progress in Photovoltaics: Research and Applications* 12.2-3 (2004), pp. 219–234.

[64]   D. Hariskos, M. Powalla, N. Chevaldonnet, D. Lincot, A. Schindler, and B. Dimmler. "Chemical bath deposition of CdS buffer layer: prospects of increasing materials yield and reducing waste". In: *Thin Solid Films* 387.1-2 (2001), pp. 179–181.

[65]   N. Barreau, JC. Bernede, S. Marsillac, C. Amory, and WN. Shafarman. "New Cd-free buffer layer deposited by PVD: In2S3 containing Na compounds". In: *Thin Solid Films* 431 (2003), pp. 326–329.

[66]   ZA. Wang, JB. Chu, HB. Zhu, Z. Sun, YW. Chen, and SM. Huang. "Growth of ZnO: Al films by RF sputtering at room temperature for solar cell applications". In: *Solid-State Electronics* 53.11 (2009), pp. 1149–1153.

[67] A. Kylner. "The chemical bath deposited CdS/Cu(In,Ga)Se$_2$ interface as revealed by X-ray photoelectron spectroscopy". In: *Journal of the Electrochemical Society* 146.5 (1999), pp. 1816–1823.

[68] Y. Hashimoto, N. Kohara, T. Negami, N. Nishitani, and T. Wada. "Chemical bath deposition of Cds buffer layer for GIGS solar cells". In: *Solar Energy Materials and Solar Cells* 50.1-4 (1998), pp. 71–77.

[69] T. Nakada and A. Kunioka. "Direct evidence of Cd diffusion into Cu(In,Ga)Se$_2$ thin films during chemical-bath deposition process of CdS films". In: *Applied Physics Letters* 74.17 (1999), pp. 2444–2446.

[70] U. Rau and M. Schmidt. "Electronic properties of ZnO/CdS/Cu(In,Ga)Se$_2$ solar cell-saspects of heterojunction formation". In: *Thin Solid Films* 387.1-2 (2001), pp. 141–146.

[71] S Ishizuka, K Sakurai, A Yamada, K Matsubara, P Fons, K Iwata, S Nakamura, Y Kimura, T Baba, H Nakanishi, et al. "Fabrication of wide-gap Cu(In$_{1-x}$Ga$_x$)Se$_2$ thin film solar cells: a study on the correlation of cell performance with highly resistive i-ZnO layer thickness". In: *Solar energy materials and solar cells* 87.1-4 (2005), pp. 541–548.

[72] SS. Hegedus, D. Desai, and C. Thompson. "Voltage dependent photocurrent collection in CdTe/CdS solar cells". In: *Progress in Photovoltaics: Research and Applications* 15.7 (2007), pp. 587–602.

[73] SS. Hegedus. "Current–Voltage Analysis of a-Si and a-SiGe Solar Cells Including Voltage-dependent Photocurrent Collection". In: *Progress in Photovoltaics: Research and Applications* 5.3 (1997), pp. 151–168.

[74] F. Obereigner and R. Scheer. "Determining diode parameters of illuminated current density-voltage curves considering the voltage-dependent photo current density". In: *EPJ Photovoltaics* 5 (2014), p. 50101.

[75] T. Meyer, M. Schmidt, F. Engelhardt, J. Parisi, and U. Rau. "A model for the open circuit voltage relaxation in Cu(In,Ga)Se$_2$ heterojunction solar cells". In: *The European Physical Journal Applied Physics* 8.1 (1999), pp. 43–52.

[76] R. Scheer, L. Messmann-Vera, R. Klenk, and HW. Schock. "On the role of non-doped ZnO in CIGSe solar cells". In: *Progress in Photovoltaics: Research and Applications* 20.6 (2012), pp. 619–624.

[77] M. Maiberg. "Numerical and analytical study of time-resolved luminescence in thin-film semiconductors". PhD thesis. Martin-Luther-Universität Halle-Wittenberg, 2016.

[78] MA. Contreras, K. Ramanathan, J. AbuShama, F. Hasoon, DL. Young, B. Egaas, and R. Noufi. "ACCELERATED PUBLICATION: Diode characteristics in state-of-the-art ZnO/CdS/Cu(In$_{1-x}$,Ga$_x$)Se$_2$ solar cells". In: *Progress in Photovoltaics: Research and Applications* 13.3 (2005), pp. 209–216.

[79]   M. Eron and A. Rothwarf. "Effects of a voltage-dependent light-generated current on solar cell measurements: CuInSe$_2$/Cd(Zn)S". In: *Applied Physics Letters* 44.1 (1984), pp. 131–133.

[80]   T. Dullweber, O. Lundberg, J. Malmström, M. Bodegård, L. Stolt, U. Rau, HW. Schock, and JH. Werner. "Back surface band gap gradings in Cu(In,Ga)Se$_2$ solar cells". In: *Thin Solid Films* 387.1-2 (2001), pp. 11–13.

[81]   A. Chirilă, S. Buecheler, F. Pianezzi, P. Bloesch, C. Gretener, AR. Uhl, C. Fella, L. Kranz, J. Perrenoud, S. Seyrling, et al. "Highly efficient Cu(In,Ga)Se$_2$ solar cells grown on flexible polymer films". In: *Nature materials* 10.11 (2011), p. 857.

[82]   O. Lundberg, M. Edoff, and L. Stolt. "The effect of Ga-grading in CIGS thin film solar cells". In: *Thin Solid Films* 480 (2005), pp. 520–525.

[83]   SM. Schleussner, U. Zimmermann, T. Wätjen, K. Leifer, and M. Edoff. "Effect of gallium grading in Cu(In,Ga)Se$_2$ solar-cell absorbers produced by multi-stage coevaporation". In: *Solar Energy Materials and Solar Cells* 95.2 (2011), pp. 721–726.

[84]   M. Gloeckler and JR. Sites. "Band-gap grading in Cu(In,Ga)Se$_2$ solar cells". In: *Journal of Physics and Chemistry of Solids* 66.11 (2005), pp. 1891–1894.

[85]   D. Poplavskyy, J. Bailey, R. Farshchi, and D. Spaulding. "Impact of Ga/III Profile on Voltage-dependent Collection Losses in CIGS Solar Cells". In: *2017 IEEE 44th Photovoltaic Specialist Conference (PVSC)*. IEEE. 2017, pp. 1686–1690.

[86]   M. Gloeckler. "Device physics of Cu(In,Ga)Se$_2$ thin-film solar cells." PhD thesis. Colorado State University, 2004.

[87]   MA. Green. "Generalized relationship between dark carrier distribution and photocarrier collection in solar cells". In: *Journal of applied physics* 81.1 (1997), pp. 268–271.

[88]   K. Orgassa. *Coherent Optical Analysis of the ZnO/CdS/Cu(In,Ga)Se$_2$ Thin Film Solar Cell*. Shaker, 2004.

[89]   R. Klenk. "Characterisation and modelling of chalcopyrite solar cells". In: *Thin solid films* 387.1-2 (2001), pp. 135–140.

[90]   S. Zahedi-Azad, M. Maiberg, R. Clausing, and R. Scheer. "Influence of heavy alkali post deposition treatment on wide gap Cu(In,Ga)Se$_2$". In: *Thin Solid Films* 669 (2019), pp. 629–632.

[91]   T. Eisenbarth, T. Unold, R Caballero, CA. Kaufmann, D. Abou-Ras, and HW. Schock. "Origin of defects in CuIn$_{1-x}$Ga$_x$Se$_2$ solar cells with varied Ga content". In: *Thin Solid Films* 517.7 (2009), pp. 2244–2247.

[92]   G. Hanna, A. Jasenek, U. Rau, and HW. Schock. "Influence of the Ga-content on the bulk defect densities of Cu(In,Ga)Se$_2$". In: *Thin Solid Films* 387.1-2 (2001), pp. 71–73.

[93]   S. Zahedi-Azad and R. Scheer. "Quenching interface recombination in wide bandgap Cu(In,Ga)Se$_2$ by potassium treatment". In: *physica status solidi c* 14.6 (2017), p. 1600203.

[94] T. Lepetit, L. Harel S.and Arzel, G. Ouvrard, and N. Barreau. "KF post deposition treatment in co-evaporated Cu(In,Ga)Se$_2$ thin film solar cells: Beneficial or detrimental effect induced by the absorber characteristics". In: *Progress in Photovoltaics: Research and Applications* 25.12 (2017), pp. 1068–1076.

[95] E. Avancini, R. Carron, TP. Weiss, Ch. Andres, M. Burki, C. Schreiner, R. Figi, YE. Romanyuk, St. Buecheler, and AN. Tiwari. "Effects of rubidium fluoride and potassium fluoride postdeposition treatments on Cu(In,Ga)Se$_2$ thin films and solar cell performance". In: *Chemistry of Materials* 29.22 (2017), pp. 9695–9704.

[96] T. Kodalle, MD. Heinemann, D. Greiner, HA. Yetkin, M. Klupsch, C. Li, PA. van Aken, I. Lauermann, R. Schlatmann, and CA. Kaufmann. "Elucidating the mechanism of an RbF post deposition treatment in CIGS thin film solar cells". In: *Solar RRL* 2.9 (2018), p. 1800156.

[97] WK. Metzger, IL. Repins, M. Romero, P. Dippo, M. Contreras, R. Noufi, and D. Levi. "Recombination kinetics and stability in polycrystalline Cu(In,Ga)Se$_2$ solar cells". In: *Thin Solid Films* 517.7 (2009), pp. 2360–2364.

[98] R. Scheer, A. Pérez-Rodríguez, and WK. Metzger. "Advanced diagnostic and control methods of processes and layers in CIGS solar cells and modules". In: *Progress in Photovoltaics: Research and applications* 18.6 (2010), pp. 467–480.

[99] B. Ohnesorge, R. Weigand, G. Bacher, A. Forchel, W. Riedl, and FH. Karg. "Minority-carrier lifetime and efficiency of Cu(In,Ga) Se$_2$ solar cells". In: *Applied Physics Letters* 73.9 (1998), pp. 1224–1226.

[100] M. Maiberg, T. Hölscher, S. Zahedi-Azad, W. Fränzel, and R. Scheer. "Investigation of long lifetimes in Cu(In,Ga)Se$_2$ by time-resolved photoluminescence". In: *Applied Physics Letters* 107.12 (2015), p. 122104.

[101] F. Pianezzi, P. Reinhard, A. Chirilă, B. Bissig, S. Nishiwaki, S. Buecheler, and AN. Tiwari. "Unveiling the effects of post-deposition treatment with different alkaline elements on the electronic properties of CIGS thin film solar cells". In: *Physical Chemistry Chemical Physics* 16.19 (2014), pp. 8843–8851.

[102] S. Ishizuka, N. Taguchi, J. Nishinaga, Y. Kamikawa, S. Tanaka, and H. Shibata. "Group III elemental composition dependence of RbF postdeposition treatment effects on Cu(In,Ga)Se$_2$ thin films and solar cells". In: *The Journal of Physical Chemistry C* 122.7 (2018), pp. 3809–3817.

[103] C. Hsu, W. Ho, S. Wei, and C. Lai. "Over 14% efficiency of directly sputtered Cu (In,Ga) Se$_2$ absorbers without postselenization by post-treatment of alkali metals". In: *Advanced Energy Materials* 7.13 (2017), p. 1602571.

[104] A. Niemegeers, M. Burgelman, R. Herberholz, U. Rau, D. Hariskos, and HW. Schock. "Model for electronic transport in Cu(In,Ga)Se$_2$ solar cells". In: *Progress in Photovoltaics: Research and Applications* 6.6 (1998), pp. 407–421.

[105] M. Gloeckler, CR. Jenkins, and JR. Sites. "Explanation of light/dark superposition failure in CIGS solar cells". In: *MRS Online Proceedings Library Archive* 763 (2003).

[106] AO. Pudov, JR. Sites, MA. Contreras, T. Nakada, and HW. Schock. "CIGS J-V distortion in the absence of blue photons". In: *Thin Solid Films* 480 (2005), pp. 273–278.

[107] TP. Weiss, S. Nishiwaki, B. Bissig, R. Carron, E. Avancini, J. Löckinger, S. Buecheler, and AN. Tiwari. "Injection Current Barrier Formation for RbF Postdeposition-Treated Cu(In,Ga)Se$_2$-Based Solar Cells". In: *Advanced Materials Interfaces* 5.4 (2018), p. 1701007.

[108] T. Ott, T. Walter, and T. Unold. "Phototransistor effects in Cu(In,Ga)Se$_2$ solar cells". In: *Thin Solid Films* 535 (2013), pp. 275–278.

[109] A. Kylner. "Effect of impurities in the CdS buffer layer on the performance of the Cu(In,Ga)Se$_2$ thin film solar cell". In: *Journal of applied physics* 85.9 (1999), pp. 6858–6865.

[110] IL. Eisgruber, JE. Granata, JR. Sites, J. Hou, and J. Kessler. "Blue-photon modification of nonstandard diode barrier in CuInSe$_2$ solar cells". In: *Solar Energy Materials and Solar Cells* 53.3-4 (1998), pp. 367–377.

[111] M. Köntges, R. Reineke-Koch, P. Nollet, J. Beier, R. Schäffler, and J. Parisi. "Light induced changes in the electrical behavior of CdTe and Cu(In,Ga)Se$_2$ solar cells". In: *Thin Solid Films* 403 (2002), pp. 280–286.

[112] D. Schmid, M. Ruckh, and HW. Schock. "A comprehensive characterization of the interfaces in Mo/CIS/CdS/ZnO solar cell structures". In: *Solar Energy Materials and Solar Cells* 41 (1996), pp. 281–294.

[113] M. Topič, F. Smole, and J. Furlan. "Examination of blocking current-voltage behaviour through defect chalcopyrite layer in ZnO/CdS/Cu(In,Ga)Se$_2$/Mo solar cell". In: *Solar energy materials and solar cells* 49.1-4 (1997), pp. 311–317.

[114] TP. Weiss, S. Nishiwaki, B. Bissig, S. Buecheler, and AN. Tiwari. "Voltage dependent admittance spectroscopy for the detection of near interface defect states for thin film solar cells". In: *Physical Chemistry Chemical Physics* 19.45 (2017), pp. 30410–30417.

[115] F. Pianezzi, P. Reinhard, A. Chirilă, S. Nishiwaki, B. Bissig, S. Buecheler, and AN. Tiwari. "Defect formation in Cu(In,Ga)Se$_2$ thin films due to the presence of potassium during growth by low temperature co-evaporation process". In: *Journal of Applied Physics* 114.19 (2013), p. 194508.

[116] AO. Pudov, A. Kanevce, HA. Al-Thani, JR. Sites, and FS. Hasoon. "Secondary barriers in CdS–CuIn$_{1-x}$Ga$_x$Se$_2$ solar cells". In: *Journal of applied physics* 97.6 (2005), p. 064901.

[117] A. Kanevce, M. Gloeckler, AO. Pudov, and JR. Sites. "Conduction-band-offset rule governing JV distortion in CdS/CI(G)S solar cells". In: *MRS Online Proceedings Library Archive* 865 (2005).

[118]   A. Kanevce, K. Ramanathan, and M. Contreras. "Impact of buffer and absorber properties in the vicinity of the interface on wide-gap Cu(In,Ga)Se$_2$ solar cell performance". In: *2014 IEEE 40th Photovoltaic Specialist Conference (PVSC)*. IEEE. 2014, pp. 0382–0386.

[119]   T. Ott, F. Schönberger, T. Walter, D. Hariskos, O. Kiowski, O. Salomon, and R. Schäffler. "Verification of phototransistor model for Cu(In,Ga)Se$_2$ solar cells". In: *Thin Solid Films* 582 (2015), pp. 392–396.

[120]   R. Scheer. "DIODE CURRENTS IN THE LIM IT OF INTERFACE RECOM BINATION AND THEIR DIAGNOSIS". In: *23rd European Photovoltaic Solar Energy Conference, Valencia, Spain* (2008).

[121]   F. Engelhardt, M. Schmidt, T. Meyer, O. Seifert, J. Parisi, and U. Rau. "Metastable electrical transport in Cu(In,Ga)Se$_2$ thin films and ZnO/CdS/Cu(In,Ga)Se$_2$ heterostructures". In: *Physics Letters A* 245.5 (1998), pp. 489–493.

[122]   I. Repins, S. Glynn, TJ. Silverman, R. Garris, K. Bowers, B. Stevens, and L. Mansfield. "Large metastability in Cu(In,Ga)Se$_2$ devices: The importance of buffer properties". In: *Progress in Photovoltaics: Research and Applications* 27.9 (2019), pp. 749–759.

[123]   D. Rudmann, D. Brémaud, AF. Da Cunha, G. Bilger, A. Strohm, M. Kaelin, H Zogg, and AN. Tiwari. "Sodium incorporation strategies for CIGS growth at different temperatures". In: *Thin Solid Films* 480 (2005), pp. 55–60.

[124]   PMP. Salomé, A. Hultqvist, V. Fjällström, B. Vermang, M. Edoff, B. Aitken, K. Zhang, K. Fuller, and CK. Williams. "The effect of high growth temperature on Cu(In,Ga)Se$_2$ thin film solar cells". In: *Solar Energy Materials and Solar Cells* 123 (2014), pp. 166–170.

[125]   O. Lundberg, J. Lu, A. Rockett, M. Edoff, and L. Stolt. "Diffusion of indium and gallium in Cu (In,Ga)Se$_2$ thin film solar cells". In: *Journal of Physics and Chemistry of Solids* 64.9-10 (2003), pp. 1499–1504.

[126]   R. Caballero, CA. Kaufmann, V. Efimova, T. Rissom, V. Hoffmann, and HW. Schock. "Investigation of Cu(In,Ga)Se$_2$ thin-film formation during the multi-stage co-evaporation process". In: *Progress in Photovoltaics: Research and Applications* 21.1 (2013), pp. 30–46.

[127]   M. Nichterwitz. "Charge carrier transport in Cu (In, Ga) Se$_2$ thin-film solar-cells studied by electron beam induced current and temperature and illumination dependent current voltage analyses". PhD thesis. 2012.

[128]   P. Salomé, V. Fjällström, A. Hultqvist, and M. Edoff. "Na doping of CIGS solar cells using low sodium-doped Mo layer". In: *IEEE Journal of Photovoltaics* 3.1 (2012), pp. 509–513.

[129]   T. Bertram, J. Lauche, T. Kodalle, HA. Yetkin, MD. Heinemann, R. Schlatmann, and CA. Kaufmann. "RbF-PDT induced sodium displacement in Cu(In,Ga)Se$_2$ absorbers grown under high substrate temperatures". In: *2018 IEEE 7th World Conference on Photovoltaic Energy Conversion (WCPEC)(A Joint Conference of 45th IEEE PVSC, 28th PVSEC & 34th EU PVSEC)*. IEEE. 2018, pp. 0109–0113.

[130]   K. Granath, M. Bodegård, and L. Stolt. "The effect of NaF on Cu(In,Ga)Se$_2$ thin film solar cells". In: *Solar energy materials and solar cells* 60.3 (2000), pp. 279–293.

[131] GH. Bauer, R. Brüggemann, S. Tardon, S. Vignoli, and R. Kniese. "Quasi-Fermi level splitting and identification of recombination losses from room temperature luminescence in Cu(In$_{1-x}$Ga$_x$)Se$_2$ thin films versus optical band gap". In: *Thin Solid Films* 480 (2005), pp. 410–414.

[132] W. Witte, D. Hariskos, R. Kniese, and M. Powalla. "Short-circuit current improvement of CuGaSe$_2$ solar cells with a ZnS/(Zn,Mg)O buffer combination". In: *physica status solidi (RRL)–Rapid Research Letters* 2.2 (2008), pp. 80–82.

Acknowledgements

Selbstständigkeitserklärung

Hiermit versichere ich, dass ich die vorliegende Dissertation mit dem Titel:

"Characterization of Alkaline-doped wide band-gap chalcopyrite $Cu(In,Ga)Se_2$
thin films and solar cells"

selbstständig und nur unter Verwendung der angegebenen Quellen und Hilfsmittel angefertigt habe. Die aus fremden Quellen direkt oder indirekt übernommenen Stellen sind als solche kenntlich gemacht.

Die Arbeit wurde bisher in gleicher oder ähnlicher Form keiner anderen Prüfungsbehörde vorgelegt und auch nicht veröffentlicht.

Halle, den 07. Januar 2020

Publications

- **S. Zahedi-Azad**, M. Maiberg, R. Clausing, R. Scheer, Influence of heavy alkali post deposition treatment on wide gap Cu(In,Ga)Se$_2$, Thin Solid Films, 669 (2018) 629-632.

- **S. Zahedi-Azad**, R. Scheer, Quenching interface recombination in wide bandgap Cu(In,Ga)Se$_2$ by potassium treatment, Physica Status Solidi. C, Current Topics in Solid State Physics 14 (2017) 1600203.

- **S. Zahedi-Azad**, E. Jarzembowski, S. Hartnauer, L. Wägele, D. Greiner, R. Scheer, Monitoring the phase evolution of Cu(In,Ga)Se$_2$ by different Se flux via in-situ XRD, physica status solidi (a), 213 (2016) 2169-2175.

- P. Pistor, **S. Zahedi-Azad**, S. Hartnauer, L.A. Wägele, E. Jarzembowski, R. Scheer, Real time observation of phase formations by XRD during Ga-rich or In-rich Cu (In, Ga) Se$_2$ growth by co-evaporation, physica status solidi (a), 212 (2015) 1897-1904.

- M. Maiberg, T. Hölscher, **S. Zahedi-Azad**, W. Fränzel, R. Scheer, Investigation of long lifetimes in Cu (In, Ga) Se$_2$ by time-resolved photoluminescence, Applied Physics Letters, 107 (2015) 122104.

- M. Maiberg, T. Hölscher, **S. Zahedi-Azad**, W. Fränzel, R. Scheer, Investigation of long lifetimes in Cu (In,Ga)Se$_2$ by time-resolved photoluminescence, Applied Physics Letters, 107 (2015) 122104.

- M. Maiberg, T. Hölscher, **S. Zahedi-Azad**, R. Scheer, Theoretical study of time-resolved luminescence in semiconductors. III. Trap states in the band gap, Journal of Applied Physics, 118 (2015) 105701.

Curriculum Vitae

Personal Details

Name	**Setareh Zahedi-Azad**
Date of Birth	**18.06.1988**
Place of Birth	**Essen**
Nationallity	**Iran**
E-mail	**setareh.zahedi-azad@physik.uni-halle.de**

Education

2014–2020   **Doctoral Researcher**, *Department of Physics, Martin-Luther University*

Topic: Characterization of Alkaline-doped wide bandgap chalcopyrite $Cu(In,Ga)Se_2$ thin films and solar cells

2010–2013   **Master of Photonics**, *Institute of Plasma & Photonics, University of Shahid Beheshti, Teheran Iran*

Topic: Inactivation of Fungus by non-thermal Plasma,

2006–2010   **Bachelor of Physics**, *Department of Physics, K. N. Toosi University, Teheran, Iran*

Topic: Non-Destructive Testing by SQUIDS